

Concrete Bridge Deck Surface Characterization: Resolving Cracks Using Optical Sensors and  
Image Processing

---

A Thesis

Presented to  
the faculty of the School of Engineering and Applied Science  
University of Virginia

---

in partial fulfillment  
of the requirements for the degree

Master of Science

by

Lauren M Bolton

May

2015

APPROVAL SHEET

The thesis  
is submitted in partial fulfillment of the requirements  
for the degree of  
Master of Science

Lauren M. Bolton

---

AUTHOR

The thesis has been read and approved by the examining committee:

Dr. Devin Harris

---

Advisor

Dr. Thomas Baber

---

Dr. Steven Chase

---

---

---

---

Accepted for the School of Engineering and Applied Science:



Dean, School of Engineering and Applied Science

May  
2015

## TABLE OF CONTENTS

---

<b>LIST OF FIGURES</b> .....	iii
<b>LIST OF TABLES</b> .....	vi
<b>ACKNOWLEDGMENTS</b> .....	viii
<b>ABSTRACT</b> .....	ix
<b>1.0 INTRODUCTION</b> .....	1
<b>1.1 Background</b> .....	1
<b>1.2 Thesis Overview and Scope</b> .....	1
<b>1.3 Thesis Organization</b> .....	2
<b>2.0 LITERATURE REVIEW</b> .....	3
<b>2.1 Bridge Deck Deterioration Mechanisms</b> .....	3
<b>2.2 Bridge Deck Inspection Methods</b> .....	5
<b>2.2.1 Non-Destructive Evaluation Techniques</b> .....	7
<b>2.3 Feature Detection – Image Acquisition</b> .....	13
<b>2.3.1 Imaging Platforms</b> .....	13
<b>2.4 Feature Detection – Image Processing</b> .....	15
<b>2.4.1 State of Practice – Concrete Crack Detection</b> .....	22
<b>3.0 METHODOLOGY</b> .....	27
<b>3.1 Image Acquisition Equipment</b> .....	27
<b>3.2 Feature Detection – Crack Identification</b> .....	31
<b>3.2.1 Jahanshahi Adapted Method</b> .....	33
<b>3.2.2 Fujita Adapted Method</b> .....	35
<b>3.2.3 Lattanzi Adapted Method</b> .....	37
<b>3.2.4 Combined Algorithm</b> .....	39
<b>3.3 Feature Evaluation – Crack Measurement</b> .....	41
<b>3.4 Experimental Testing</b> .....	43
<b>3.4.1 Simulated Cracks</b> .....	44
<b>3.4.2 Idealized Laboratory Cracks</b> .....	46
<b>3.4.3 In-Service Cracks</b> .....	52
<b>3.5 Summary of Methodology</b> .....	54
<b>4.0 RESULTS</b> .....	55

<b>4.1 Simulated Crack Results</b> .....	55
<b>4.2 Ideal Laboratory Results</b> .....	59
<b>4.2.1 Definition of Error</b> .....	59
<b>4.2.2 Comparison of Image Processing Techniques</b> .....	60
<b>4.2.3 Comparison of Crack Geometry, Working Distances and Focal Lengths</b> ...	61
<b>4.2.4 Comparison of Image Acquisition Systems</b> .....	65
<b>4.2.5 Aperture Analysis</b> .....	68
<b>4.3 In-Service Crack Results</b> .....	69
<b>4.3.1 Crack Detection</b> .....	69
<b>4.3.2 Crack Geometry</b> .....	73
<b>5.0 CONCLUSIONS</b> .....	75
<b>6.0 FUTURE WORK</b> .....	78
<b>REFERENCES</b> .....	81
<b>APPENDIX A: EXPERIMENTAL SET-UP</b> .....	87
<b>APPENDIX B: SIMULATED CRACKS</b> .....	99
<b>APPENDIX C: IDEAL LABORATORY CRACK</b> .....	103
<b>APPENDIX D: IN-SERVICE CRACKS</b> .....	118
<b>APPENDIX E: MATLAB CODES</b> .....	124

## LIST OF FIGURES

---

Figure 1: Example of a Spall.....	4
Figure 2: Types of Cracks: a) Pattern Cracking; b) Linear Cracking .....	4
Figure 3: Example of Subsurface Defect Found by Using an Infrared Camera .....	9
Figure 4: Example GPR Data: a) No Rebar; b) Rebar .....	10
Figure 5: Example Impact Echo Inspection: a) Impact Echo Scanner; b) Thickness Scan .	11
Figure 6: The Electromagnetic Spectrum.....	14
Figure 7: Example of a Grayscale and Binary Image .....	16
Figure 8: Comparison of Global and Local Threshold Methods .....	17
Figure 9: Morphological Operations (Adapted from Acton, 2013) .....	19
Figure 10: Example of Edge Detection Methods.....	20
Figure 11: Example of the Active Contour Technique .....	21
Figure 12: Percolation Technique: a) Focal Pixel in the Background; b) Focal Pixel in the Crack .....	22
Figure 13: Crack Detection Algorithm by Fujita and Hamamoto (Adapted from Fujita & Hamamoto, 2011).....	25
Figure 14: Crack Detection Algorithm by Jahanshahi et al (Adapted from Jahanshahi et al., 2011).....	26
Figure 15: Comparison of Camera Sensor Sizes.....	29
Figure 16: Field of View Diagram .....	30
Figure 17: Comparison of Focal Lengths.....	31
Figure 18: Example of Open-Close Functions (Adapted from Acton, 2013). .....	34
Figure 19: Illustration of the Jahanshahi Adapted Method .....	35
Figure 20: Illustration of the Fujita Adapted Method .....	37
Figure 21: Illustration of the Lattanzi Adapted Method .....	39
Figure 22: Illustration of Combined Algorithm .....	41
Figure 23: Calculating Object Orientation (Adapted from MATLAB, 2013) .....	42
Figure 24: Example of Stair-Step Pixels .....	42
Figure 25: Euclidean Distance Transform .....	43
Figure 26: Simulated Crack.....	45
Figure 27: Experimental Set-Up for the Ideal Laboratory Crack Experiments .....	47
Figure 28: Sample Image of a) F-stop (f/8); b) F-stop (f/14).....	49
Figure 29: Sample Images of a) 17.9 Megapixels; b) 24.2 Megapixels.....	50
Figure 30: Sample Images of a) CCD Camera; b) DSLR Camera .....	51
Figure 31: Sample Images of a) Nikon D3200; b) Nikon D610 .....	52
Figure 32: Sample Sidewalk Crack Images: a) Optical Image; b) NIR Image .....	52
Figure 33: Example of Manually Segmented Image.....	53
Figure 34: Example of Subtracting Images.....	54
Figure 35: Example of Rotation Errors: a) 0.2 degrees; b) 1 degrees .....	56
Figure 36: Error Due to Orientation of a Crack: a) Up to 1 degrees; b) Up to 0.2 degrees .	57
Figure 37: Post Processed Laboratory Cracks: a) 0.125 in; b) 0.06 in; c) 0.02 in .....	63
Figure 38: Example Segmentation of In-Service Cracks Imaged with the Optical Camera	70

Figure 39: Example Segmentation of In-Service Cracks Imaged with the NIR Camera.....	71
Figure 40: Example of Residual Pixels .....	72
Figure 41: Example of Issues in Segmented Images: a) Noise; b) Non-continuous Pixels .	73
Figure 42: Ideal Laboratory Cracks .....	88
Figure 43: 4 in by 0.02 in Crack Imaged at 4 feet with a 60 mm and 85 mm Focal Length	89
Figure 44: 4 in by 0.02 in Crack Imaged with a 24 mm at 3 feet and 8 feet.....	90
Figure 45: 4 in by 0.06 in Crack Imaged at 4 feet with a 60 mm and 85 mm Focal Length	90
Figure 46: 4 in by 0.02 in Crack Imaged with a 24 mm at 3 feet and 8 feet.....	91
Figure 47: 4 in by 0.125 in Crack Imaged at 4 feet with a 60 mm and 85 mm Focal Length .....	91
Figure 48: 4 in by 0.125 in Crack Imaged with a 24 mm at 3 feet and 8 feet.....	92
Figure 49: 6 in with a Width of 0.125 in Imaged at 3 feet and 8 feet .....	92
Figure 50: 6 in with a Width of 0.06 in Imaged at 3 feet and 8 feet .....	93
Figure 51: 6 in with a Width of 0.02 in Imaged at 3 feet and 8 feet .....	93
Figure 52: Imaged with 24.3 Megapixels at 3 feet and 8 feet.....	94
Figure 53: Imaged with 18 Megapixels at 3 feet and 8 feet.....	94
Figure 54: DSLR Images at 1.5 feet and 8.5 feet.....	95
Figure 55: CCD Images at 1.5 feet and 8.5 feet.....	95
Figure 56: Optical Images at 3 feet and 8 feet .....	96
Figure 57: NIR Images at 3 feet and 8 feet .....	96
Figure 58: In-Service Cracks Optically Imaged.....	97
Figure 59: In-Service Cracks NIR Imaged.....	97
Figure 60: Image Processing Errors for a 0.25 in Crack Using a 24 mm Focal Length ....	103
Figure 61: Image Processing Errors for a 0.125 in Crack Using a 24 mm Focal Length ..	103
Figure 62: Image Processing Errors for a 0.125 in Crack Using a 60 mm Focal Length ..	103
Figure 63: Image Processing Errors for a 0.125 in Crack Using an 85 mm Focal Length	104
Figure 64: Image Processing Errors for a 0.06 in Crack Using a 24 mm Focal Length ....	104
Figure 65: Image Processing Errors for a 0.06 in Crack Using a 60 mm Focal Length ....	104
Figure 66: Image Processing Errors for a 0.06 in Crack Using an 85 mm Focal Length ..	105
Figure 67: Image Processing Errors for a 0.02 in Crack Using a 24 mm Focal Length ....	105
Figure 68: Image Processing Errors for a 0.02 in Crack Using a 60 mm Focal Length ....	105
Figure 69: Image Processing Errors for a 0.02 in Crack Using an 85 mm Focal Length ..	106
Figure 70: Image Processing Errors for a 6 in by 0.125 in Crack Using a 24 mm Focal Length.....	106
Figure 71: Image Processing Errors for a 6 in by 0.06 in Crack Using a 24 mm Focal Length.....	106
Figure 72: Image Processing Errors for a 6 in by 0.02 in Crack Using a 24 mm Focal Length.....	107
Figure 73: Image Processing Errors for a 4 in by 0.25 in Crack Using a 24 mm Focal Length and the Canon 7D.....	107
Figure 74: Image Processing Errors for a 4 in by 0.125 in Crack Using a 35 mm Focal Length and the CCD Camera .....	107

Figure 75: Image Processing Errors for a 4 in by 0.125 in Crack Using a 35 mm Focal Length and the DSLR Camera .....	108
Figure 76: Image Processing Errors for a 6 in by 0.125 in Crack Using a 24 mm Focal Length and the NIR Camera.....	108
Figure 77: Comparison of 24 mm Focal Length.....	108
Figure 78: Comparison of 60 mm Focal Length.....	109
Figure 79: Comparison of 85 mm Focal Length.....	109
Figure 80: Comparison of Focal Lengths.....	110
Figure 81: Comparison of Crack Thickness.....	110
Figure 82: Comparison of Crack Length.....	110
Figure 83: Comparison of Megapixels.....	111
Figure 84: Comparison of CCD vs DSLR .....	111
Figure 85: Comparison of NIR versus Optical.....	111
Figure 86: Interaction Plot for Width Errors (Minitab, 2007).....	117
Figure 87: Interaction Plot for Length Errors (Minitab, 2007) .....	117
Figure 88: Manually Segmented Optical Images.....	118
Figure 89: Optical Images Segmented by Jahanshahi Adapted Method.....	118
Figure 90: Optical Images Segmented by Fujita Adapted Method.....	119
Figure 91: Optical Images Segmented by Lattanzi Adapted Method .....	119
Figure 92: Optical Images Segmented by Combined Method .....	120
Figure 93: Manually Segmented NIR Images.....	121
Figure 94: NIR Images Segmented by Jahanshahi Adapted Method .....	121
Figure 95: NIR Images Segmented by Fujita Adapted Method.....	122
Figure 96: NIR Images Segmented by Lattanzi Adapted Method.....	122
Figure 97: NIR Images Segmented by Combined Method .....	123

## LIST OF TABLES

---

Table 1: PONTIS Rating for Concrete Bridge Decks .....	7
Table 2: Common Nondestructive Evaluation Methods for Evaluating Concrete Bridge Decks .....	8
Table 3: Image Acquisition Systems and Their Properties .....	28
Table 4: Previous Crack Detection Methods.....	32
Table 5: Pixel Requirements for the Nikon D610 with a 24mm Focal Length .....	45
Table 6: Geometric Properties of Ideal Laboratory Crack Specimens.....	46
Table 7: Experiments Conducted for the Idealized Laboratory Cracks .....	47
Table 8: Orientation of Specimens for Experiment 1 .....	48
Table 9: Example of Calculated Pixel Errors .....	58
Table 10: Mean Processing Errors for Calculating Width .....	61
Table 11: Factorial Design Analysis Results .....	62
Table 12: Factorial Design Results Regarding Width for Different Image Acquisition Systems.....	66
Table 13: Factorial Design Results Relating To Aperture .....	68
Table 14: Average Residual Pixels from the In-Service Cracks .....	73
Table 15: Average Optical Measurement Errors for In-Service Cracks .....	74
Table 16: Pixel Requirements for Nikon D610 with 60 mm Focal Length .....	87
Table 17: Pixel Requirements for Nikon D610 with 85 mm Focal Length .....	87
Table 18: Pixel Requirements for Canon 7D with 24 mm Focal Length.....	87
Table 19: Pixel Requirements for CCD and DSLR with 35 mm Focal Length.....	88
Table 20: Pixel Requirements for NIR Camera with 24 mm Focal Length.....	88
Table 21: Light Intensity Values .....	89
Table 22: In-Service Field Measurements .....	98
Table 23: Rotation Errors for 28 by 448 Pixel Crack .....	99
Table 24: Rotation Errors for a 11 by 169 Pixel Crack.....	99
Table 25: Rotation Errors for a 5 by 169 Pixel Crack.....	100
Table 26: Pixel Width Errors for the Nikon D610 and a 60 mm Focal Length.....	100
Table 27: Pixel Width Errors for the Nikon D610 and an 85 mm. Focal Length .....	101
Table 28: Pixel Width Errors for the Canon 7D and a 24 mm. Focal Length.....	101
Table 29: Pixel Width Errors for the CCD and DSLR camera with a 35 mm. Focal Length .....	101
Table 30: Pixel Width Errors for the Nikon D3200 and a 24 mm. Focal Length .....	102
Table 31: P-Values for Normality - Nikon D610 Imaging .....	112
Table 32: P-values for Normality - Acquisition Systems .....	112
Table 33: P-values for T-test - Length Comparison.....	113
Table 34: P-values for T-test - Acquisition Systems.....	113
Table 35: Average Aperture Errors for a 0.02 in. Crack.....	114
Table 36: Average Aperture Errors for a 0.06 in. Crack.....	115
Table 37: Average Aperture Errors for a 0.125 in. Crack .....	116
Table 38: Width Errors for In-Service Optical Images .....	120

Table 39: Length Errors for In-Service Optical Images..... 120

## ACKNOWLEDGMENTS

---

The author would like to thank the following for their support and contributions to this work;

- **Dr. Devin Harris**, for being my advisor and guiding me through my graduate research.
- **Dr. Steven Chase**, for serving on my committee and lending your expertise to assist me in learning various nondestructive inspection methods.
- **Dr. Thomas Baber**, for serving on my committee, and for guiding me throughout my academic career at the University.
- **Dr. Scott Acton** and his students **Suvadip Mukherjee** and **Rituparna Sarkar** for lending their expertise to assist me in evaluating digital image processing techniques, and for their never ending patience when teaching me how to use MATLAB.
- **Mid-Atlantic University Transportation Center (MAUTC)** for providing financial support.
- **Rachel Ford-Fink** and **Adam Maguire** for all of your help in capturing in-service crack images.
- **Muhammed Sherif**, for all of your help with, well, everything.

## **ABSTRACT**

---

Concrete bridge decks are a critical structural component in most bridges and the characterization of their deteriorating condition remains as an ongoing challenge for the Department of Transportation. These challenges include lane closures, inspector safety, and subjective results. Visual inspection remains as the primary and most common nondestructive evaluation technique for bridge decks, but recently there has been an increased interest in enhancing or even replacing this method with digital image processing techniques. An automated system would not only increase inspector safety but also produce reliable and repeatable results.

This thesis presents findings pertaining to the evaluation of non-contact measurement techniques in their use in quantifying cracks. In particular, the research compares promising image acquisition systems and analysis techniques. Images from both a controlled laboratory and outdoor environment were used to test the image acquisition systems and image processing methodologies, and establish a measure of both accuracy and efficiency. The outcome of the investigation provides confidence to the feasibility of the automated image processing approach, but also creates a foundation for the application to more complex environments.

## **1.0 INTRODUCTION**

---

### **1.1 Background**

As of 2013, the United States public road network consisted of 604,493 bridges (U.S. Department of Transportation 2013). The American Society of Civil Engineers (ASCE) states that “more than thirty percent of these bridges have exceeded their 50-year design life, meaning that maintenance, repair, and rehabilitation programs will still require significant investment in the upcoming years” (2013). These bridges must be inspected for degradation and repaired before they pose a threat to the commuting public.

A major component of a bridge is the bridge deck, and the degradation of the bridge deck will contribute greatly to the degradation of the entire bridge. The forms of surface degradation in concrete bridge decks include spalling and cracking, while subsurface degradation includes delamination (Federal Highway Administration 2012). Bridge inspectors currently rely on a visual analysis to evaluate a bridge deck for surface degradation. This type of evaluation method is costly, timely, and highly subjective. With the large amount of bridges that need to be inspected yearly, there is an increased need for a completely automated visual inspection system that can easily be used in the field to accurately monitor bridge deck conditions. In recent years, both image acquisition systems and image processing methods have improved greatly, thus potentially offering a means to develop a fully automated bridge inspection system.

### **1.2 Thesis Overview and Scope**

This study was conducted as a means of evaluating potential image acquisition systems and image processing methods that can be used in an automated system. The research was conducted in two

phases. The first phase focused on evaluating the errors associated with the set-up and the amount of error within feature detection methods. The goal of the first phase was to gain an understanding of how to select proper camera parameters in order to accurately analyze surface defects. The second phase of the research focused on evaluating and comparing various image processing algorithms that could be used to identify and quantify deterioration features.

### **1.3 Thesis Organization**

The following chapter, Chapter 2, presents a summary and review of the literature relevant to this research. The chapter includes background information on current bridge inspection methods and various image acquisition systems. The section also details past research on crack detection algorithms. Chapter 3 describes the experimental methodology, and the results are discussed in Chapter 4. Chapter 5 provides a summary of the research conducted and an overarching conclusion. Finally, Chapter 6 will describe possible future research in continuing to develop a fully automated bridge deck inspection system.

## **2.0 LITERATURE REVIEW**

---

There are many different materials used in bridge decks, such as timber, steel, and concrete and the evaluation of these decks are vital in ensuring the overall structural stability of a bridge. The following chapter details current bridge inspection methods used for concrete bridge decks within the United States. It also explains different technologies that can aid in the creation of a fully automatic inspection system. Finally, it details various algorithms that have been created to detect and analyze the geometric attributes of cracks in concrete specimens.

### **2.1 Bridge Deck Deterioration Mechanisms**

According to the Bridge Inspector's Reference Manual, the function of a concrete bridge deck is to provide a smooth riding surface and transfer both dead and live loads to the superstructure, thus making it a critical component to the structural integrity of the bridge (Federal Highway Administration 2012). Common deficiencies in bridge decks include but are not limited to, cracking, delamination, and spalling. Delamination is the surface separation of concrete into layers near the level of the reinforcing steel (Federal Highway Administration 2012). Delamination can be caused by the expansion of corroding steel or severe overstress of the deck (Federal Highway Administration 2012). Spalling occurs when a portion of the concrete completely separates from the surface concrete, as shown in Figure 1 (Federal Highway Administration 2012). Spalls can be caused by overstress, corroded reinforcement, or overfinishing (U.S. Department of Transportation et al. 2013).



Figure 1: Example of a Spall

Another deterioration mechanism is cracking. Cracks can occur on concrete bridge decks in even the highest quality of concrete. They are caused by either stress due to applied loads or stress due to volume changes (Kosmatka and Wilson 2011). The cracks that form can be described as either pattern cracks, shown in Figure 2a, or linear cracks, shown in Figure 2b (Virginia Department of Transportation 2009). Both types of cracks can pose problems to bridges and need to be accurately evaluated. The larger cracks can allow access for water and other corrosive materials to reach the reinforcing steel thus leading to the steel's deterioration (Ganapuram et al. 2012).



Figure 2: Types of Cracks: a) Pattern Cracking; b) Linear Cracking

## **2.2 Bridge Deck Inspection Methods**

According to the Federal Highway Administration (FHWA), bridges are typically inspected every 24 months, but bridges that show advanced deterioration are inspected more frequently (2012).

Bridge inspectors are required to examine all components of the 604,485 bridges across the nation based on a criteria outlined in the National Bridge Inspection Standards (NBIS) (U.S. Department of Transportation et al. 2013).

A condition rating system is used to measure the bridge's components over time. The rating categories vary from zero to nine, where nine rates the condition as excellent and zero rates the condition as failed (U.S. Department of Transportation et al. 2013). Using this data bridges can be classified, for example, as structurally deficient or functionally obsolete. According to the *2013 Status of the Nation's Highways, Bridges, and Transit* report (2013) bridges will be labeled as structurally deficient if a main component has a rating of four or lower, thus indicating that the bridge is in poor condition due to deterioration. The bridge could also be labeled as functionally obsolete if the bridge's geometry and design-load carrying capacity does not meet the standards required to carry the current amount of traffic. In 2010, 11.7 percent of bridges were considered structurally deficient and 14.2 percent were functionally obsolete (U.S. Department of Transportation et al. 2013).

As of July 2013, the Virginia Department of Transportation (VDOT) is responsible for the maintenance and inspection of 20,997 structures identified as bridges or culverts (Virginia Department of Transportation 2013). VDOT personnel typically inspect these bridges every two year. The data collected from the inspection are used to deem if the structures require repair,

maintenance, or replacement. In 2013, VDOT inspected around 10,700 bridges and culverts at a cost of about 26.1 million dollars (Virginia Department of Transportation 2013).

In addition to gathering data required by the NBIS, VDOT collected data of bridge's structural elements (Virginia Department of Transportation 2013). An element is defined as a component of a bridge, such as an abutment, pile, or girder. The elements are then subdivided into material type, such as timber or concrete (Virginia Department of Transportation 2007). Inspectors will inspect the elements and VDOT will incorporate this data into a database called Pontis (Virginia Department of Transportation 2007). Unlike the NBI inspection program, which has inspectors give an average rating to indicate the overall condition of the component, Pontis rates bridge elements in "quantitative units so that an inspector rates the entire element for the NBIS and then subdivides it into various condition states for Pontis" (Virginia Department of Transportation 2007). The condition states, using Pontis, for concrete bridge decks can be seen in Table 1.

Table 1: PONTIS Rating for Concrete Bridge Decks  
(Virginia Department of Transportation 2007).

<b>Element Rating</b>	<b>Condition State Description for Concrete Deck and Slabs</b>	<b>Condition State Description for Deck Cracking</b>
1	This element exhibits no patched areas and/or deficiencies such as spalling, delamination, etc.	The surface of the deck is cracked, but the cracks are either filled/sealed or insignificant in size and density (cracks less than 1/16 inch in width and spaced greater than 10 feet apart)
2	Patched areas, spalling/delamination and/or potholes exist. Their combined area is 10% or less of the total deck area	Unsealed crack exist which are of moderate size or density (cracks greater than or equal to 1/16 inch and less than 3/16 inch in width or where cracks are spaced 5 feet to 10 feet apart).
3	Patched areas, spalling/delamination and/or potholes exist. Their combined area is more than 10% but 25% or less of the total deck area	Unsealed cracks exist in the deck that are of moderate size and density (cracks greater than or equal to 1/16 inch and less than 3/16 inch in width and where cracks are spaced 5 feet to 10 feet apart).
4	Patched areas, spalling/delamination and/or potholes exist. Their combined area is 25% but less than 50% of the total deck area	Unsealed cracks exist in the deck that are of severe size and/or density (cracks greater than 3/16 inch in width and/or are spaced less than 5 feet apart).
5	Patched areas, spalling/delamination and/or potholes exist. Their combined area is 50% or more of the total deck area	

### 2.2.1 Non-Destructive Evaluation Techniques

Inspectors will employ a variety of non-destructive evaluation techniques, shown in Table 2, when inspecting a concrete bridge deck.

Table 2: Common Nondestructive Evaluation Methods for Evaluating Concrete Bridge Decks

<b>Inspection Method</b>	<b>Purpose</b>	<b>Example Defects</b>
<b>Visual Inspection</b>	Detection of Surface Defects	Cracks, Spalling, Rebar Rust Staining
<b>Infrared Thermography</b>	Detection of Near-Surface Defects	Delamination, Honeycombing
<b>Ground Penetrating Radar</b>	Detection of Near-Surface Features	Delamination, Air Voids, Location of Rebar
<b>Impact Echo</b>	Detection of Near-Surface Features	Delamination, Air Voids, Thickness of Concrete

### 2.2.1.1 Infrared Thermography

Infrared thermography, outlined in ASTM D4788-03, can be used to detect subsurface defects in concrete bridge decks, such as delamination, honeycombing, and voided tendon ducts (Clark et al. 2003). Two types of thermal inspection techniques are used in civil engineering. The first is passive thermography, which only observes the surface temperatures of objects by using an infrared detector. The second is active thermography, which supplies heat to an object and then observes the surface temperatures by using an infrared detector. For concrete bridges, delamination will modify the heat transfer properties of concrete and thus the image will be able to detect the location of the delamination (Vaghefi et al. 2013). If the delamination or voids are deep within the concrete, they will take longer to appear and have less contrast than if they were located at a shallower position (Washer et al. 2013). Figure 3 shows an example of a subsurface defect in a concrete bridge that was found using an infrared camera.

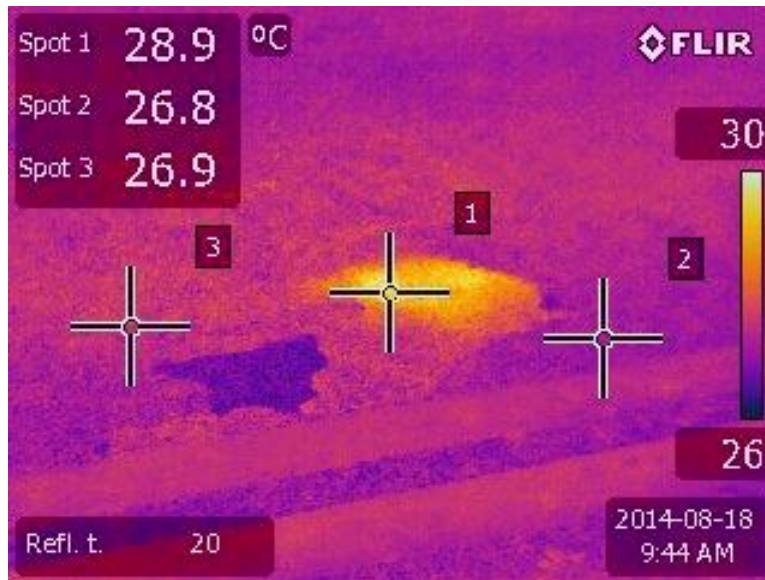


Figure 3: Example of Subsurface Defect Found by Using an Infrared Camera

The data acquired from the imaging equipment provides an instant image of the specimen for inspectors to analyze, and can visually show the locations of near surface defects. Some problems with infrared thermography include the subjectivity of its results. If the emissivity is different for each material, the objects will show different brightness, which does not necessarily mean they have different temperatures (Clark et al. 2003). Infrared thermography also cannot be accurately used if the weather conditions are not favorable or if voids are filled with water (Washer et al. 2013).

### 2.2.1.2 Ground Penetrating Radar

Another non-destructive evaluation technique for concrete bridge decks is ground penetrating radar (GPR). ASTM D6432-11 describes the equipment and the test method for conducting subsurface investigation using GPR (ASTM 2011). GPR uses an electromagnetic energy signal that penetrates through a surface (Daniels 2004). The waves interact throughout the specimen and are reflected back to the surface and recorded. These waves can be analyzed to assess the rebar,

rebar cover depth, and voids (Alani 2013). GPR is more sensitive to detecting metallic components that are perpendicular to the polarization (Geophysical Survey Systems, Inc. 2006). If steel is present in the concrete, the entire electromagnetic wave is reflected from the steel. Therefore, data that might lie beneath the steel, such as possible voids, cannot be gathered (Geophysical Survey Systems, Inc. 2006). To avoid this issue and allow the machine the ability to detect voids, it is recommended that the GPR system is oriented parallel to metallic components (Geophysical Survey Systems, Inc. 2006). Figure 4 shows an example of GPR data gathered when inspecting a concrete slab.

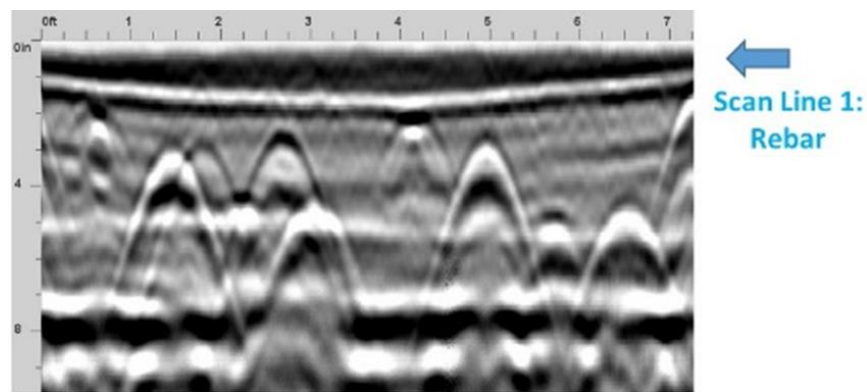


Figure 4: Example GPR Data

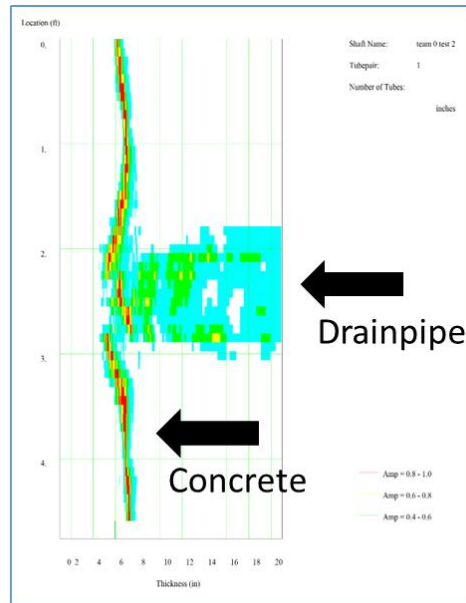
The advantages of GPR testing include its ability to detect defects such as voids, delamination, and metallic objects. It can also provide quantitative data; however, the interaction between the electromagnetic waves and the materials can be difficult to interpret. Therefore, extensive training is required in order to interpret this data accurately.

### 2.2.1.3 Impact Echo

Impact echo inspection is described in ASTM C1383-04 (ASTM 2010) and provides another means of inspecting concrete decks. The theory behind impact echo testing is stress waves are propagated into a concrete deck's surface through a mechanical impact (Carino 2001). The wave interacts with boundaries and interfaces causing low frequency waves to be reflected back to the surface and recorded (Sansalone 1997). The waves can then be used to evaluate the concrete deck to determine the thickness of the concrete and the location of voids or delamination (Sansalone 1997). The impact echo system can detect defects includes the defect's orientation and depth, and is affected by the contact time of the impact during the test (Carino 2001). Figure 5 shows an example an impact echo scanner and a thickness plot recorded during an impact echo inspection of a drainpipe underneath a concrete surface.



a)



b)

Figure 5: Example Impact Echo Inspection: a) Impact Echo Scanner; b) Thickness Scan

The advantages of impact echo testing include its ability to provide quantitative data, such as the depth to the defect and thickness of the concrete. However, impact echo systems are expensive, they can only perform local inspection, and inspectors must receive extensive training to accurately interpret the data.

#### **2.2.1.4 Visual Inspection**

The most common method is visual inspection, which is only effective in detecting surface defects. For bridge decks, surface defects include spalling, cracking, and rebar rust staining. For cracking, the inspector should note the orientation, width, and length of the crack (Atomic and Agency 2002). In August 2014, two VDOT inspectors were shadowed as they conducted a visual inspection of multiple bridge decks in the Charlottesville area. On the concrete bridge decks, the inspectors used visual inspection to look for cracks, spallings, and areas of possible delamination. They would use extended rulers to measure lengths of cracks and areas of spalling.

Although this method is efficient and low cost compared to other methods, there can be discrepancies in the identification and quantification of the condition state of the bridge. Factors influencing the accuracy of inspection include object characteristics, light, environmental factors, and human psychological factors (Hellier, 2013). Over the years, visual aids have been developed to help inspectors when they are on a job site. Such aids include flashlights, measuring devices, and cameras (Chase, 2013). However, even with these aids, the contrast between the defect and the surface, along with the lighting conditions still determine how easily a defect can be detected. The analysis of the surface defects found during visual inspection can also be subjective, causing discrepancies in the condition assessment of the bridge deck (Hellier, 2013).

## **2.3 Feature Detection – Image Acquisition**

An automated system would help eliminate some of the logistical and accuracy challenges involved in the traditional visual-based bridge deck inspection process. If designed properly, this system could provide reliable results and involve minimal disruption in motorist activities on the bridge. To maintain compatibility with current practices, an optical characterization method would be appropriate; however, current optical characterization techniques have major limitations in accuracy for both detection and quantification of cracks. The capturing and analysis of cracks within the concrete are difficult due to blemishes, voids, debris, shading, and the geometric features of the crack (Higgins and Turan 2013). Researchers have attempted to overcome these challenges through both digital image processing techniques and by using various camera technology to image the concrete. The focus in this investigation is on visual methods.

### **2.3.1 Imaging Platforms**

The most common image acquisition systems used are optical cameras. These cameras use only the visible light range, which has a wavelength between 400nm and 700nm, shown in Figure 6 (Ishikawa et al. 2014). To analyze a specimen, the optical cameras can either take a single photograph or take a series of photographs over a given period of time, which is called multitemporal images (Chen et al. 2006). There are generally two categories of techniques used for gathering the photographs. The first is aerial photography where images are taken from an aircraft (Jiang et al. 2008). Small-format aerial photography was used in 2011 to detect large cracks and joint openings on bridge decks from a height of 1,000ft (Chen et al. 2011). The other category is terrestrial, where images are taken near or on the surface (Jiang et al. 2008). These images are typically taken with either a Charged Couple Device (CCD) camera or a Digital Single-Lens

Reflex (DSLR) camera. There have also been instances of use with video microscopes, such as in 2002 when a video microscope was used to analyze defects in concrete slabs and beams (De Schutter 2002).

Another type of image acquisition system is the near infrared (NIR) camera. The NIR camera uses wavelengths just beyond the visible spectrum, usually between 800nm and 2,500nm (Hedrick et al. 2007). A comparison between the wavelengths for the visible and NIR spectrum can be seen below in Figure 6.

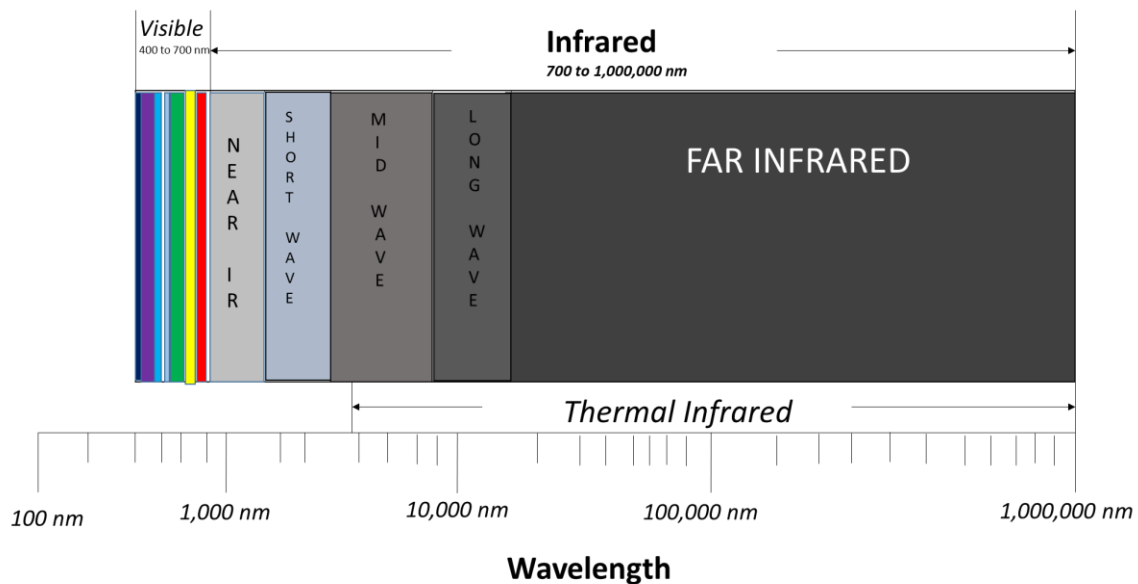


Figure 6: The Electromagnetic Spectrum

Most applications of NIR camera technology have been restricted to chemical, agriculture, polymers, and medical sciences (Siesler, Ozaki, Kawata, & Heise, 2002). However, there has been an increased interest in using NIR camera technology for analyzing materials used in infrastructures, such as wood, mortar, and concrete. In 2007, NIR sensors were used to measure

the longitudinal stiffness and longitudinal tensile strength of treated wood by obtaining the near infrared reflectance spectra along the radial-longitudinal face of the specimen (Hedrick et al. 2007). In 2015, NIR cameras were used to classify recycled aggregate, thus allowing aggregate that contained gypsum, autoclaved aerated concrete, or organic particles to be removed (Vegas et al. 2015).

Research has also been conducted using multi-spectral analysis. Multi-spectral analysis combines the blue, green, and red bands from the visible spectrum with the near-infrared band. Multi-spectral analysis was used to semi automatically detect materials within a masonry wall in Valencia, Spain (Lerma 2005). The materials it was able to identify included wood, glass, rock, and various mortars used in the pilaster and the face (Lerma 2005). Multi-spectral analysis has also been used to identify damage on concrete surfaces. In 2013, multi-spectral analysis was used to assess damage on roofs in Coimbra, Portugal (Valença et al., 2013). In particular, the experiments analyzed and measured areas that contained biological colonization, moisture, cracks, and repaired materials (Valença et al. 2013). The work done by both Valença et al (2013) and Lerma (2005) showed that combining the visible spectrum with the near-infrared spectrum can be used to better assess multiple materials in a structure.

#### **2.4 Feature Detection – Image Processing**

After gathering the images, researchers will use various digital image processing techniques to identify the location of cracks and their geometrical features. Many algorithms developed combine both basic and more advanced digital image processing tools. Some researchers process the images captured by using the RGB spectrum or the HSV color space. The HSV color space concentrates

on the variations of the hue, saturation, and intensity values of an image (Sural and Pramanik 2002). However, the majority of images are processed using grayscale. Grayscale converts the RGB values in an image to shades of gray, typically images are 8 bits and therefore have 256 gray levels (Bovik 2009). Grayscale serves as an advantage because it can simplify an image and allows for faster processing when converting to a binary image (Acton, 2013). Figure 7 shows an example of an image that has been converted to both a grayscale image and a binary image.



Figure 7: Example of a Grayscale and Binary Image

A binary image is an image that has converted the grayscale values into logical values, either a 1 or a 0 (Bovik 2009). Such processing allows an individual to see the absence and presence of certain properties. In order to convert a grayscale image to a binary image, the image must undergo thresholding. The quality of an image depends heavily on the thresholding process (Acton, 2013). The goal of thresholding is to separate the objects from the background and can be achieved through global thresholding or local thresholding (Bovik 2009). Figure 8 shows the methodology and an example of the two threshold methods.

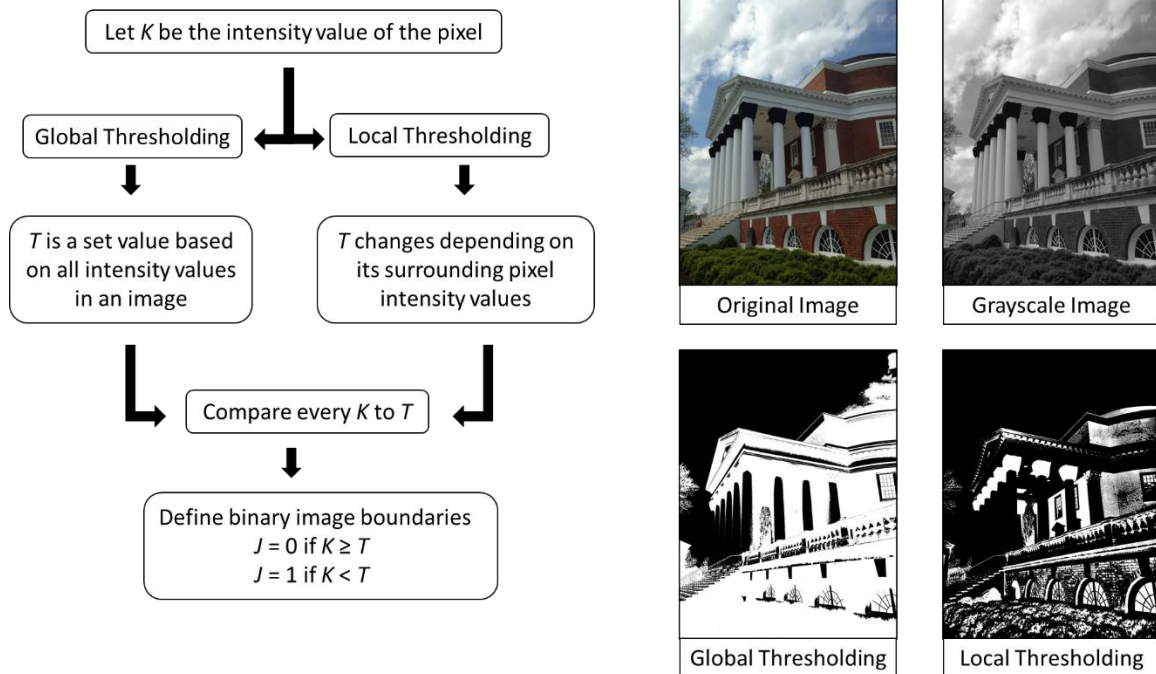


Figure 8: Comparison of Global and Local Threshold Methods

The example image displays the University of Virginia’s Rotunda. The global threshold method takes into account all of the intensity values in the image, while the local threshold method segments parts of an image based on the surrounding pixels’ intensities. Using the global threshold method, the Rotunda and the bushes are selected as the objects and segmented. However, with the local threshold method, the details of the Rotunda and bushes are locally segmented from the background. The outlines of the individual bricks can be seen in the local thresholding image, while in the global thresholding image the sky in the upper right corner is mistaken as part of the Rotunda. Global threshold methods are not as computationally expensive as local threshold methods, but local threshold methods excel when there are variations of lighting within an image (Bradley and Roth 2007).

One of the digital image processing methods used to identify the shape of a crack is morphological filtering. These are used to filter objects within an image. They can expand, shrink, smooth, or eliminate features within the image (Bovik 2009). Common morphological filters include:

- Dilation, which will remove holes that are very small and will remove gaps that are very narrow.
- Erosion, which will remove objects that are very small and will remove peninsulas that are very narrow.
- Median filter, which does not change the size of objects of background (Bovik 2009). The median filter will remove small object and small holes.
- Open function, which is erosion followed by dilation and will remove small objects but not holes. Similar to the median function, it does not affect the object's size (Bovik 2009).
- Close function, which is dilation followed by erosion and will remove small holes but not objects. Like the median filter, it does not affect the object's size (Bovik 2009).

An illustration of example outcomes for the various functions can be found in Figure 9 (Acton 2013).

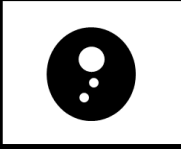
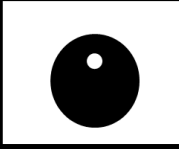
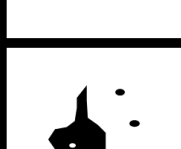
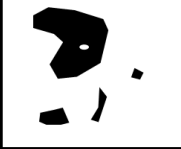
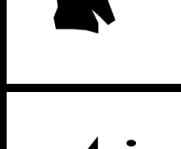
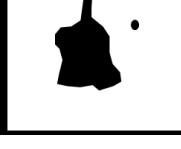
Method	Original Image	Processed Image	Method	Original Image	Processed Image
Dilation			Median		
				Open	
Erosion			Close		
					

Figure 9: Morphological Operations (Adapted from Acton 2013)

These morphological operations are implemented within a predefined geometric rule, called a window or a structuring element. The structuring element will have a predefined shape and size in which pixel data will be collected and modified (Bovik 2009). Common window shapes include a line, a square, or a cross (Acton, 2013). The size and shape of the window will have a great effect on the results of the morphological operation.

Another tool used in image processing is edge detections. Edges are defined as either points along which there is an abrupt change in orientation and surface features, or points which separate different materials (Bovik 2009). Two common edge detection methods include the Sobel edge detector and the Canny edge detector. The Sobel edge detector is a gradient edge detector that is simple and quick, but does not do well with noisy images (Acton, 2013). It detects the locations

that exhibit the greatest rate of change in image intensity and uses two convolution edge templates,  $\Delta_x$  and  $\Delta_y$  shown below, to help reduce noise (Bovik 2009).

$$\Delta_x = \begin{bmatrix} -1 & 0 & 1 \\ -2 & 0 & 2 \\ -1 & 0 & 1 \end{bmatrix} \quad \Delta_y = \begin{bmatrix} -1 & -2 & -1 \\ 0 & 0 & 0 \\ 1 & 2 & 1 \end{bmatrix} \quad \text{Equation 2.1}$$

The Canny edge detector is also a gradient detector, but it incorporates features of a Laplacian detector (Bovik 2009). This edge detector finds the edges based on the local maxima of the image gradient, which is calculated using the derivative of the Gaussian filter (Canny 1986). A comparison of the Sobel edge detection and the Canny edge detection can be seen in Figure 10. Comparatively, the Canny edge detector performs better than the Sobel edge detector because the Canny edge detector employs a blurring technique that helps eliminate the noises that the Sobel edge detector mistakes for edges (Abdel-qader et al. 2003). In Figure 10, the Canny edge detector distinguishes the shading in the image, unlike the Sobel edge detector.

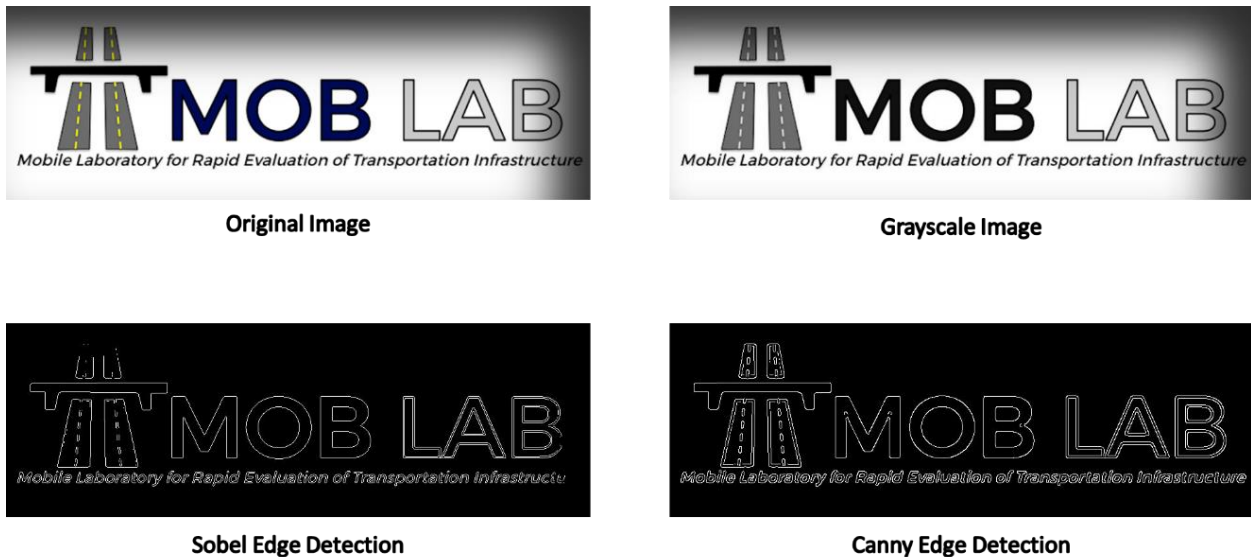


Figure 10: Example of Edge Detection Methods

A more advanced image processing method is called the active contour model, or snake (Tang et al. 2006). Snakes “deform on the image domain and capture a desired feature by minimizing an energy functional subject to certain constraints” (Li and Acton 2007). The snake model is influenced by image forces that push the snake onto features such as edges, and an external constraint force that puts the snake near the local minimum (Kass et al. 1987). The result is a curved object that converges on the closed boundary of the intended object (Chen and Hutchinson 2010). Figure 11 shows an example of this image processing technique.

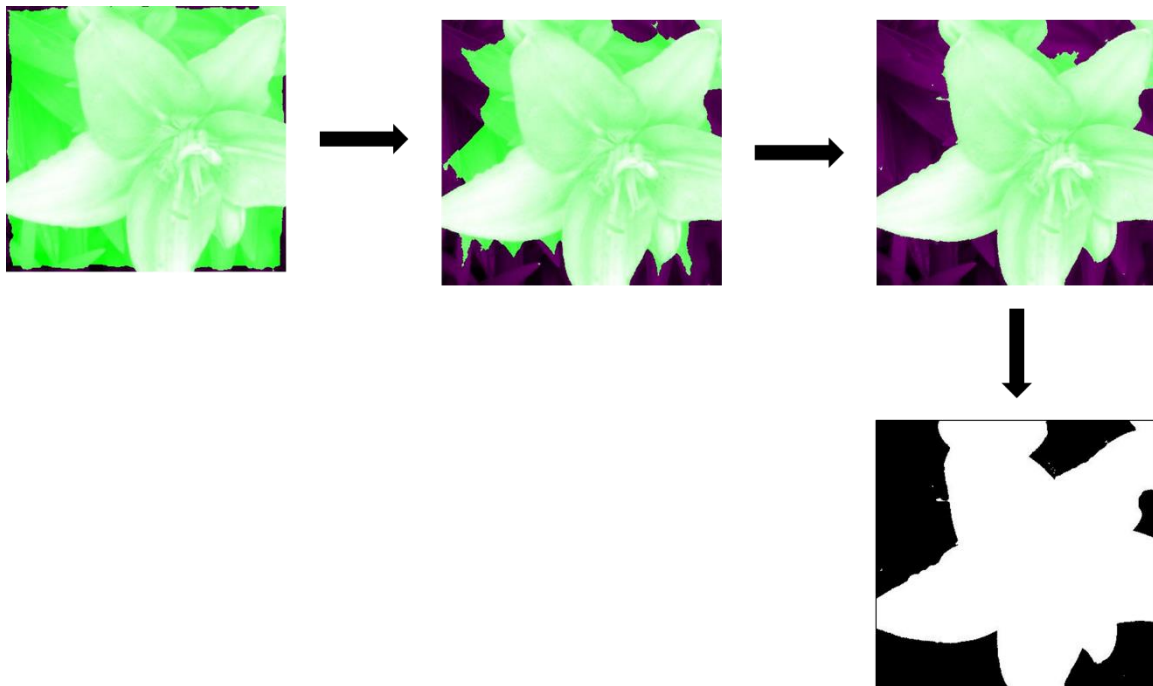


Figure 11: Example of the Active Contour Technique

Another advanced model is the percolation model, which is based on the principles of liquid permeation. To begin the process, a focal pixel is chosen, if that pixel is part of the crack, the region will grow linearly; however, if the focal pixel is not part of the crack, the region will grow

in all directions (Yamaguchi and Hashimoto 2009b). To determine if the focal pixel is part of a crack, the circularity, or roundness of a feature, is calculated using the following equation:

$$F = \frac{4 * C_{count}}{\pi * C_{max}^2} \quad \text{Equation 2.2}$$

where  $F$  is the circularity,  $C_{count}$  is the number of pixels in the region, and  $C_{max}$  is the length of the region (Yamaguchi and Hashimoto 2009a). If  $F$  is close to one, the region is circular and thus the focal pixel is not part of the crack, but if  $F$  is close to zero, then the region is linear and the focal pixel is part of the crack (Yamaguchi and Hashimoto 2009a). Figure 12 shows an example of the percolation process when the focal pixel is in the background, and when it is part of the crack.



Figure 12: Percolation Technique: a) Focal Pixel in the Background; b) Focal Pixel in the Crack

#### 2.4.1 State of Practice – Concrete Crack Detection

Image processing techniques used in identifying and analyzing cracks in concrete bridge decks can also be found in the analysis of other common infrastructures. Underground pipelines pose an issue for inspectors to accurately analyze the cracks. In 2005, experiments were conducted using an algorithm that uses a geometry-based image modeling concept to segment the cracks (Iyer and Sinha 2005). The authors used an algorithm that concentrated on dark regions of images and implemented filters that included features such as constant width and tree-like features (Iyer and Sinha 2005). Another infrastructure conducive to cracking is sewers. In 2014, cracks were detected

using an algorithm consisting of Sobel edge detection to identify possible crack fragments, the Hough transform to remove errant edges, morphological operations to enhance the possible cracks, and then a filtering mechanism to remove noise (Halfawy and Hengmeechai 2014). In 2007, a mobile robot inspection system was created in South Korea to analyze cracks within a tunnel (Yu et al. 2007). The other most common infrastructure conducive to cracking is asphalt roadways. In 2014, researchers developed an algorithm to help detect cracks on roadways using fragment grouping by dilation and fragment connection by thinning processes (Wu et al. 2014).

Some of the image processing techniques are even used in the medical field for segmenting cartilages and neurons. In 2006, studies were conducted on extracting cartilage surfaces and computing their thicknesses through complicated algorithms that use gradient vector flow snakes to segment the image (Tang et al. 2006). Studies have been done on segmenting neurons by using a technique called tubularity flow field, which perform regional growing guided by the direction of the tubularity and by also using an attraction force based motion (Mukherjee et al. 2014). The active contour model technique has also been used in concrete crack detection. The Chen-Vese Active Contour model was used to segment cracks because it can automatically detect and evolve its contours and it has the capability of extracting geometric properties of the crack (Chen & Hutchinson, 2010).

Percolation has also been used. Zhu et al. (2011), used an algorithm based on percolation models to evaluate concrete structures after an earthquake. Unlike typical percolation models, this algorithm performed percolation on pixels with high gradient magnitudes (Zhu et al. 2011).

Another percolation algorithm was developed to detect the cracks on concrete surfaces, then the cracks were dilated and thinned before being measured (Yamaguchi and Hashimoto 2009b).

Other researchers have decided to rely solely on basic digital image processing techniques, such as morphological operations, thresholding, and edge detection. In 2001, microcracks were analyzed within a concrete structure by putting red dye into the cracks to increase contrast. Then once the image had been taken they were post-processed using erosion and closing operations and thresholded based off of the entropy of the image (Ammouche et al. 2001). In 2003, Abdel-qader et al. (2003) compared multiple edge detections and their relation to identifying cracks on bridges. The edge detection methods analyzed included the Sobel edge detector, the Canny edge detector, the Fourier transform, and the Fast Haar transform. It was found that the Fast Haar transform performed better than both the Sobel and Canny edge detectors while the Fourier transform performed the worst (Abdel-qader et al. 2003).

Similarly, Lattanzi and Miller compared various methods for segmenting concrete cracks (2014). The methods included a clustering method based on k-means, a clustering method based on k\*-means, Canny edge detection, and Haar wavelet filtering. The k\*-means clustering method was developed as an improvement of the k-means method (Lattanzi and Miller 2014). The k-means method is an iterative partitioning method that separates an image into different clusters (MathWorks 2015). The k\*-means algorithm began with specifying a certain number of clusters and setting the initial value to bright pixels. It then proceeded to assign each pixel to a cluster, set a new cluster value based on the average value of pixels within the cluster. It repeated this until the cluster value remained the same. The cluster with the lowest value was segmented. It was found

that the clustering method was more robust than the Canny edge detection or the Haar wavelet filtering (Lattanzi and Miller 2014).

An extremely accurate crack detection algorithm was developed by Fujita and Hamamoto (2011). The structure of their algorithm can be seen in Figure 13.



Figure 13: Crack Detection Algorithm by Fujita and Hamamoto (Adapted from Fujita & Hamamoto, 2011)

The subtraction-preprocessing step subtracts the original image from the corrective image, which is obtained by applying a median filter to the original image. The multi-scale line emphasis uses a line filter based on the Hessian matrix. The Hessian matrix is the partial second derivative of the image. The eigenvalues found from this matrix can describe the difference between structures, such as a line or a blob structure (Fujita and Hamamoto 2011). If the eigenvalues are about zero then the structure is considered line-like, while if they are greater than zero the structure is considered blob-like. This helps eliminate stains and aggregates from the image because they typically have blob-like structures. The image then undergoes probabilistic relaxation, which helps eliminate noisy data. Finally, adaptive thresholding is used to segment the image. The adaptive thresholding is not susceptible to lighting variations like the global thresholding methods, however, it is very computationally expensive (Fujita and Hamamoto 2011).

Another accurate crack detection algorithm that was not computationally expensive, was developed by Jahanshahi et al. (2011). The structure of their algorithm can be seen below in Figure

14. The authors decided to use a line shape for their structuring element because when cracks are perpendicular to the direction of the structuring element, the morphological operations can successfully segment the crack (Jahanshahi et al. 2011).



Figure 14: Crack Detection Algorithm by Jahanshahi et al (Adapted from Jahanshahi et al., 2011)

Segmentation is performed by using the morphological operations of open and close functions. The line-structuring element's size is calculated based on five parameters. The parameters are the distance from the target, the focal length of the camera, the camera sensor resolution, the camera sensor, and the smallest crack size that the algorithm needs to detect. The line-structuring element is then rotated to 0 degrees, 45 degrees, 90 degrees, and 135 degrees. Finally, Otsu's global thresholding is performed on the image. The features extracted include eccentricity, solidity, compactness, the area of the segmented crack divided by the area of an ellipse, and the absolute value of the correlation coefficient. The algorithm effectively segments a crack; however, the ability to detect the crack becomes heavily dependent on lighting conditions. (Jahanshahi et al. 2011)

## **3.0 METHODOLOGY**

---

This section describes the methodology used to conduct experimental testing on the optimal camera parameters needed to resolve various size concrete cracks. Section 3.1 defines the different image acquisition equipment and camera parameters used throughout the experimental testing. Section 3.2 and Section 3.3 details the algorithms utilized to resolve and quantify the concrete cracks. In order to compare the algorithms and the different acquisition systems, three stages of experimental testing were conducted. These stages, described in Section 3.4, include the analysis of simulated cracks, idealized laboratory cracks, and in-service cracks. The experiments conducted on simulated cracks assessed the errors associated with the feature detection and quantification methods used in the algorithms. The experiments conducted on the idealized laboratory cracks evaluated the errors associated with the image acquisition system and camera parameters within a controlled environment. Finally, in-service cracks were analyzed under ideal lighting conditions.

### **3.1 Image Acquisition Equipment**

Multiple image acquisition systems, shown in Table 3 below, were used to capture images of cracks. The cameras provided a range of sensor sizes, sensor types, resolutions, and image wavelengths. The cameras chosen represent commonly available systems.

Table 3: Image Acquisition Systems and Their Properties

	<b>Nikon D610</b>	<b>Canon 7D</b>	<b>Point Grey</b>	<b>Nikon D3200</b>
<b>Electromagnetic Spectrum Region</b>	Optical	Optical	Optical	Near-Infrared
<b>Megapixels</b>	24.3	18	5	24.2
<b>Sensor Size</b>	35.9 x 24 mm	22.3 x 14.9 mm	8.8 x 6.6 mm	23.2 x 15.4 mm
<b>Pixel Pitch</b>	5.95 $\mu\text{m}$	4.29 $\mu\text{m}$	3.45 $\mu\text{m}$	3.84 $\mu\text{m}$
<b>Focal Lengths</b> <b>24 mm</b>	x	x		x
<b>35 mm</b>	x		x	
<b>60 mm</b>	x			x
<b>85 mm</b>	x			x

The electromagnetic spectrum indicates whether the acquisition system used wavelengths within the visible spectrum or just beyond the visible spectrum. The systems that used the visible spectrum were labeled as *Optical*. The optical cameras include the Nikon D610 and the Canon 7D, which are both Digital Single Lens Reflex (DSLR) cameras, and the Point Grey, which is a Charge-Couple Device (CCD) camera. The Nikon D3200 was converted to a near-infrared camera that operates in a wavelength of 715 nm by removing the stock glass in the camera and replacing it with WG280 glass (LDP LLC 2014). The images captured by the converted camera will appear red because red pixels are the most open to the infrared. The Megapixels, Sensor Size, and Pixel Pitch are all dependent on the actual camera.

Megapixels are a unit equal to one million pixels and can be used to measure the resolution of an image. Typically, a higher amount of megapixels results in a higher resolution image. However, if the sensor size is not increased along with the increasing amount of megapixels, the camera will capture a noisier image. The sensor size indicates the amount of surface area a camera has to capture light to create an image. A comparison of the four cameras and their sensor sizes can be

seen in Figure 15. Usually, a larger sensor size leads to a higher quality image. Similarly, a larger pixel pitch, meaning the distance from the center of one pixel to the center of the next pixel, gathers more light resulting in a higher quality image. If there are two cameras with the same sensor sizes but different pixel pitches, the camera with the smaller pixel pitch will produce a noisier image than a camera with a larger pixel pitch.

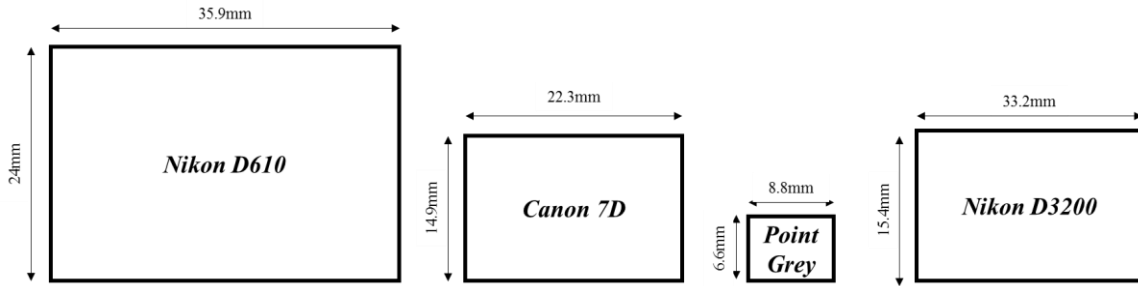


Figure 15: Comparison of Camera Sensor Sizes

The lenses used during experiments were both normal lenses and macro lenses. The macro lens allows the photographer to capture an image that is either half its life size or its actual life size (Nikon, 2015). This can be beneficial when imagining small objects. The lenses used were a macro lens with a 60 mm focal length and a standard lens with a variable focal length between 24 mm to 85 mm.

Table 3 describes the focal lengths that were used with each particular acquisition system. Different focal lengths capture a different field of view. The angle of view, also known as the field of view and shown in Figure 16, can be calculated using the Equations 3.1 and 3.2.

$$\text{Horizontal FOV} = 2 * \tan^{-1}(0.5 * W / FL) \quad \text{Equation 3.1}$$

$$\text{Vertical FOV} = 2 * \tan^{-1}(0.5 * H / FL) \quad \text{Equation 3.2}$$

Where *Horizontal FOV* is the horizontal field of view in degrees,  $W$  is the width of the camera sensor, *Vertical FOV* is the Vertical field of view in degrees,  $H$  is the height of the camera sensor, and  $FL$  is the focal length.

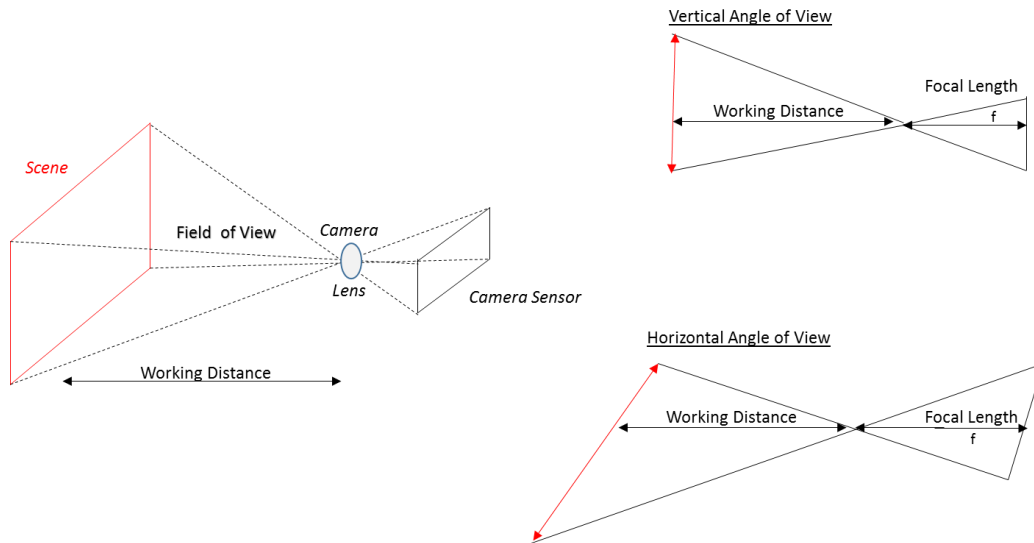


Figure 16: Field of View Diagram

Short focal lengths capture a wide angle of view with lower magnification. While, long focal lengths capture a narrow angle of view and a higher magnification. The longest focal length used during the experiments was 85 mm. and the shortest focal length was 24 mm, as shown in Figure 17.

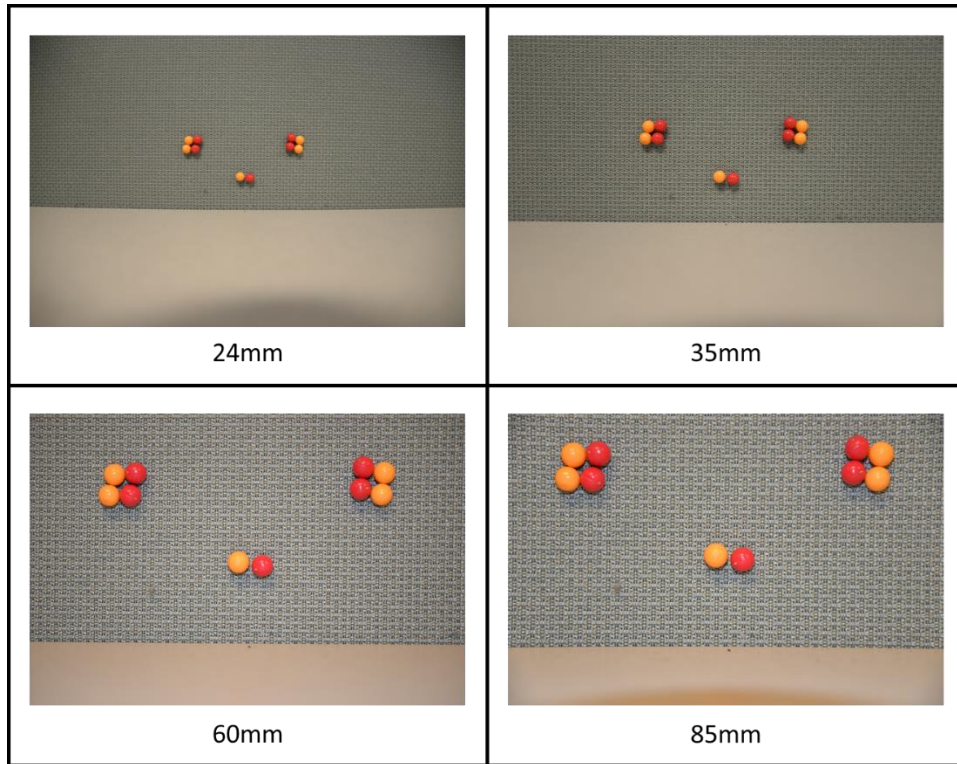


Figure 17: Comparison of Focal Lengths

### 3.2 Feature Detection – Crack Identification

In order to meet the goals of this research, a series of image processing techniques, shown below in Table 4, were evaluated for their potential to locate and analyze crack characteristics in concrete specimens.

Table 4: Previous Crack Detection Methods

<b>Researchers</b>	<b>Method for Segmenting Cracks</b>
Ammouche et al. 2001	Morphological Operations: Erosion and Close Functions
Tung et al. 2002	Edge Detection: Sobel
Abdel-qader et al. 2003	Edge Detection: Canny, Fast Haar, Sobel, and Fast Fourier Transform
Chen et al. 2006	Manual seed points used to create skeletization
Oh et al. 2009	Morphological Operations: Median and Dilation Functions
Yamaguchi and Hashimoto 2009b	Percolation and Morphological Operations: Dilation and Erosion
Yamaguchi and Hashimoto 2009a	Percolation Method
Chen and Hutchinson 2010	Active Contour Model: Chen-Vese
Zhu et al. 2011	Percolation-Based Method
Fujita and Hamamoto 2011	Morphological Operations: Median Function
Jahanshahi et al. 2011	Morphological Operations: Open-Close Function
Jahanshahi and Masri 2012	Morphological Operations: Open-Close Function
Jahanshahi and Masri 2013	Morphological Operations: Open-Close Function
Lattanzi and Miller 2014	Edge Detection, K-means Clustering: Canny, Haar Wavelet, and k*-means
Liu et al. 2014	3D Crack Detection Methods
Torok et al. 2014	3D Crack Detection Methods
Wu et al. 2014	Morphological Operation: Dilation

After the literature review of these techniques, three algorithms were chosen based on their ability to accurately identify concrete cracks under less than ideal environmental scenarios. The first method was adapted from the journal article *An innovative methodology for detection and*

*quantification of cracks through incorporation of depth perception* by Jahanshahi et al. (2011). The second method was adapted from the journal article *A robust automatic crack detection method from noisy concrete surfaces* by Fujita and Hamamoto (2011). The last method was adapted from Lattanzi and Miller (2014) as described in the article *Robust automated concrete damage detection algorithms for field applications*. Finally, the author created an algorithm for detection that combined the work from Jahanshahi et al. (2011) and Fujita and Hamamoto (2011). After the cracks were identified their width and length were calculated using a distance transform method. It should be noted that none of the code for the methods was provided by the sources, but rather, were created using the processes described within the articles. The MATLAB codes used during the experiments is provided in Appendix E of this thesis.

### **3.2.1 Jahanshahi Adapted Method**

The first algorithm, adapted from Jahanshahi et al. (2011), segments cracks based on the camera parameters used during the acquisition of the image. The camera parameters needed to use this algorithm are focal length, working distance, number of megapixels, and the sensor size of the camera. The algorithm also assumes that the image was captured perpendicular to the object of interest.

The steps used in feature detection are as follows:

1. Convert the image to grayscale
2. Select a line structuring element and define its size by using the developed equation

$$S = FL/WD \times SR/SS \times CS \quad \text{Equation 3.3}$$

where  $S$  is the size of the structuring element in pixels,  $WD$  is the distance from the target in mm,  $FL$  is the focal length of the camera in mm,  $SR$  is the number of megapixels,  $SS$  is

the camera sensor size in mm, and  $CS$  is the crack size in mm. The minimum crack size of interest should be used in calculating the size of the structuring element. This ensures the small cracks will not be removed from the image.

3. To remove non-crack like features from the image, perform open and then close functions with the line structuring element rotated at 0 degrees
  - a. Repeat the open and then close functions with the line-structuring element rotated at 45 degrees, 90 degrees, and 135 degrees. An illustration of the outcomes of open and then close functions are shown in Figure 18 (Acton 2013).

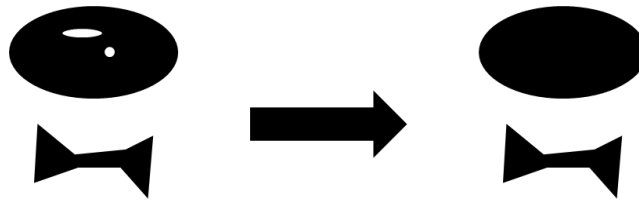


Figure 18: Example of Open-Close Functions (Adapted from Acton 2013)

4. Perform Otsu's global thresholding to convert the grayscale image to a binary image.

The complete method is illustrated in Figure 19. The red boxes are placed to show how a line-structuring element would move through the image. Typically, the element would start in the left top corner of the image and make its way to the bottom right corner. The first round would have the line element rotated to 0 degrees; it would move through the whole image while performing open and then close functions, which are discussed in Section 2.4. The line structuring element would then be rotated to 45 degrees and begin the process again. This would be repeated for the remaining two rotations. Finally, the results from each rotation would be added together and thresholded to produce the binary image shown.

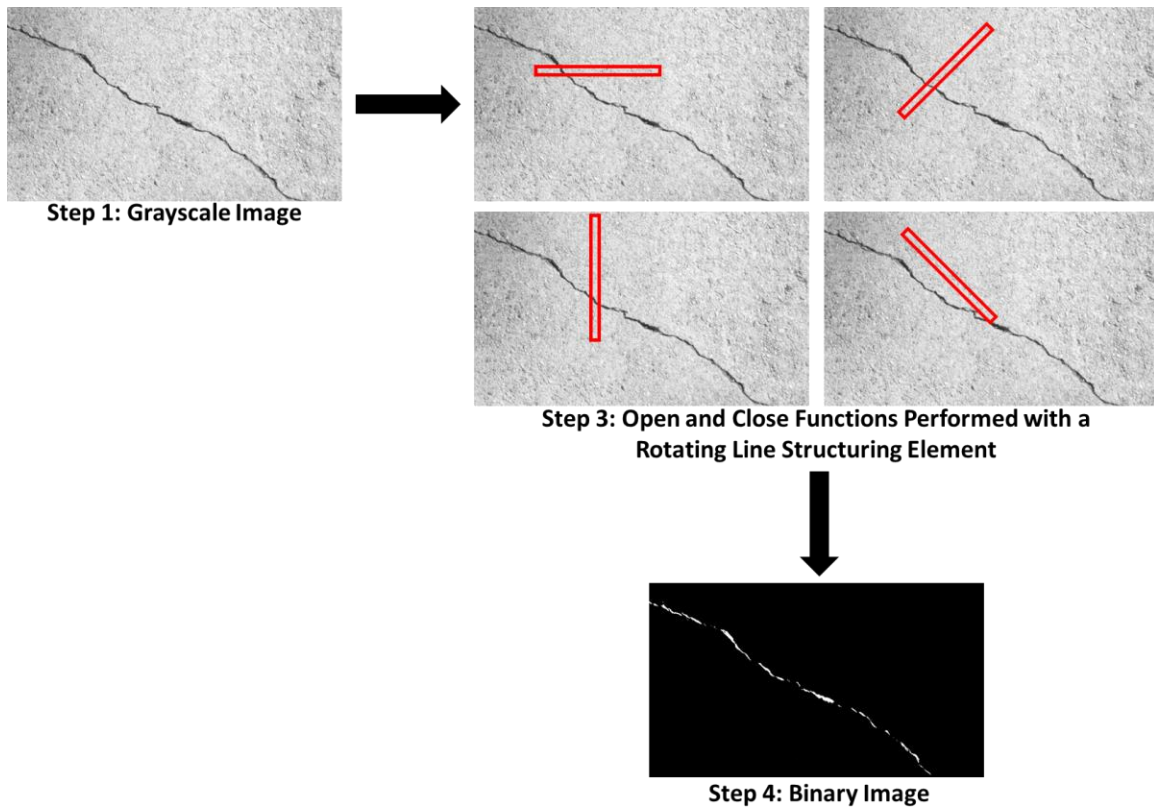


Figure 19: Illustration of the Jahanshahi Adapted Method

### 3.2.2 Fujita Adapted Method

The second algorithm, adapted from Fujita and Hamamoto (2011), was developed to detect cracks in noisy concrete conditions. Noisy concrete images include concrete that has stains, aggregates visible on the surface, or shading.

The steps used in feature detection are as follows:

1. Convert the image to grayscale
2. Apply a median filter to the grayscale image and then the original image is subtracted from the median filtered image.
3. The image undergoes a multi-scale line emphasis, which uses a line filter based on the Hessian matrix. Typically, noise in concrete images comes from stains or aggregates,

which have blob-like structures. The multi-scale line emphasis will help eliminate these components.

4. The image then undergoes probabilistic relaxation; this will help eliminate any other noisy data from the image. For probabilistic relaxation, it is set so that an image would undergo a variable amount of iterations and that the pixels could only be placed into either two categories, background or crack. The probability of a pixel being part of a crack can be seen below:

$$P = \frac{\log(R(x_i)+1)}{\log(R_{max}+1)} \quad \text{Equation 3.4}$$

where  $P$  is the probability of being a crack,  $R_{max}$  is the maximum pixel value of an image, and  $R_i$  is the value at that specific pixel. The probability of a pixel being in the background is found by subtracting  $P$  from 1.

5. Implement Wellner's Adaptive Threshold Method to segment the image (Wellner 1993). The adaptive threshold method used a filter size one thirtieth of the image size and used Gaussian smoothing. Upon experimentation, it was found that the local threshold is set between 30 and 40 percent of the local average gray value.

The complete method is illustrated in Figure 20. The median filter smoothed the image and when subtracted from the original image, the crack appeared as the main component of the picture. After the multi-scale line emphasis and the probabilistic relaxation, the crack was identified as the foreground and the rest as the background. Finally, the results were thresholded to produce the binary image shown in Figure 20.

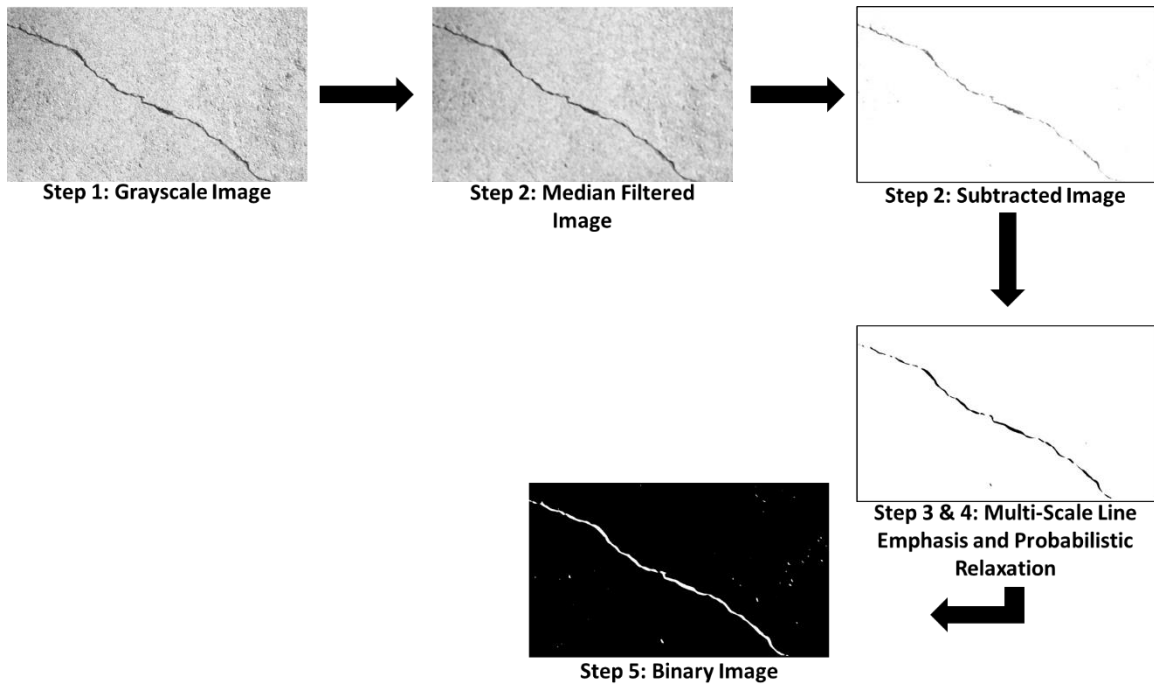


Figure 20: Illustration of the Fujita Adapted Method

### 3.2.3 Lattanzi Adapted Method

The third algorithm use the  $k^*$ -means method developed by Lattanzi and Miller (2014). The authors recognized that cracks typically appear in the darker areas of an image. Using that knowledge, they developed a  $k^*$ -means method, which improves upon the  $k$ -means algorithm, which is a clustering based method.

The steps used in feature detection are as follows:

1. Convert the image to grayscale.
2. Perform histogram equalization to lessen lighting variations in the image. This enhances the contrast between the crack and the concrete.
3. Choose a number of clusters to use and skew the initial cluster values to bright pixel values using logarithmic spacing. In their paper, they used 10 clusters. However, upon corresponding with the authors it was disclosed that the number of clusters should be

between 6 and 12. Six clusters proved to be optimal in computational time and accuracy for this research project.

4. Assign the pixels in the image to a cluster and then set the cluster value to match the average pixel value in the respective cluster.
5. Compare the new cluster value to the old cluster value. If the cluster values have changed, repeat the algorithm. If the cluster values have not changed, select the cluster with the lowest value.
6. Segment the image using Otsu's global thresholding method.

The complete method is illustrated in Figure 21. The histogram equalization darkened the crack, making it easier to segment. Then the image was assigned into clusters and iterated until the cluster values did not change. The clustering image shows the final clusters separated by color. Finally, the results were thresholded to produce the binary image shown.

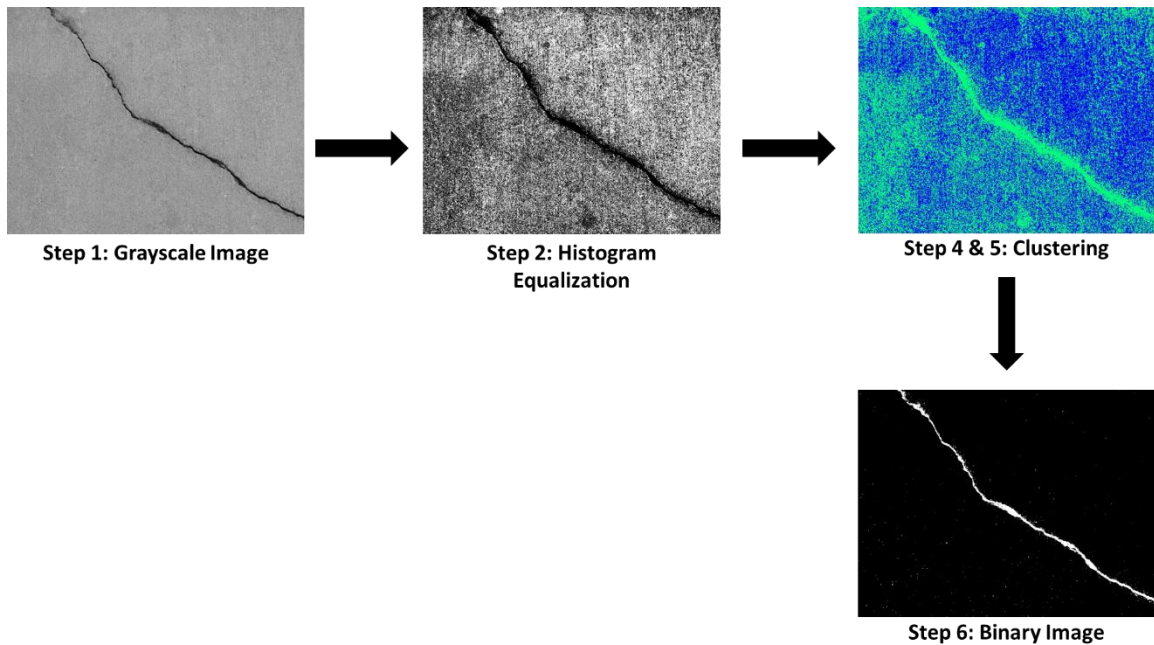


Figure 21: Illustration of the Lattanzi Adapted Method

### 3.2.4 Combined Algorithm

The final algorithm, called the Combined Algorithm, was developed by combining techniques described in Section 3.2.1 and Section 3.2.2. The line structuring element equation from the Jahanshahi Adapted Method and their morphological operations are combined with Fujita Adapted Method's adaptive local threshold idea.

The steps used in feature detection are as follows:

1. Convert the image to grayscale
2. Select a line-structuring element and define its size by using Equation 3.3, outlined in Section 3.2.1. As with the other method, the minimum crack size of interest should be used in calculating the size of the structuring element. This ensures the small cracks will not be removed from the image.

3. To remove non-crack like features from the image, perform open and then close functions with the line structuring element rotated at 0 degrees
  - a. Repeat the open and then close functions with the line-structuring element rotated at 45 degrees, 90 degrees, and 135 degrees.
4. Implement the adaptive threshold method described in Section 3.2.2. The adaptive threshold method used a filter size one thirtieth of the image size and used Gaussian smoothing. Upon experimentation, it was found that the local threshold is set between 30 and 40 percent of the local average gray value.

The complete method is illustrated in Figure 22. The line structuring element in combination with the open and close functions move through the image and produce the results shown. These results are then added together and thresholded to produce a binary image, where the crack is shown in white and the background is black.

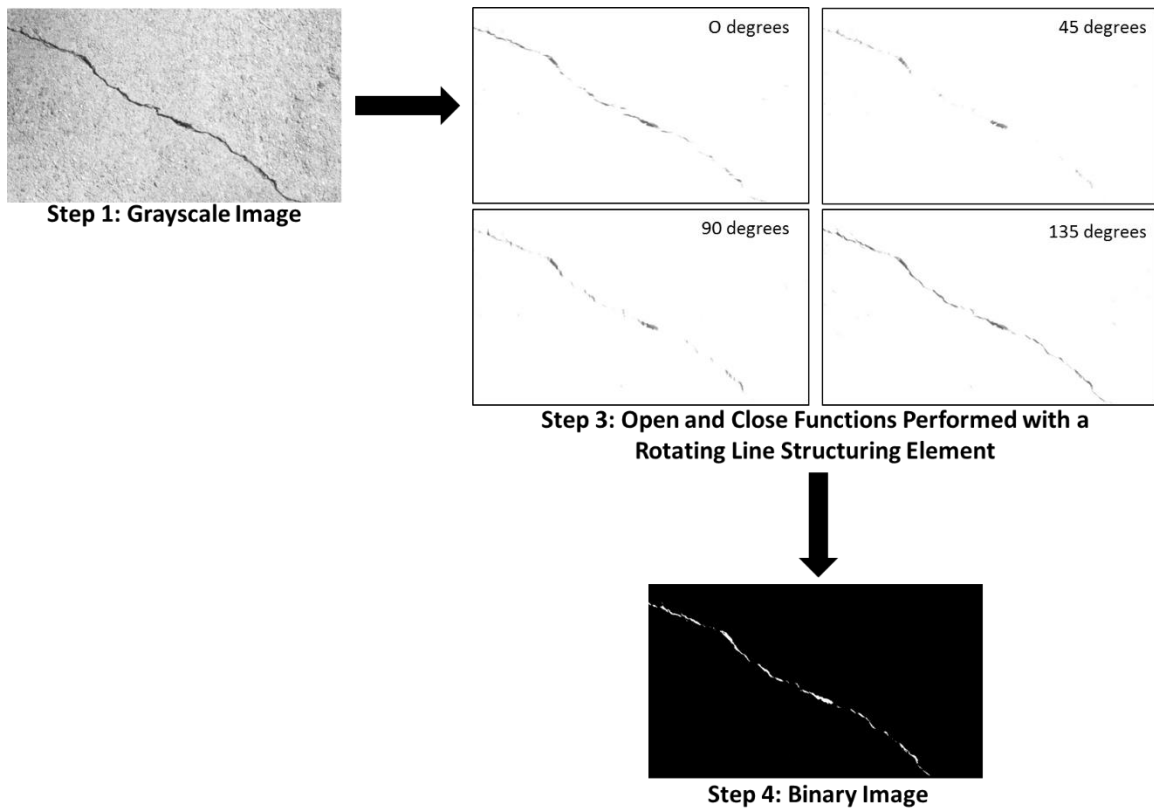


Figure 22: Illustration of Combined Algorithm

### 3.3 Feature Evaluation – Crack Measurement

In addition to detecting crack features, an algorithm was used to quantify crack dimensions. The dimensions of interest included width and length of the crack.

The steps used in feature evaluation are as follows:

1. Calculate the orientation of the feature detected. The orientation is specified as the angle between the x-axis and the major axis of an ellipse that is generated from the second moments of the object region (MATLAB, 2013). Figure 23 illustrates this process.

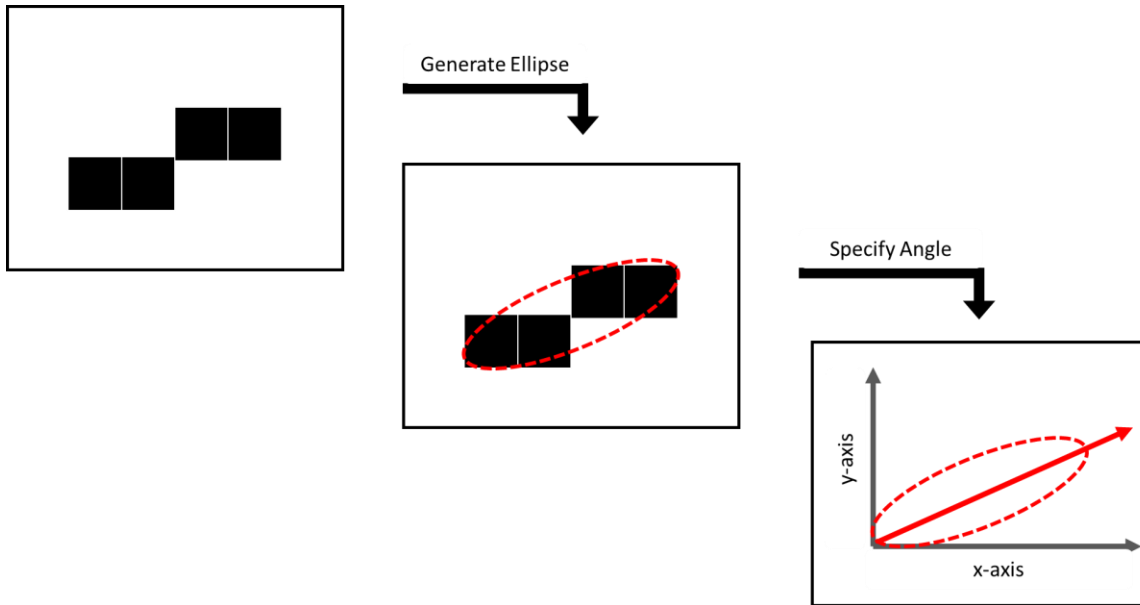


Figure 23: Calculating Object Orientation (Adapted from MATLAB, 2013)

2. Rotate the object until it has an orientation of zero degrees. This helps reduce the errors of miscalculating distances due to the stair step effect of pixels when the crack is at angle, as shown below in Figure 24.



Figure 24: Example of Stair-Step Pixels

3. Use the Euclidean distance transform to calculate the straight line distance between two pixels by using Equation 3.5:

$$\text{Distance Transform} = \sqrt{(x_1 - x_2)^2 + (y_1 - y_2)^2} \quad \text{Equation 3.5}$$

The values of  $x_1$ ,  $x_2$ ,  $y_1$ , and  $y_2$  are dependent on the dimension being measured. Figure 25 shows the values used when measuring both thickness and length. The left image is calculating the amount of pixels in length and the right image is calculating the amount of pixels in width.

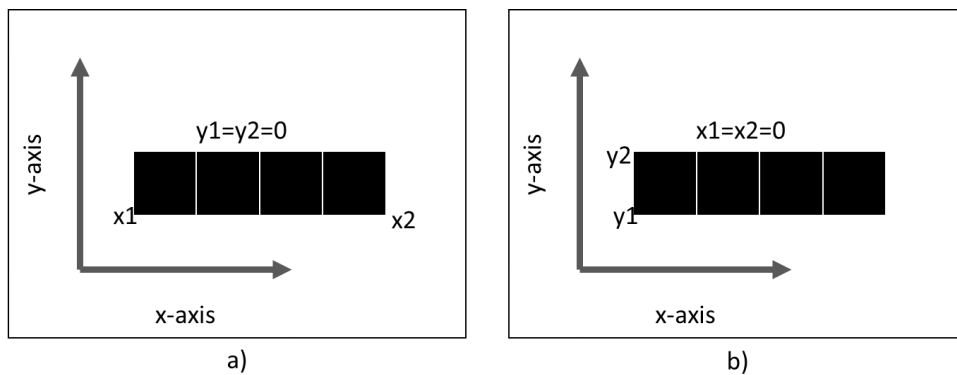


Figure 25: Euclidean Distance Transform

### 3.4 Experimental Testing

To meet the goals of this research in assessing optimal camera parameters needed to resolve various concrete cracks, a series of experiments were conducted. The experiments can be described in three stages and in each stage the camera captured static images. The first stage primarily assesses the ability of the selected algorithms to detect and accurately analyze geometric features of simulated cracks. These experiments isolated errors that were solely due to the feature detection and quantification from the methods used in the algorithms. The second stage of experiments used ideal laboratory cracks to assess environmental errors within a controlled setting. In this stage, multiple experiments were conducted to test different acquisition systems, focal lengths, and working distances. The final stage of experiments analyzed in-service cracks under ideal lighting

conditions. Ideal lighting conditions are defined as an area that is illuminated with no shadows present.

### 3.4.1 Simulated Cracks

In order to measure the amount of error produced from the code itself, ideal cracks were created in MATLAB (2013). The steps used in creating simulated cracks are as follows:

1. Select crack dimension, working distance, and image acquisition system that will be used to capture data.
2. Calculate the amount of pixels needed for a specified crack dimension using the equation below:

$$\text{Pixels} = \frac{FL}{PP} \times \frac{CV}{D} \quad \text{Equation 3.6}$$

where *Pixels* is the number of pixels occupied by the object, *FL* is the focal length in mm, *PP* is the pixel pitch in mm, *CV* is the dimension of the crack being measured in mm, and *D* is the working distance from the crack in mm.

3. Because a computer cannot read fractions of a pixel, all calculated pixels found in step 2 need to be rounded to the nearest whole number.
4. Create a rectangle matrix in MATLAB using the dimensions found in step 3.
5. Analyze the matrix using the image processing techniques outlined in Section 3.2 and Section 3.3.
6. Repeat steps 1 through 5 for multiple crack dimensions, working distances, focal lengths, and image acquisition systems.

This process calculates how many pixels a crack will occupy when imaged with a specified acquisition system and focal length. For example, the amount of pixels needed for crack specimens

analyzed with the Nikon D610 and a 24 mm focal length can be seen in Table 5. Additional tables for the pixel requirements of other focal lengths and cameras can be seen in Appendix A. An example of a simulated crack is shown in Figure 26. This crack has a total length of 448 pixels and a total width of 28 pixels.

Table 5: Pixel Requirements for the Nikon D610 with a 24mm Focal Length

<b>Nikon D610</b>						
	<b>3 ft</b>	<b>4 ft</b>	<b>5 ft</b>	<b>6 ft</b>	<b>7 ft</b>	<b>8 ft</b>
<b>Crack Width</b>						
<b>0.250 in</b>	28.01	21.01	16.81	14.01	12.00	10.50
<b>0.125 in</b>	14.01	10.50	8.40	7.00	6.00	5.25
<b>0.060 in</b>	6.72	5.04	4.03	3.36	2.88	2.52
<b>0.020 in</b>	2.24	1.68	1.34	1.12	0.96	0.84
<b>Crack Length</b>						
<b>4 in</b>	448.18	336.13	268.91	224.09	192.08	168.07
<b>6 in</b>	672.27	504.20	403.36	336.13	288.12	252.10

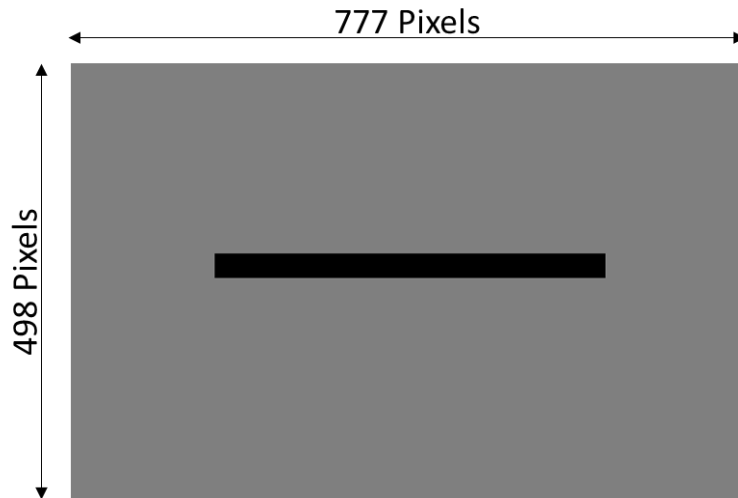


Figure 26: Simulated Crack

### 3.4.2 Idealized Laboratory Cracks

The first series of physical experiments were performed in a laboratory environment. The idealized cracks were created in AutoCAD (2014) which allowed for the creation of features with precise lengths and thicknesses. Using the approach a total of seven specimens were created with the geometric properties shown in Table 6. The Teaching Laboratory in the Civil Engineering Department at the University of Virginia was used to conduct the experiments. The lighting in this space is primarily derived from artificial lighting sources, fluorescent lighting to be exact, with an average light intensity of 500 lux. The simulated cracks were printed on white paper, creating an idealized black and white pattern, where the crack was represented in black and the background in white. The cracks can be seen in Appendix A. The intent of the idealized image was to remove the errors associated with environmental noise and provide a measure of the imaging performance. The following subsections describe the structure and format of the experiments presented in Table 7 and Figure 27.

Table 6: Geometric Properties of Ideal Laboratory Crack Specimens

<b>Ideal Laboratory Specimens</b>		
	<b>Width (in)</b>	<b>Length (in)</b>
<b>Crack 1</b>	0.02	4
<b>Crack 2</b>	0.06	4
<b>Crack 3</b>	0.125	4
<b>Crack 4</b>	0.25	4
<b>Crack 5</b>	0.02	6
<b>Crack 6</b>	0.06	6
<b>Crack 7</b>	0.125	6

Table 7: Experiments Conducted for the Idealized Laboratory Cracks

Idealized Laboratory Crack Experiments						
	Purpose	Camera 1	Camera 2	Specimens Photographed	Focal Length	Working Distances
<b>Exp. 1</b>	Focal Lengths, Working Distances, Crack Geometry	Nikon D610	x	All Specimens	24 mm, 60 mm, 85 mm	3 ft - 8 ft
<b>Exp. 2</b>	Different Sensor Sizes	Nikon D610	Canon 7D	4 in x 0.25 in	24 mm	3 ft - 8 ft
<b>Exp. 3</b>	CCD vs. DSLR	Nikon D610	Point Grey	4 in x 0.125 in	35 mm	1.5 ft, 5 ft, 8.5 ft
<b>Exp. 4</b>	Near-Infrared vs. Optical	Nikon D610	Nikon D3200	6 in x 0.125 in	24 mm	3 ft - 8 ft

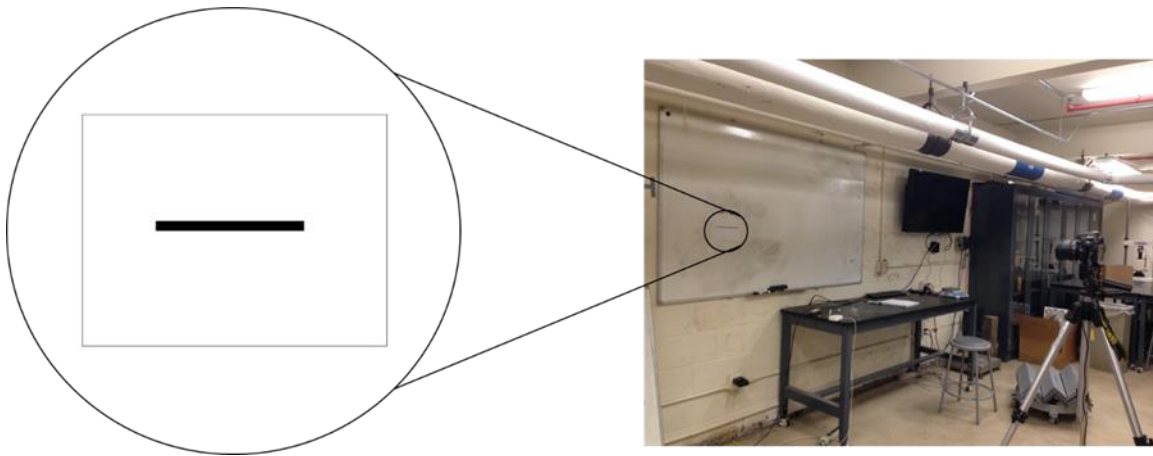


Figure 27: Experimental Set-Up for the Ideal Laboratory Crack Experiments

### 3.4.2.1 Experiment 1 – Crack Geometry, Working Distances and Focal Lengths

Experiment 1, gathered data related to crack dimensions, working distances, and focal lengths. All images were acquired with the Nikon D610. Three different focal lengths were used to compare how focal lengths affect image quality. The specimens were photographed in one-foot increments from 3 ft to 8 ft to determine optimal distances needed to resolve various crack widths. In order to help eliminate systematic errors, each specimen was photographed five times at every distance

with every focal length. The orientation of the specimen was randomized, as shown in Table 8. *D* dictates the crack should be placed at approximately an angle of 45 degrees, *V* dictates the crack should be placed vertically, and *H* dictates the crack should be placed horizontally. This equated to 480 ideal laboratory crack images analyzed for Stage 1. Sample images can be seen in Appendix A.

Table 8: Orientation of Specimens for Experiment 1

	3 ft	4 ft	5 ft	6 ft	7 ft	8 ft
<b>Crack Width: 0.02 in</b>	D	V	H	D	H	D
	D	V	V	V	D	D
	H	V	H	V	V	V
	D	V	V	V	D	D
	H	V	H	V	V	V
<b>Crack Width: 0.06 in</b>	H	D	D	V	H	V
	V	D	H	V	V	D
	H	D	D	V	H	V
	V	D	H	V	V	D
	D	V	H	H	V	H
<b>Crack Width: 0.125 in</b>	V	H	D	H	H	V
	H	H	D	V	H	D
	V	H	D	H	H	V
	H	H	D	V	H	D
	V	H	H	D	D	V
<b>Crack Width: 0.25 in</b>	V	V	D	H	V	D
	H	V	V	H	V	D
	V	V	D	H	V	D
	H	V	V	H	V	D
	D	H	D	H	D	H

The lighting in the laboratory was not consistent for every distance imaged, requiring variation in the aperture for each configuration to restrict the amount of light on the camera sensor. The light

intensity was measured using a handheld light meter, the cal-LIGHT 400, positioned at the camera sensor for each working distance.

To illustrate the effect of light intensity on image quality, Figure 28 includes a comparison of a sample 4 in. by 0.125 in. crack. Changes in the aperture, or size of the opening in the lens, allows for adjustments to the light transmitted to the camera sensor (Nikon, 2015). Aperture is measured and controlled with f-stop values. An f-stop value is the focal length divided by the aperture. An increase in the f-stop value, or a decrease in aperture value, decreases the light resulting in a lower contrast image (Sheppard 2010). Whereas a decrease in f-stop value, or an increase in aperture value, increases the light resulting in a higher contrast image.

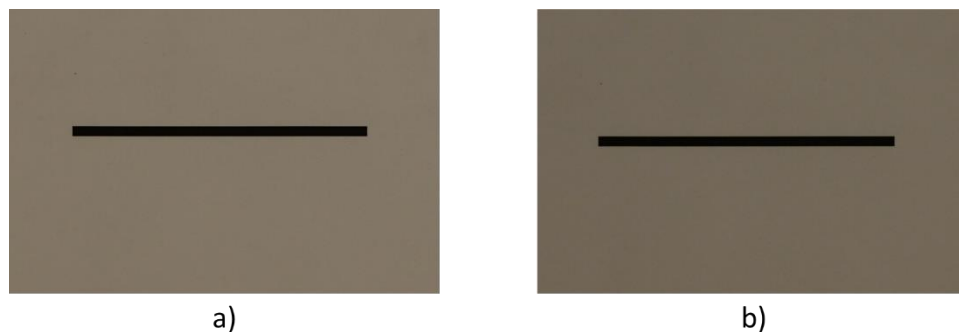


Figure 28: Sample Image of a) F-stop (f/8); b) F-stop (f/14)

### 3.4.2.2 Experiment 2 – Sensor Size Comparison

Experiment 2 compared different sensor sizes by using the Nikon D610, which has 24.2 megapixels, and a Canon 7D, which has 17.9 megapixels. Typically, a larger amount of megapixels provides a more detailed image, but requires more light to fully capture a high quality image of all those details. They will also require more time to capture an image, thus using a tripod becomes necessary to avoid a blurry image (Sheppard 2010). For this experiment, a focal length of 24mm

was used as the specimens were imaged every foot from a distance of 3 feet to a distance of 8 feet. To help eliminate systematic errors, each specimen was photographed five times at every distance equating to thirty images analyzed per camera. Figure 29 shows a comparison of an ideal 4 in by 0.25 in crack imaged at 3 feet. The image on the left was photographed using 17.9 megapixels and the image on the right was photographed using 24.2 megapixels.

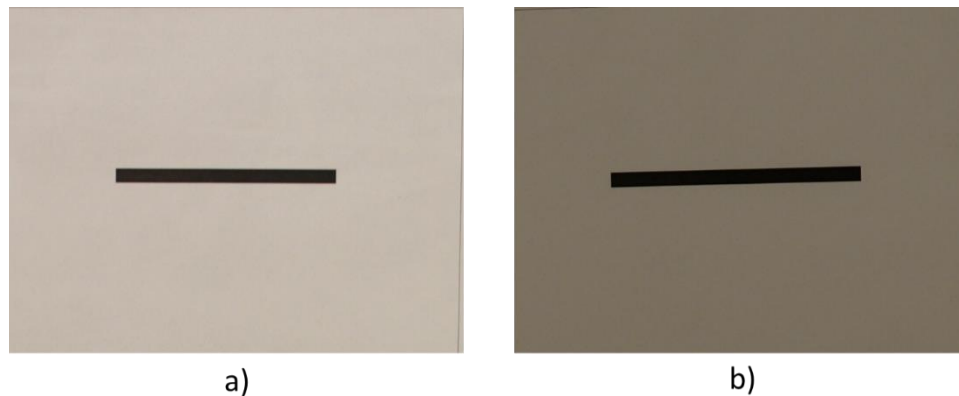


Figure 29: Sample Images of a) 17.9 Megapixels; b) 24.2 Megapixels

### 3.4.2.3 Experiment 3 – CCD versus DSLR

The Nikon D610 uses a complementary metal oxide semiconductor (CMOS) sensor, which is the typical sensor used in DSLR cameras. The Point Grey camera, however, uses a CCD sensor. The CCD sensor transfers every pixel's charge to be converted to voltage, where a CMOS sensor has each pixel convert its own charge to voltage (Litwiller, 2001). The CMOS sensor has a smaller area available for light capture than the CCD sensors. Thus, the CCD sensors tend to be easily overloaded by extreme light. In Experiment 3, a DSLR camera is compared with a CCD camera by using the Nikon D610 and the Point Grey. Due to constraints of the CCD camera, a 35 mm focal length was used and the specimen was only imaged at the distances of 1.5ft, 5ft, and 8.5ft. To help eliminate systematic errors, each specimen was photographed five times at every distance

equating to fifteen images analyzed per camera. Figure 30 shows a comparison of an ideal 4 in by 0.125 in crack imaged at 5 ft. The image on the left was photographed using the CCD camera and the image on the right was photographed using the DSLR camera.

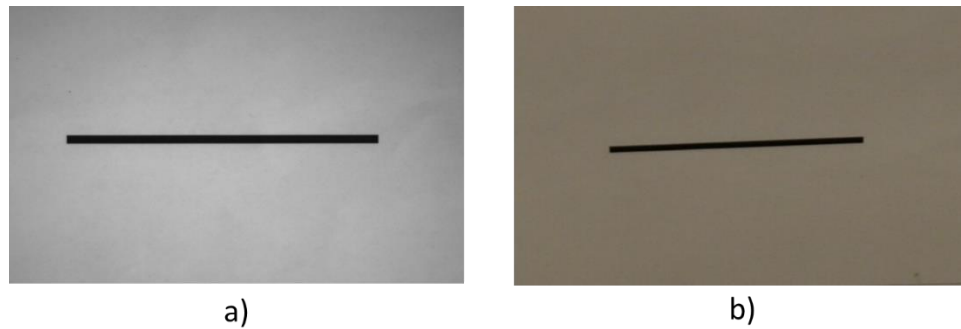


Figure 30: Sample Images of a) CCD Camera; b) DSLR Camera

#### **3.4.2.4 Experiment 4 – Comparison of Near-Infrared Cameras and Optical Cameras**

Using the near-infrared spectrum allows the acquisition system to capture an image using a wavelength just beyond what the human eye can see. However, the conversion of a camera to the near-infrared spectrum can also cause distortions when an image is taken. The common distortions include having out of focus pictures around the corners when using a wide-angle lens, not being able to focus the near infrared light as sharply as focusing the visible light, and light bouncing inside a camera when shooting with a small aperture.

Experiment 4 compared the near-infrared camera to the optical camera. A focal length of 24mm was used as the specimens were imaged every foot from a distance of 3 feet to a distance of 8 feet. The largest F-stop used with the near infrared was f/20. To help eliminate systematic errors, each specimen was photographed five times at every distance equating to thirty images analyzed per camera. Figure 31 shows a comparison of an ideal 6 in by 0.125 in crack imaged at 5 feet with the

near-infrared camera and an optical camera. The image on the left was photographed with the Nikon D3200 and the image on the right was photographed with the Nikon D610. Both used an F-stop value of f/20.

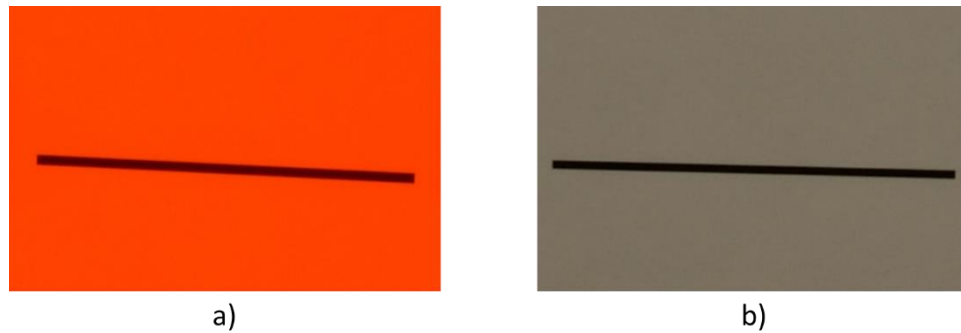


Figure 31: Sample Images of a) Nikon D3200; b) Nikon D610

### 3.4.3 In-Service Cracks

The last experiment imaged in-service cracks with the Nikon D610 camera and the Near-Infrared Nikon D3200 camera. Both cameras used a focal length of 24 mm. at a working distance of 3 ft. A sample pair of images is shown in Figure 32, where the Nikon D610 took the left image and the Near-Infrared Nikon D3200 took the right image. Images of the other specimens can be seen in Appendix A.



Figure 32: Sample Sidewalk Crack Images: a) Optical Image; b) NIR Image

Each crack specimen was measured in the field using a crack card and a ruler. The measurement values can be seen in Appendix A. The analysis then compared the selected image processing techniques' ability to detect the given crack. For the cracks that could be detected, their geometric properties were found using the process outlined in Section 3.3.

The following steps were used to compare the detection abilities of the selected image processing technique:

1. Convert the image to grayscale
2. Manually segment the image, using the MATLAB (2013) 'roipoly' function. An example can be seen in Figure 33.

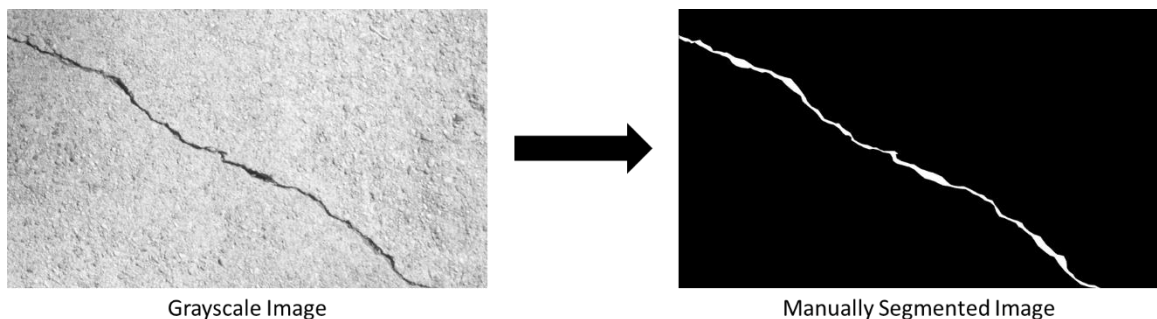


Figure 33: Example of Manually Segmented Image

- a. Use Equation 3.5 to determine the geometric properties of the crack. Compare these findings to the measurements taken in the field. If they are similar, proceed to Step 3. If they are not similar, re-segment the crack.
3. Process the grayscale image using the selected image processing technique
  4. Subtract the processed image from the manually selected image. The subtraction process visually represents the differences between the two images, as shown in Figure 34. If two

images are the same, the subtracted image will appear black, but if they are not the same, the differences will appear in white. The white pixels are considered residual pixels.

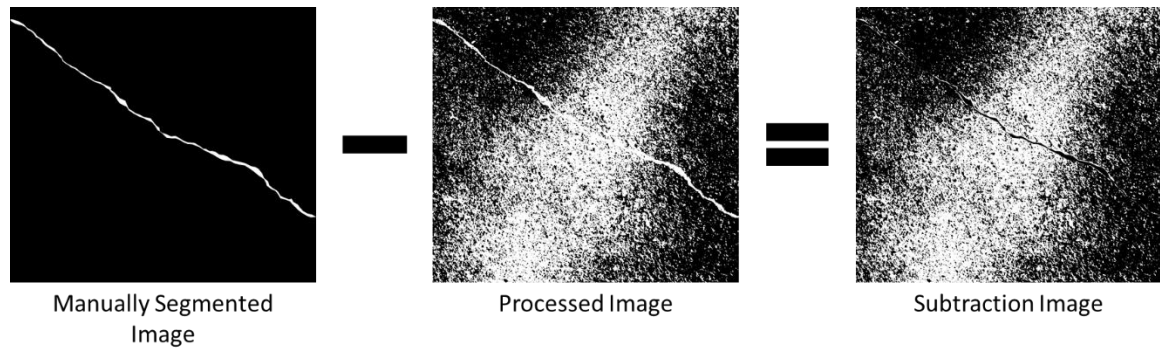


Figure 34: Example of Subtracting Images

5. Count the amount of residual pixels.

### 3.5 Summary of Methodology

The experiments discussed in this section were selected to analyze multiple camera parameters and track where errors occur while acquiring and analyzing an image. The simulated cracks show the amount of error inherent to the image processing while the idealized laboratory cracks and the in-service cracks illustrated the impact of image acquisition and environmental factors have on the quality of an image and therefore the measurement of the crack feature.

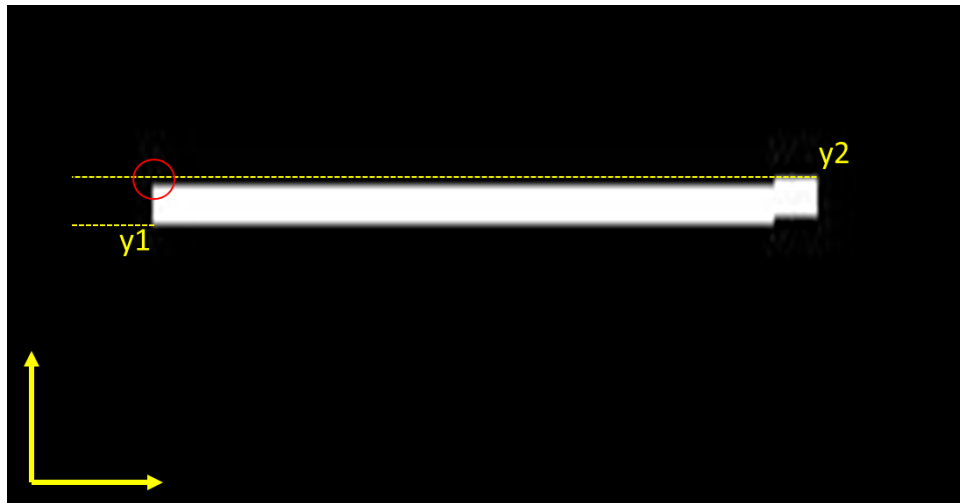
## **4.0 RESULTS**

---

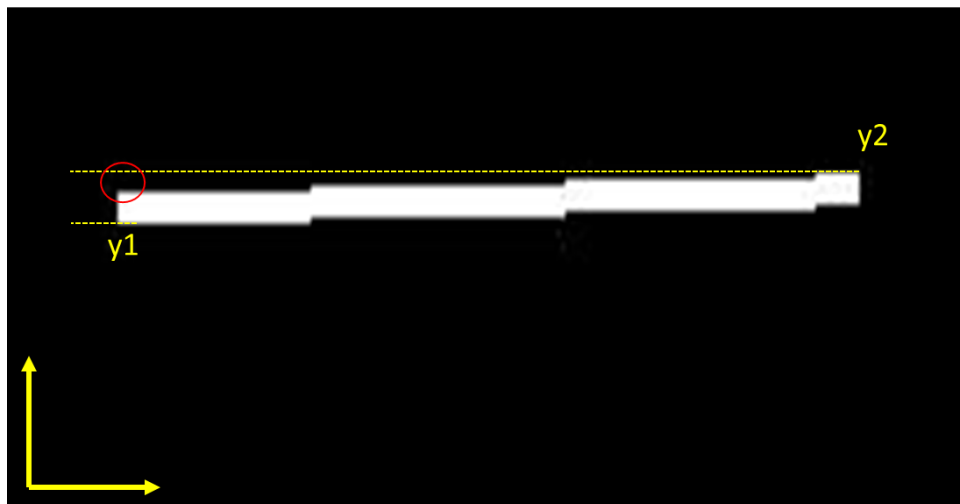
Presented in this section are the results from experimental testing conducted to assess the optimal camera parameters needed to resolve various concrete cracks. The first section details the findings of analyzing geometric features of simulated cracks. The second section presents the results of experiments conducted under ideal laboratory conditions and the final section details the findings of the in-service crack experiment.

### **4.1 Simulated Crack Results**

After the simulated cracks were created, three random specimens were chosen to analyze the effect rotation had on accurately calculating the width of the crack. The three widths chosen were 28-pixel, 11-pixel, and 5-pixel. The cracks began at zero degrees and were rotated up to one degrees. Rotation is known to cause a stair-step effect, discussed in Section 3.3, which can lead to errors when quantifying the dimensions of cracks. Figure 35 shows the stair-step effect for both the 5-pixel specimen when rotated 0.2 degrees and 1 degrees. The red circle on each of the images shows a gap between the true width and the calculated width.



a)



b)

Figure 35: Example of Rotation Errors: a) 0.2 degrees; b) 1 degrees

The rotation errors due to the stair-step effect, as shown in Figure 36, were calculated by using Equation 4.1.

$$\text{Rotation Error} = \frac{(PK - PF)}{PK} \times 100 \quad \text{Equation 4.1}$$

where  $PK$  is the amount of known pixels and  $PF$  is the amount of pixels calculated by the distance transform after the simulated crack was rotated. The results, shown in Figure 36, showed that even

the smallest amount of rotation caused errors. As shown in Figure 36, a rotation of 0.2 degrees causes the 5-pixel specimen to have an error of 20 percent and a 28-pixel specimen to have an error of 7 percent. Larger rotations produced greater errors, and the smaller amount of pixels a specimen required, the larger amount of errors were induced by rotation. The raw data for the rotation experiments can be seen in Appendix B.

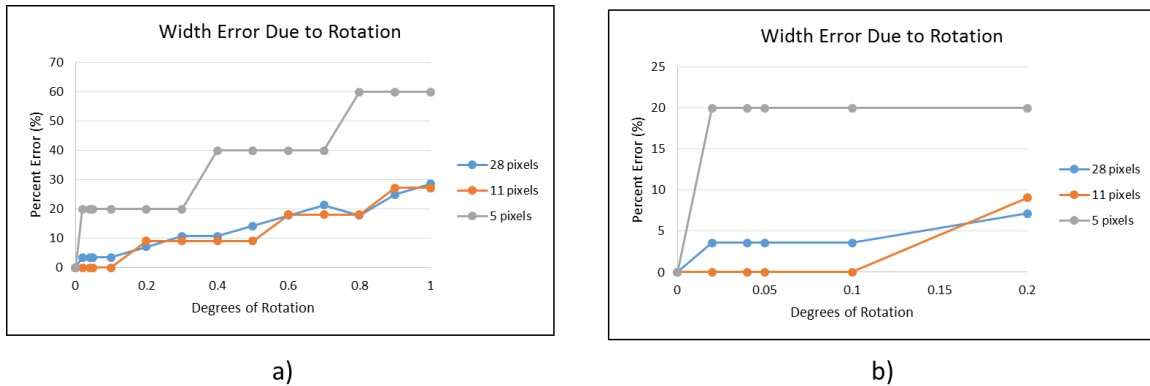


Figure 36: Error Due to Orientation of a Crack: a) Up to 1 degrees; b) Up to 0.2 degrees

The simulated cracks were also used to measure the amount of error produced from the selected image processing techniques. It was found that the chosen image processing techniques did not produce any errors when analyzing the simulated cracks. The errors were induced because the simulated cracks rounded the required amount of pixels to the nearest whole number, as discussed in Section 3.4.1. The process of rounding the pixels resulted in an automatic geometric error, which was calculated using Equation 4.2:

$$\text{Pixel Error} = \frac{\text{Pixels} - PC}{\text{Pixels}} \times 100 \quad \text{Equation 4.2}$$

where *Pixels* is the calculated amount of pixels, using Equation 3.6, for the specified crack dimension, and *PC* is the amount of required pixels rounded to the nearest whole number.

Table 9 shows the amount of required pixels for a 0.25 in crack and for a 0.02 in crack when imaged with the Nikon D610 and a focal length of 24 mm. It also shows the amount of required pixels rounded to the nearest whole number and the resulting pixel error. Additional tables for other focal lengths and cameras can be seen in Appendix B.

Table 9: Example of Calculated Pixel Errors

<b>Crack Width 0.25 in.</b>						
<b>Distance</b>	<b>3 ft.</b>	<b>4 ft.</b>	<b>5 ft.</b>	<b>6 ft.</b>	<b>7 ft.</b>	<b>8 ft.</b>
<b>Required Pixels</b>	28.01	21.01	16.81	14.01	12.00	10.50
<b>Rounded No.</b>	28	21	17	14	12	11
<b>Pixel % Error</b>	0.04	0.04	1.15	0.04	0.04	4.72

<b>Crack Width 0.02 in.</b>						
<b>Distance</b>	<b>3 ft.</b>	<b>4 ft.</b>	<b>5 ft.</b>	<b>6 ft.</b>	<b>7 ft.</b>	<b>8 ft.</b>
<b>Required Pixels</b>	2.24	1.68	1.34	1.12	0.96	0.84
<b>Rounded No.</b>	2	2	1	1	1	1
<b>Pixel % Error</b>	10.75	19	25.63	10.75	4.13	19

The results showed that if a crack had a required amount of pixels that was close to a whole number, the amount of pixel error was relatively small. For example, when the 0.25 in crack was imaged at 3 ft the required amount of pixels was 28.01 and the rounded number of pixels was 28 thus resulting in an error of 0.04 percent. However, if the required amount of pixels was closer to half a pixel the pixel error was larger. For example, when the 0.25 in crack was imaged at 8 ft the required amount of pixels was 10.50 and the rounded number of pixels was 11 thus resulting in an error of 4.72 percent.

The magnitude of the pixel error also increased as the required amount of pixels decreased. This occurred as the crack size decreased and the distance from the crack increased. For example, the

0.02 in crack when imaged from farther than 7 feet had a width that was less than one pixel, thus resulting in a large pixel error. This can be avoided by increasing the focal length, decreasing the working distance, or changing the sensor size.

## 4.2 Ideal Laboratory Results

The following sections outline the results of the experiments conducted under ideal laboratory conditions. The first section defines the type of errors found from the experiments. The next section compares the selected four image processing techniques that were discussed in Section 3.2. The third section compares different variables and their effects on quantifying dimensions of a crack. The variables include focal lengths, crack dimensions, and working distances. The next section compares the different acquisition systems and their ability to accurately detect and quantify crack widths and lengths. The final section discusses the findings related to aperture values and lighting conditions. The raw data for all sections can be found in Appendix C.

### 4.2.1 Definition of Error

Throughout the experiments conducted in the ideal laboratory settings, multiple types of errors were measured. The first type of error was the *pixel error*, which was discussed in Equation 4.1. The next type of error was calculated using Equation 4.3.

$$\text{Processing Error} = \frac{(G - Gf)}{G} \times 100 \quad \text{Equation 4.3}$$

where  $G$  is the known geometric value of the crack specimen and  $Gf$  is the geometric value calculated from the selected image processing techniques described in Section 3.2 and 3.3. This value was calculated for every data point.

Each algorithm has its strength and weaknesses, to create a more average understanding of the errors being produced due to camera parameters, the *processing error* for each image processing technique was averaged using Equation 4.4.

$$\text{Imaged Error} = (C + F + J + L) / 4 \quad \text{Equation 4.4}$$

where  $C$  is the processing error from the Combined Algorithm,  $F$  is the processing error from the Fujita Adapted Method,  $J$  is the processing error from the Jahanshahi Adapted Method, and  $L$  is the processing error from the Lattanzi Adapted Method.

The final type of error calculated was the *environmental error*, which was calculated using Equation 4.5. The *pixel error* exists despite environmental conditions. By subtracting it from the *imaged error*, the effects the environmental conditions had on the ability to accurately quantify a crack's dimensions are isolated.

$$\text{Environmental Error} = \text{Imaged Error} - \text{Pixel Error} \quad \text{Equation 4.5}$$

#### 4.2.2 Comparison of Image Processing Techniques

The crack specimens were analyzed through four image processing techniques, as discussed in Section 3.2. In order to compare the accuracy of each image processing technique, the processing error was averaged over all working distances, focal lengths, and crack widths. Then a one-way analysis of variance (ANOVA) was conducted by using the Fisher Least Significant Difference Method was used to compare the means for each technique (Minitab, 2007). It was hypothesized that the digital image processing techniques varied in mean error. The test had a significance level of 0.05 and all of the data passed the Anderson-Darling Normality Test (Minitab, 2007).

The ANOVA test for a difference in mean processing error produced a p-value of 0.864. Therefore, it could not be concluded that the image processing techniques significantly varied in mean processing error. Table 10 shows the technique and the mean processing error it produced. Similarly, the ANOVA test for the difference in mean processing error concerning length produced a p-value of 0.961. Therefore, it also could not be concluded that, in regards to quantifying length, the mean processing error of the image processing techniques varied.

Table 10: Mean Processing Errors for Calculating Width

<b>Method</b>	<b>Mean Processing Error Width</b>	<b>Mean Processing Error Length</b>
<b>Combined</b>	26.33	8.77
<b>Fujita</b>	33.80	7.87
<b>Jahanshahi</b>	39.26	7.87
<b>Lattanzi</b>	38.15	7.60

#### **4.2.3 Comparison of Crack Geometry, Working Distances and Focal Lengths**

Experiment 1 compared how the crack dimensions, working distances, and focal lengths affected the environmental error for both length and width. All of the ideal specimens were imaged using the Nikon D610 and analyzed with the selected image processing techniques. A factorial design analysis, with an alpha value of 0.05, was conducted to study the effects multiple factors had on the environmental error (Minitab, 2007). The factors analyzed were crack width, focal length, and working distance.

The analysis provided effect values, p-values, and interaction effects. The absolute value of the effect value indicates the relative strength of the factor, while its sign determines the correlation between the factor and the response. A negative effect value indicates that as the factor value is

decreased, the environmental error increases. A positive effect value indicates that as a factor value increases, the environmental error also increases. If the p-value is less than or equal to 0.05 then it can be concluded that the factor has a significant effect on the environmental error. Finally, an interaction effect would occur if the effect one factor has on the response was dependent on the level of another factor. If an interaction effect is found to be significant, the results cannot be accurately analyzed without discussing both of the factors. Table 11 shows the factors, their effect values, and their associated p-values when analyzing the environmental error related to width and length.

Table 11: Factorial Design Analysis Results

Factor	Width Calculations		Length Calculations	
	Effect	P-Value	Effect	P-value
Crack Width	-53.67	0.000	1.545	0.232
Working Distance	5.78	0.54	-6.49	0.000
Focal Length	-16.86	0.035	-8.431	0.000
Interaction: Crack Width & Working Distance	-17.05	0.137	11.817	0.335
Interaction: Crack Width & Focal Length	15.	0.101	-1.668	0.288
Interaction: Working Distance & Focal Length	-26.13	0.026	4.135	0.032

When looking at the width calculations, Table 11 shows that the crack width, the focal length, and the interaction between the working distance and focal length have a significant effect on the environmental error. The effect values suggest that the crack width, with an effect value of -53.67, has the greatest influence on the value of environmental error. It also suggests that as the crack width decreases, shown in Figure 37, the environmental error increases. Similarly, the effect value for focal length suggests that as the focal length is decreased the environmental error increases. However, the interaction effect between working distance and focal length is significant. Therefore, the effect working distance has on the error is dependent on the size of the focal length.

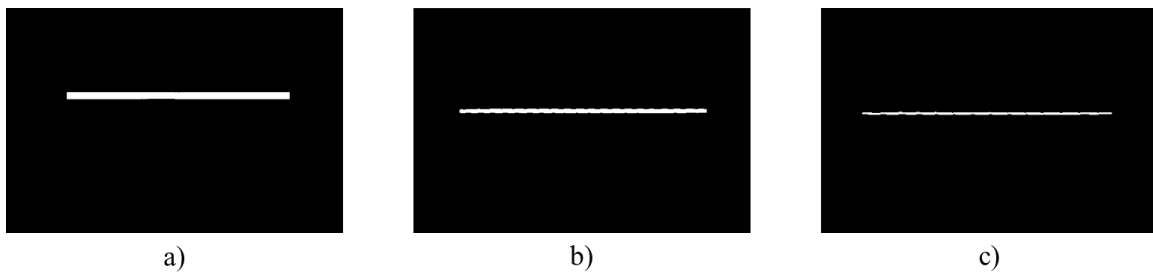


Figure 37: Post Processed Laboratory Cracks: a) 0.125 in; b) 0.06 in; c) 0.02 in

Table 11 shows for the length calculations that the working distance, the focal length, and the interaction between the working distance and the focal length have a significant effect on the environmental error. The effect values for both the working distance and the focal length are negative, thus indicating that as these factors are decreased the environmental errors increase. However, because of the interaction effect being significant, the effect working distance has on the error is dependent on the size of the focal length.

#### 4.2.3.1 Relationship Equation

The factorial design experiment also produced coefficients for each factor analyzed. These coefficients can be used to create an equation, shown in Equation 4.6, which can be used to estimate an expected environmental error. To create a more accurate model the non-significant interactions were removed from the calculation of coefficient values and from the generated equation.

#### Equation 4.6

$$EE = 24.62 - (502.19 * CW) + (10.77 * WD) + (0.65 * FL) - (0.17 * WD * FL)$$

*EE* is the resulting environmental error in percent, *CW* is the crack width in inches, *WD* is the working distance in feet, and *FL* is the focal length in millimeters. This relationship equation only produced an R-squared value of 0.53. The equation, in its present state, does not provide an accurate representation of the amount of environmental error that would be produced; however, the equation can be improved upon. In order to increase the R-squared value more variety needs to be added to the factors. In this experiment, only three focal lengths and six working distances were measured. By increasing the number of focal lengths and working distances used, a revised equation would be created. This new equation would have a more accurate representation of resulting environmental errors and in theory could provide a starting point for choosing the optimum environment to capture an image.

#### 4.2.3.2 Changing Crack Length

A series of crack specimens were also created with a longer length than the original specimens. These specimens were compared to determine if a crack's length affects the ability to quantify its

width and length. Both sets of specimens were analyzed with a 24 mm focal length from distances ranging from 3 feet to 8 feet. The resulting environmental errors were tested for normality using the Anderson-Darling Normality Test, and all data sets were proven normal. Then a t-test was conducted on the data sets to test the hypothesis that the mean environmental error between the longer crack and the shorter crack was significantly different at a 95 percent confidence level. When analyzing the environmental errors related to width, there was not enough evidence to conclude that the means differed at a 0.05 significance level. The analysis of the environmental errors related to length produced the same result. These results showed that the smallest dimension determines the accuracy of quantifying crack dimensions, which in most cases is the crack width.

#### **4.2.4 Comparison of Image Acquisition Systems**

Experiments 2 through 4 compared different acquisition systems. The specified cracks, discussed in Table 7 in Section 3.4.2, were imaged by the various acquisition systems and analyzed with the selected image processing techniques. The following results are broken into two categories, the first details the findings on quantifying a crack's width and the second details the findings on quantifying a crack's length.

##### **4.2.4.1 Accuracy in Quantifying Width**

The environmental error data for quantifying width was tested for normality using the Anderson-Darling Normality Test. All of the data passed the test for normality. A t-test was conducted on the three data sets to test the hypothesis that the mean environmental error between the cameras was significantly different at a 95 percent confidence level. The statistical analysis showed that there was enough evidence to conclude that there was a difference in the mean environmental error

produced from the different sensor sizes. However, in Experiment 3 there was not enough evidence to conclude that the mean environmental error produced when using a CCD camera was different from the mean error produced when using a DSLR camera. Likewise, there was not enough evidence to conclude that the mean environmental error produced when using a near-infrared camera was different from the mean error produced when using an optical camera.

The data was then tested using a factorial design and an alpha value of 0.05 to examine if there were any interaction effects between factors. The factors analyzed were the various working distances and the type of image acquisition system. An interaction effect would occur if the effect the working distance has on the environmental error, were dependent on which acquisition system was used. Table 12 shows the factors, the effect value, and the associated p-values. Negative effect values indicate an inverse relationship, while positive values indicate a direct relationship.

Table 12: Factorial Design Results Regarding Width for Different Image Acquisition Systems

Factor	Experiment 2: 24.2 MP vs. 17.9 MP		Experiment 3: CCD vs. DSLR		Experiment 4: NIR vs. Optical	
	Effect	P-Value	Effect	P-value	Effect	P-value
Working Distance	4.24	0.237	-9.74	0.138	-11.26	0.000
Acquisition System	-10.09	0.002	-2.893	0.473	-0.217	0.849
Interaction: Acquisition System & Working Distance	-13.74	0.003	1.61	0.729	1.763	0.305

For Experiment 2, the t-test had proven there was a significant difference between mean error values. The factorial design test showed that a decrease in megapixels leads to an increase in environmental error. However, the test also showed that, at a 95 percent confidence level, the interaction of the working distance and the acquisition system are significantly dependent on one

another. This indicates that, despite having a low p-value for the acquisition system, the effect the amount of megapixels has on the environmental error is dependent on the working distance. Unlike the results for the sensor size comparison, Experiment 3 and Experiment 4 showed that there was not a significant interaction between the working distance and the type of acquisition system used to image the specimens.

#### **4.2.4.1 Accuracy in Quantifying Length**

As with the environmental error data for quantifying width, the environmental error data for quantifying length was tested for normality using the Anderson-Darling Normality Test and all of the data passed. A t-test was conducted on the three data sets to test the hypothesis that the mean environmental error between the cameras was significantly different at a 95 percent confidence level. The statistical analysis produced results similar to the width analysis. Experiment 2 had enough evidence to conclude the mean environmental errors differed, while Experiment 3 and Experiment 4 did not have enough evidence to conclude that the means differed.

A factorial design analysis was also conducted, with an alpha value of 0.05, to study the effects that working distance and type of image acquisition system had on the accuracy of quantifying crack length (Minitab, 2007). The statistical analysis showed, for all three experiments, that there was not a significant interaction between the working distances tested and the type of acquisition system chosen. Yet, it did indicate that unlike the width measurements, which had an inverse correlation to sensor size, there was a direct correlation between sensor size and the amount of environmental error. This means that as the amount of megapixels increase the accuracy in quantifying length decreases and the accuracy in quantifying the width increases.

#### 4.2.5 Aperture Analysis

Throughout the images taken at each distance, a variety of f-stop values were utilized ranging from f/4.5 to f/20. A factorial design analysis with a 0.05 significance level was conducted to study the effects multiple factors had on the environmental error regarding width calculations. The factors chosen included aperture value, working distance, and crack width. All of the specimens analyzed were imaged with a 24 mm focal length. Table 13 shows the factors and their associated p-values.

Table 13: Factorial Design Results Relating To Aperture

<b>Factor</b>	<b>P-Value</b>
Aperture	0.277
Working Distance	0.000
Crack Width	0.000
Interaction: Aperture & Working Distance	0.043
Interaction: Crack Width & Working Distance	0.000
Interaction: Aperture & Crack Width	0.257

At a 95 percent confidence level, it can be concluded that the working distance, crack width, and their interaction had a significant effect on the environmental error. The test also showed the effect the f-stop value has on the results is dependent on the working distance.

### **4.3 In-Service Crack Results**

The following sections outline the results of the in-service crack experiment. The first section compares the ability of selected image processing techniques to detect the given crack specimens. The following section analyzes their ability to quantify the geometric dimensions of the cracks. The results for all crack specimens, including data and post-processed images, can be seen in Appendix D

#### **4.3.1 Crack Detection**

The first part of the experiment compared the ability of the selected image processing techniques to detect cracks, through the method outline in Section 3.4.3. When analyzing the images taken with the optical camera, the Jahanshahi Adapted Method, the Fujita Adapted Method, and the Combined Adapted Method were all able to successfully segment the cracks. The Lattanzi Adapted Method, however, was not able to distinguish between concrete surface features and the crack. An example of the processed images can be seen in Figure 38.

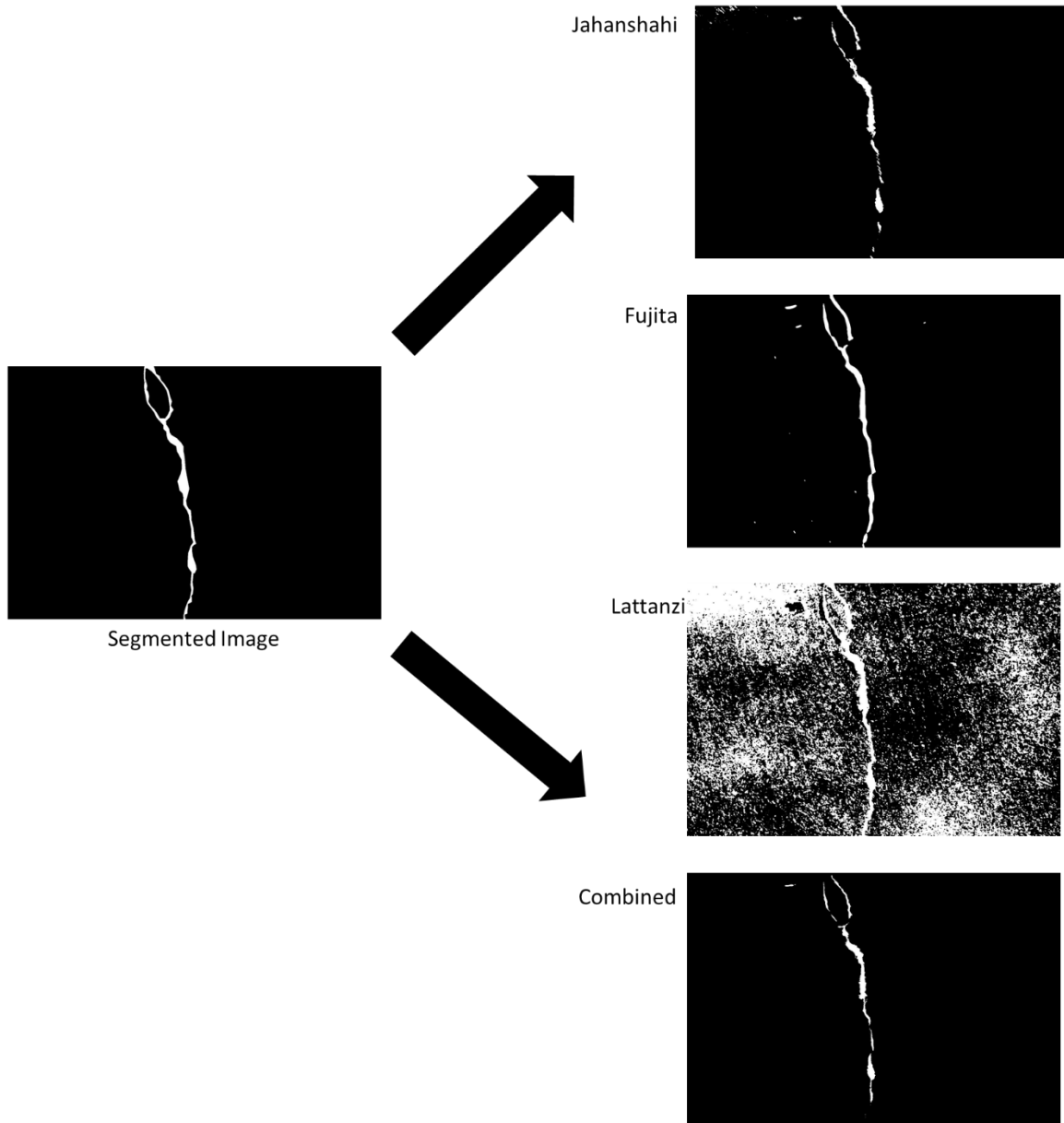


Figure 38: Example Segmentation of In-Service Cracks Imaged with the Optical Camera

For the near infrared camera, all of the algorithms could not successfully segment that cracks, as shown in Figure 39. The Jahanshahi Adapted Method and the Lattanzi Adapted Method could not distinguish the crack from the concrete surface. While, the Fujita Adapted Method and the Combined Method were able to better detect the crack, they both contained noisy pixels produced from the near infrared camera's sensitivity to the aggregates.

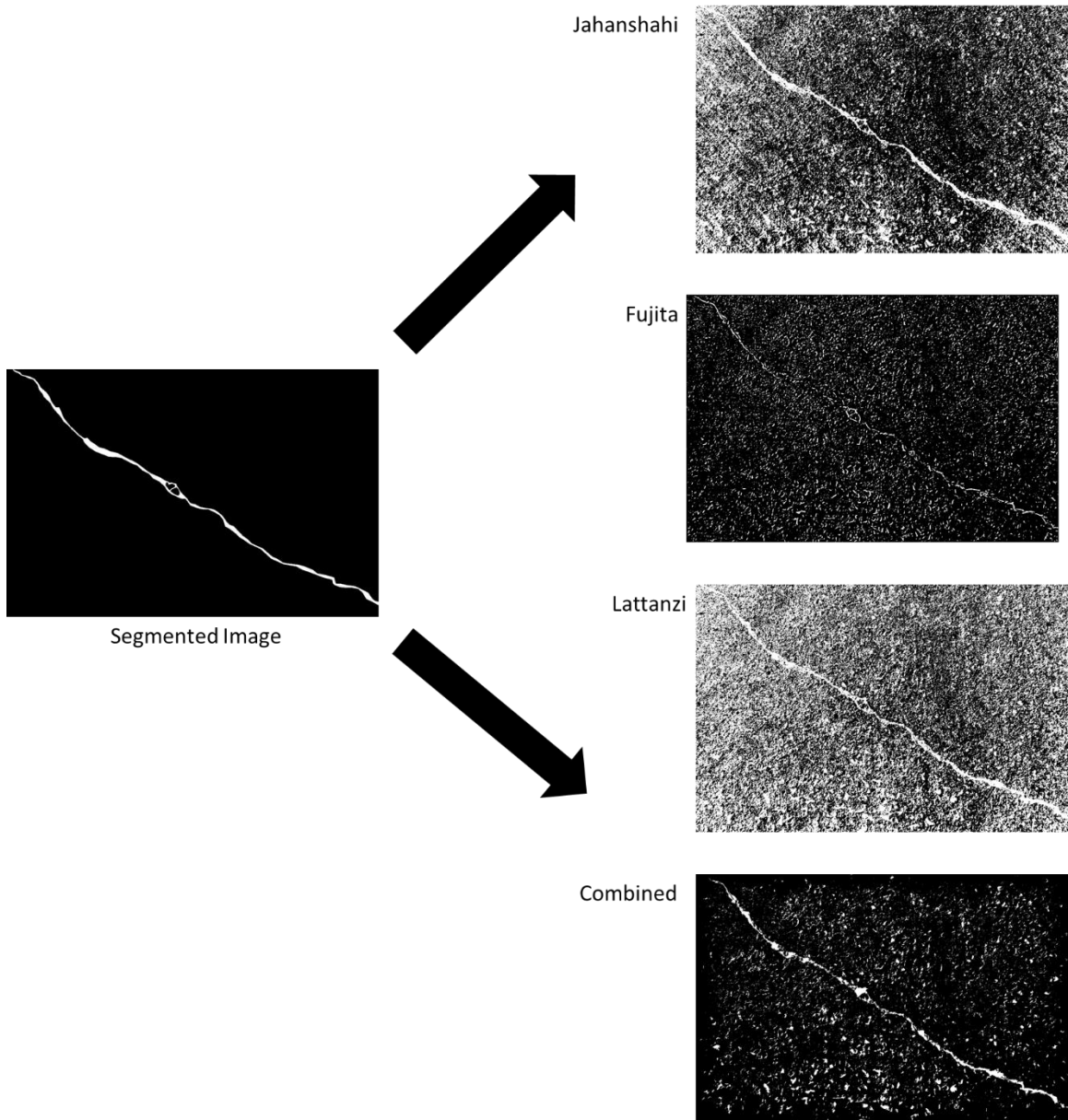


Figure 39: Example Segmentation of In-Service Cracks Imaged with the NIR Camera

After all of the images were processed, the algorithms were compared to one another by quantifying the difference between the manually segmented image and the processed image. As discussed in Section 3.4.3, this was completed by subtracting the processed image from the manually segmented image. If the processed image perfectly segmented the crack, the subtracted

image would appear black. If the algorithm failed to perfectly segment the crack, the difference between the two images would result in residual pixels. An example of the residual pixels, shown in white, can be seen in Figure 40.



Figure 40: Example of Residual Pixels

The amount of residual pixels were greater when an image was captured with the near infrared camera than when it was captured with the optical camera, as can be seen in Table 14. For both acquisition systems, the Lattanzi Adapted Method performed the worst at detecting cracks. When the images were captured using the optical system, the Combined Method performed the best. However, when the images were taken with the near infrared camera the Fujita Adapted Method was the best.

Table 14: Average Residual Pixels from the In-Service Cracks

Camera Type	Jahan	Fujita	Lattanzi	Combined
Optical	7,391	9,230	665,699	4,779
NIR	948,806	117,826	1,093,962	236,050

### 4.3.2 Crack Geometry

None of the cracks that were captured with the near infrared camera were segmented enough to quantify their geometric properties. The optically imaged cracks segmented by the Lattanzi Adapted Method could also not be quantified. Unlike the ideal specimens, the in-service cracks are not straight lines and therefore are subject to the stair-step effect. Therefore, the processed image dimensions were compared to the manually segmented image dimensions. Another issue in accurately comparing the techniques came from the noise pixels and non-continuous crack pixels, as shown in Figure 41.

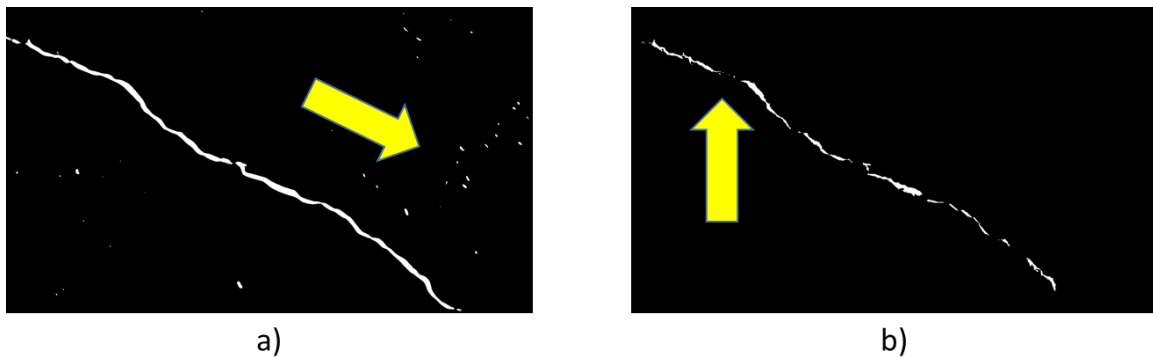


Figure 41: Example of Issues in Segmented Images: a) Noise; b) Non-continuous Pixels

The average errors shown in Table 15 result from the extra noise pixels and the non-continuous crack pixels. Error is defined using equation 4.7.

$$\text{Technique Error} = \frac{(S - P)}{S} \times 100 \quad \text{Equation 4.7}$$

where  $S$  is the amount of dimension pixels found in the manually segmented image and  $P$  is the amount of dimension pixels found in the processed image. For the five specimens analyzed with the optical camera, the Combined Method Produced the best results in quantifying the width and length of a crack.

Table 15: Average Optical Measurement Errors for In-Service Cracks

Dimension	Jahan (%)	Fujita (%)	Lattanzi (%)	Combined (%)
Width	30.22	31.49	x	18.61
Length	34.45	27.99	x	20.46

If the image contains non-continuous pixels, the algorithms underestimated the length and the width of the crack. Morphological operations can be used to bridge the gaps between the non-continuous pixels, thus providing a way to reduce the errors in calculating crack dimensions. If the image contains noisy pixels, the algorithms overestimate the length and the width of the crack. This error can also be reduced by using morphological operations to clean the image from erroneous pixels. However, the type of morphological operation and window size must be carefully chosen so that the shape of the crack does not change.

## 5.0 CONCLUSIONS

---

Bridge inspectors typically use visual inspection methods to monitor the condition of concrete bridge decks. These methods can be both time consuming and subjective. An automated crack detection system would provide a less subjective system. Such a system would need to be efficient, accurate, and practical. This investigation concentrated on evaluating non-contact evaluation techniques used to quantify concrete cracks.

During the simulated crack testing phase it was found that there is an inherent error within an idealized geometric analysis driven by pixel orientation and pixel quantity. The smallest amount of rotation causes an error in calculating geometric dimensions because of the stair-step effect. To eliminate this error, the object's orientation should be zero degrees relative to the x-axis. This is not possible with in-service cracks and it should be noted that all in-service cracks would be subject to errors caused by the stair-step effect. Errors related to pixel quantity occur because binary images only present whole numbers. Therefore, if the amount of pixels needed is a fraction of a number, an error is produced through the rounding process. These errors can be reduced by selecting a sensor size, focal length, and working distance that creates a pixel count close to a whole number.

After the simulated crack phase, tests were performed on ideal laboratory cracks in order to analyze various image processing techniques and different camera parameters. When they analyzed ideal specimens, it was found that there was not enough statistical evidence to conclude that the selected algorithms performed differently. However, the Fujita Adapted Method and the Combined Method

used adaptive thresholding, which proved to be more computationally expensive and time consuming than the methods that used global thresholding.

The experiments showed that the crack width, working distance, and focal length had a significant effect on accurately quantifying geometric properties. Larger crack thicknesses are easier to detect and analyze because they occupy more pixels than smaller cracks. Although, shorter focal lengths have cracks that occupy a small amount of pixels than if they were imaged with a longer focal length, the accuracy of quantifying dimensions is dependent on the working distance. The results also showed that width, not length, is the controlling factor for analyzing and detecting cracks. Lighting conditions and aperture values likewise affect the quality of an image taken. For this experiment it was found that , with a 95 percent confidence level, the effect the f-stop values has on the error, is dependent on the working distance being used. Although the experiments proved that there is an inherent error even in ideal cases, this error can be reduced by selecting the optimum sensor size, focal length, and working distance. The regression equation can eventually provide a starting point to selecting the optimum values of these factors to reduce the inherent error.

When comparing image acquisition systems it was found that the effect the amount of megapixels has on accurately detecting crack dimensions is dependent on the working distance. When quantifying crack width the experiments showed that a decrease in the sensor size led to an increase in error, but when quantifying crack length an increase in sensor size increased the error. There was not enough evidence to conclude that a CCD camera produced a different amount of error compared to the DSLR camera.

It also could not be concluded that the near infrared camera produced a different amount of error compared to the optical camera when imaging under ideal conditions. However, during the in-service crack experiment the near infrared camera was more sensitive to the concrete surface and the aggregate; therefore, the near infrared camera could not successfully segment the cracks. The Fujita Adapted Method was able to most successfully segment the cracks when the near infrared camera was used. The Combined Method was the best at both segmenting and quantifying crack dimensions when the optical camera imaged the specimens. The errors calculated by this experiment could be reduced by changing the sensor size, focal length, or working distance. The digital image processing techniques could also be improved upon by including morphological operations that bridge non-continuous pixels or operations that eliminate noisy pixels.

When inspecting concrete cracks on a bridge deck, the goals of the project need to be well defined. This includes the desired crack size to be detected, the amount of acceptable error, and the area of the bridge that needs to be captured. Then the proper camera parameters, such as the focal length and working distance can be determined. These variables should be chosen to minimize the amount of inherent error in the processing techniques used to quantify the crack dimensions.

## 6.0 FUTURE WORK

---

This investigation focused on testing different acquisition systems and image processing methods that could be used as another means of conducting non-contact evaluation of concrete bridge decks. Only a select number of camera parameters, image acquisition systems, and image processing techniques were analyzed. Further study is needed in the following areas to completely assess the optimal parameters needed to effectively analyze concrete bridge deck defects.

- The camera parameters in this study were limited to two sensor sizes, three focal lengths, and six working distances. Adding more variety to these factors, i.e. more focal lengths, would increase the understanding of camera parameters and ultimately lead to a more precise regression equation. The regression equation could then be used as a guideline to setting up the optimum environment for imaging concrete bridge defects.
- This study only focused on the use of four image processing techniques that have been developed. Other techniques that are more robust in the handling of environmental factors, such as shadows and debris, need to be researched and developed.
- Each of the image processing techniques used had parameters that needed to be manually inputted in order to obtain the best result. These parameters varied depending on crack size, working distance, and the camera system. There needs to be a conclusive study on what parameters are optimal for various crack dimensions and environmental conditions.

- The current study focused on taking images while being perpendicular to the crack. This eliminated any error due to angles of the camera. More research should be done on the effects the camera has on the accuracy in detecting a crack's geometry.
- The current study also only focused on 2D images. By extending the study to focus on 3D images, data can be detected on crack depth. This could help inspectors recognize if the crack depth extends to the location of the reinforcement thus leading to a higher chance of steel corrosion.
- Mounting a camera on top of a moving vehicle would allow images to be taken at highway speeds thus eliminating the need to close traffic lanes. However, this concept presents numerous variables that need to be analyzed. These variables include the distance and angle in which the camera should be mounted, the effect vibration has on the quality of images, the quality of images captured at different speeds, and the ability of image processing techniques to detect cracks under less than ideal conditions. It can be expected that when imaging at highway speeds the bridge deck will have debris that could hide the cracks or hinder the ability of the cracks to be detected. There is also inconsistency of weather conditions, such as snow or rain, and the interference of shadows.

- In this investigation, images were taken in the field and then post-processed within MATLAB at the office. More research should be conducted in evaluating the feasibility of inspectors being able to take an image with their phone, send it to a server, and then immediately see the results on their phone.
- The experiments conducted with the near-infrared camera provided promising results. Although the camera was more sensitive to aggregate at closer distances, it could become a valuable tool when imaging from greater distances, for example on top of a van. More studies should be done on the ability of a near-infrared camera to accurately analyze cracks from greater distances.
- The near-infrared camera also proved throughout the investigation its ability to enhance the contrast of various materials such as steel, aggregates, and concrete. By combining the near-infrared camera with other image acquisition systems, a complete analysis of bridges can be accomplished. This analysis could include a surface investigation for rust stains, cracks, and spalls.
- Combining the near-infrared camera or the optical camera with a thermal camera could also provide interesting results. Combining the two cameras would allow investigators to see both surface and near surface defects. More research should be done to see the capability of this idea, the challenges it presents, and the advantages that could come from combining the technologies.

## REFERENCES

---

- Abdel-qader, I., Abudayyeh, O., and Kelly, M. E. (2003). "Analysis of Edge-Detection Techniques for Crack Identification in Bridges." *Journal of Computing in Civil Engineering*, 17(October), 255–263.
- Acton, S. (2013). *Binary Image Processing*. Personal Collection of Scott Acton, University of Virginia School of Engineering and Applied Sciences Electrical Engineering Department, Charlottesville, VA.
- Alani, A.M., Aboutalebi, M. and Kilic, G. (2013) "Applications of Ground Penetrating Radar (GPR) in Bridge Deck Monitoring and Assessment." *Journal of Applied Geophysics*, 97, 45-54.
- American Society of Civil Engineers. (2013). "2013 Report Card for America's Infrastructure."
- Ammouche, A., Riss, J., Breyse, D., and Marchand, J. (2001). "Image analysis for the automated study of microcracks in concrete." *Cement and Concrete Composites*, 23(2-3), 267–278.
- ASTM. (2007). "ASTM D4788-03: Standard practice for measuring delaminations in concrete decks using infrared thermography." *ASTM International*, West Conshohocken, PA.
- ASTM. (2010). "ASTM C1383-04: Standard test method for measuring the p-wave speed and the thickness of concrete plates using the impact-echo method." *ASTM International*, West Conshohocken, PA.
- ASTM. (2011). "ASTM D6432-11: Standard guide for using the surface ground penetrating radar method for subsurface investigation." *ASTM International*, West Conshohocken, PA.
- Atomic, I., and Agency, E. (2002). *Guidebook on non-destructive testing of concrete structures*.
- AutoCAD (2014). [Computer software]. San Rafael, CA: Autodesk, Inc.
- Bovik, A. (2009). *The Essential Guide to Image Processing*. Elsevier, Boston, MA, 853.
- Bradley, D., and Roth, G. (2007). "Adaptive Thresholding using the Integral Image." *Journal of Graphics, GPU, and Game Tools*, 12(2), 13–21.
- Canny, J. (1986). "A computational approach to edge detection." *IEEE transactions on pattern analysis and machine intelligence*, 8(6), 679–98.
- Carino, N. (2001). "The impact echo method: an overview." *National Institute of Standards and Technology*, 1-18.

- Chase, S. (2013). *Visual Inspection*. Personal Collection of Stephen Chase, University of Virginia School of Engineering and Applied Sciences Civil Engineering Department, Charlottesville, VA.
- Chen, L.-C., Shao, Y.-C., Jan, H.-H., Huang, C.-W., and Tien, Y.-M. (2006). “Measuring System for Cracks in Concrete Using Multitemporal Images.” *Journal of Surveying Engineering*, 132(2), 77–82.
- Chen, S., Rice, C., Boyle, C., and Hauser, E. (2011). “Small-Format Aerial Photography for Highway-Bridge Monitoring.” *Journal of Performance of Constructed Facilities*, 25(2), 105–112.
- Chen, Z., and Hutchinson, T. C. (2010). “Image-Based Framework for Concrete Surface Crack Monitoring and Quantification.” *Advances in Civil Engineering*, 2010, 1–18.
- Clark, M. ., McCann, D. ., and Forde, M. . (2003). “Application of infrared thermography to the non-destructive testing of concrete and masonry bridges.” *NDT & E International*, 36(4), 265–275.
- Daniels, D. J. (2004). *Ground Penetrating Radar*. London: Institution of Electrical Engineers.
- Federal Highway Administration. (2012). *Bridge Inspector’s Reference Manual*. Washington, D.C.
- Fujita, Y., and Hamamoto, Y. (2011). “A robust automatic crack detection method from noisy concrete surfaces.” *Machine Vision and Applications*, 22, 245–254.
- Ganapuram, S., Adams, M., and Patnaik, A. (2012). *Quantification of Cracks in Concrete Bridge Decks in Ohio District 3*.
- Geophysical Survey Systems, Inc. (2006). *GSSI Handbook for RADAR Inspection of Concrete*, Published by Geophysical Survey Systems, Inc. (GSSI), Salem, NH
- Halfawy, M. R., and Hengmeechai, J. (2014). “Efficient Algorithm for Crack Detection in Sewer Images from Closed-Circuit Television Inspections.” *Journal of Infrastructure Systems*, 20(2).
- Hedrick, S. E., Bennett, R. M., Rials, T. G., and Kelley, S. S. (2007). “Correlation of Near-Infrared Spectroscopy Measurements with the Properties of Treated Wood.” *Journal of Materials in Civil Engineering*, 19(4), 279–285.
- Hellier, C. (2013). *Handbook of Nondestructive Evaluation*. McGraw Hill Companies, Inc, New York, New York.
- Higgins, C., and Turan, O. T. (2013). “Imaging Tools for Evaluation of Gusset Plate Connections in Steel Truss Bridges.” *Journal of Bridge Engineering*, 18(5), 380–387.

- Ishikawa, D., Shinzawa, H., Genkawa, T., Kazarian, S. G., and Ozaki, Y. (2014). “Recent progress of near-infrared (NIR) imaging--development of novel instruments and their applicability for practical situations--.” *Analytical sciences : the international journal of the Japan Society for Analytical Chemistry*, 30(1), 143–50.
- Iyer, S., and Sinha, S. K. (2005). “A robust approach for automatic detection and segmentation of cracks in underground pipeline images.” *Image and Vision Computing*, 23(10), 921–933.
- Jahanshahi, M. R., and Masri, S. F. (2012). “Adaptive vision-based crack detection using 3D scene reconstruction for condition assessment of structures.” *Automation in Construction*, Elsevier B.V., 22, 567–576.
- Jahanshahi, M. R., and Masri, S. F. (2013). “A new methodology for non-contact accurate crack width measurement through photogrammetry for automated structural safety evaluation.” *Smart Materials and Structures*, 22(3).
- Jahanshahi, M. R., Masri, S. F., Padgett, C. W., and Sukhatme, G. S. (2011). “An innovative methodology for detection and quantification of cracks through incorporation of depth perception.” *Machine Vision and Applications*, 24(2), 227–241.
- Jiang, R., Jáuregui, D. V., and White, K. R. (2008). “Close-range photogrammetry applications in bridge measurement: Literature review.” *Measurement*, 41(8), 823–834.
- Kass, M., Witkin, A., and Terzopolous, D. (1987). “Snakes: active contour models.” *International Journal of Computer Vision*, 1(4).
- Kosmatka, S., and Wilson, M. (2011). *Design and Control of Concrete Mixtures*. Portland Cement Association, Skokie, Illinois.
- Lattanzi, D., and Miller, G. R. (2014). “Robust Automated Concrete Damage Detection Algorithms for Field Applications.” *Journal of Computing in Civil Engineering*, 28(2), 253–262.
- LDP LLC. (2014). “Camera Conversions.” <<https://www.maxmax.com/>>.
- Lerma, J. L. (2005). “Automatic Plotting of Architectural Facades with Multispectral Images.” *Journal of Surveying Engineering*, 131(3), 73–77.
- Li, B., and Acton, S. T. (2007). “Active contour external force using vector field convolution for image segmentation.” *IEEE transactions on image processing : a publication of the IEEE Signal Processing Society*, 16(8), 2096–106.
- Litwiller, D. (2001). “CCD vs . CMOS : Facts and Fiction.” *Photonics Spectra*, (January).

- Liu, Y.-F., Cho, S., Spencer, B. F., and Fan, J.-S. (2014). "Concrete Crack Assessment Using Digital Image Processing and 3D Scene Reconstruction." *Journal of Computing in Civil Engineering*, 04014124.
- MathWorks. (2015). "k-Means Clustering." <<http://www.mathworks.com/help/stats/k-means-clustering.html>> (Nov. 30, 2015).
- MATLAB and Statistics Toolbox Release 2013b (2013). [Computer software]. Natick, MA: The MathWorks, Inc.
- Minitab 17 Statistical Software (2010). [Computer software]. State College, PA: Minitab, Inc.
- Mukherjee, S., Condron, B., and Acton, S. (2014). "Tubularity Flow Field - A Technique For Automatic Neuron Segmentation." *IEEE transactions on image processing : a publication of the IEEE Signal Processing Society*, 24(1), 374–389.
- Nikon. (2015). "Understanding Maximum Aperture." <<http://www.nikonusa.com/en/Learn-And-Explore/Article/g3cu6o1r/understanding-maximum-aperture.html>> (Jan. 30, 2014).
- Nikon. (2015). "Macro Lenses." <<http://www.nikonusa.com/en/Learn-And-Explore/Article/gnhy8b3m/macro-lenses.html>> (Jan. 30, 2014).
- Oh, J.-K., Jang, G., Oh, S., Lee, J. H., Yi, B.-J., Moon, Y. S., Lee, J. S., and Choi, Y. (2009). "Bridge inspection robot system with machine vision." *Automation in Construction*, Elsevier B.V., 18(7), 929–941.
- Sansalone, M. (1997). "Impact-echo: the complete story." *ACI Structural Journal*, 94(6), 777-786.
- De Schutter, G. (2002). "Advanced monitoring of cracked structures using video microscope and automated image analysis." *NDT & E International*, 35(4), 209–212.
- Sheppard, R. (2010). *Digital Photography Top 100 Simplified Tips & Tricks*. Wiley Publishing Inc, Indianapolis, Indiana.
- Siesler, H. W., Ozaki, Y., Kawata, S., and Heise, H. M. (2002). *Near infrared spectroscopy principles, instruments, applications*. Wiley VCH, Weinham, Germany.
- Sural, S., and Pramanik, S. (2002). "Segmentation and histogram generation using the HSV color space for image retrieval." *Proceedings. International Conference on Image Processing*, IEEE, II-589–II-592.
- Tang, J., Millington, S., Acton, S. T., Crandall, J., and Hurwitz, S. (2006). "Surface extraction and thickness measurement of the articular cartilage from MR images using directional gradient vector flow snakes." *IEEE transactions on bio-medical engineering*, 53(5), 896–907.

- Torok, M. M., Golparvar-Fard, M., and Kochersberger, K. B. (2014). "Image-Based Automated 3D Crack Detection for Post-disaster Building Assessment." *Journal of Computing in Civil Engineering*, 28(5), A4014004.
- Tung, P.-C., Hwang, Y.-R., and Wu, M.-C. (2002). "The development of a mobile manipulator imaging system for bridge crack inspection." *Automation in Construction*, 11(6), 717–729.
- U.S. Department of Transportation, Federal Highway Administration, and Federal Transit Administration. (2013). *2013 Status of the nation's highways, bridges, and transit: conditions and performance*. Washington, DC.
- Vaghefi, K., Ahlborn, T. (Tess) M., Harris, D. K., and Brooks, C. N. (2013). "Combined Imaging Technologies for Concrete Bridge Deck Condition Assessment." *Journal of Performance of Constructed Facilities*, 04014102.
- Valença, J., Gonçalves, L. M. S., and Júlio, E. (2013). "Damage assessment on concrete surfaces using multi-spectral image analysis." *Construction and Building Materials*, 40, 971–981.
- Vegas, I., Broos, K., Nielsen, P., Lambertz, O., and Lisbona, A. (2015). "Upgrading the quality of mixed recycled aggregates from construction and demolition waste by using near-infrared sorting technology." *Construction and Building Materials*, 75, 121–128.
- Virginia Department of Transportation. (2007). *Element Data Collection Manual*. Richmond.
- Virginia Department of Transportation. (2009). "Guide Manual for Causes and Repair of Cracks in Bridge Decks." Richmond.
- Virginia Department of Transportation. (2013). "State of the Structures and Bridges Report." Richmond, VA.
- Washer, G., Fenwick, R., and Nelson, S. (2013). "Guidelines for the Thermographic Inspection of Concrete Bridge Components in Shaded Conditions." *Transportation Research Record: Journal of the Transportation Research Board*.
- Wellner, P. D. (1993). *Adaptive Thresholding for the DigitalDesk*. Cambridge.
- Wu, L., Mokhtari, S., Nazef, A., Nam, B., and Yun, H. (2014). "Improvement of Crack-Detection Accuracy Using a Novel Crack Defragmentation Technique in Image-Based Road Assessment." *Journal of Computing in Civil Engineering*, (Level 1).
- Yamaguchi, T., and Hashimoto, S. (2009a). "Fast crack detection method for large-size concrete surface images using percolation-based image processing." *Machine Vision and Applications*, 21(5), 797–809.
- Yamaguchi, T., and Hashimoto, S. (2009b). "Practical image measurement of crack width for real concrete structure." *Electronics and Communications in Japan*, 92(10), 1–12.

- Yu, S.-N., Jang, J.-H., and Han, C.-S. (2007). "Auto inspection system using a mobile robot for detecting concrete cracks in a tunnel." *Automation in Construction*, 16(3), 255–261.
- Zhu, Z., German, S., and Brilakis, I. (2011). "Visual retrieval of concrete crack properties for automated post-earthquake structural safety evaluation." *Automation in Construction*, Elsevier B.V., 20(7), 874–883.

**APPENDIX A: EXPERIMENTAL SET-UP**

Table 16: Pixel Requirements for Nikon D610 with 60 mm Focal Length

<b>Nikon D610</b>						
	<b>3 ft</b>	<b>4 ft</b>	<b>5 ft</b>	<b>6 ft</b>	<b>7 ft</b>	<b>8 ft</b>
<b>Crack Width</b>						
<b>0.125 in</b>	35.01	26.26	21.01	17.51	15.01	13.13
<b>0.060 in</b>	16.81	12.61	10.08	8.40	7.20	6.30
<b>0.020 in</b>	5.60	4.20	3.36	2.80	2.40	2.10
<b>Crack Length</b>						
<b>4 in</b>	1120.45	840.34	672.27	560.22	480.19	420.17
<b>6 in</b>	1680.67	1260.50	1008.40	840.34	720.29	630.25

Table 17: Pixel Requirements for Nikon D610 with 85 mm Focal Length

<b>Nikon D610</b>						
	<b>3 ft</b>	<b>4 ft</b>	<b>5 ft</b>	<b>6 ft</b>	<b>7 ft</b>	<b>8 ft</b>
<b>Crack Width</b>						
<b>0.125 in</b>	49.60	37.20	29.76	24.80	21.26	18.60
<b>0.060 in</b>	23.81	17.86	14.29	11.90	10.20	8.93
<b>0.020 in</b>	7.94	5.95	4.76	3.97	3.40	2.98
<b>Crack Length</b>						
<b>4 in</b>	1587.30	1190.48	952.38	793.65	680.27	595.24
<b>6 in</b>	2380.95	1785.71	1428.57	1190.48	1020.41	892.86

Table 18: Pixel Requirements for Canon 7D with 24 mm Focal Length

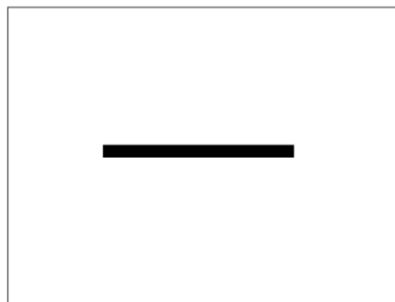
<b>Canon 7D</b>						
	<b>3 ft</b>	<b>4 ft</b>	<b>5 ft</b>	<b>6 ft</b>	<b>7 ft</b>	<b>8 ft</b>
<b>Crack Width</b>						
<b>0.25 in</b>	38.85	29.14	23.31	19.43	16.65	14.57
<b>Crack Length</b>						
<b>4 in</b>	621.60	466.20	372.96	310.80	266.40	233.10

Table 19: Pixel Requirements for CCD and DSLR with 35 mm Focal Length

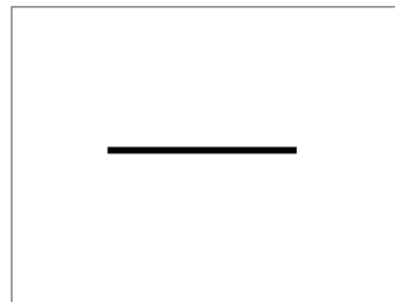
CCD				DSLR		
	1.5 ft	5 ft	8.5 ft	1.5 ft	5 ft	8.5 ft
<b>Crack Width</b>						
<b>0.125 in</b>	70.45	21.14	12.43	40.85	12.25	7.21
<b>Crack Length</b>						
<b>4 in</b>	2254.43	676.33	397.84	1307.19	392.16	230.68

Table 20: Pixel Requirements for NIR Camera with 24 mm Focal Length

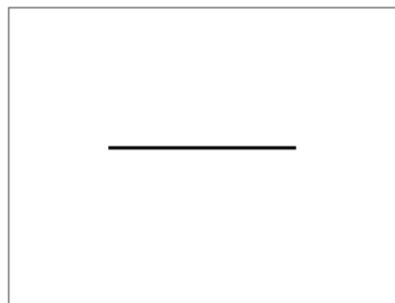
Nikon D3200						
	3 ft	4 ft	5 ft	6 ft	7 ft	8 ft
<b>Crack Width</b>						
<b>0.125 in</b>	21.70	16.28	13.02	10.85	9.30	8.14
<b>Crack Length</b>						
<b>6 in</b>	1041.67	781.25	625	520.83	446.43	390.63



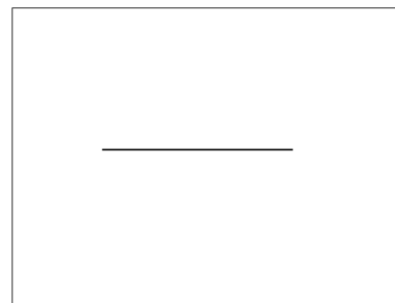
4 in by 0.25 in



4 in by 0.125 in



4 in by 0.06 in



4 in by 0.02 in

Figure 42: Ideal Laboratory Cracks

Table 21: Light Intensity Values

<b>Location</b>	<b>Light Intensity (Iz)</b>
At Ideal Crack	104
3 feet	228
4 feet	490
5 feet	630
6 feet	670
7 feet	690
8 feet	680

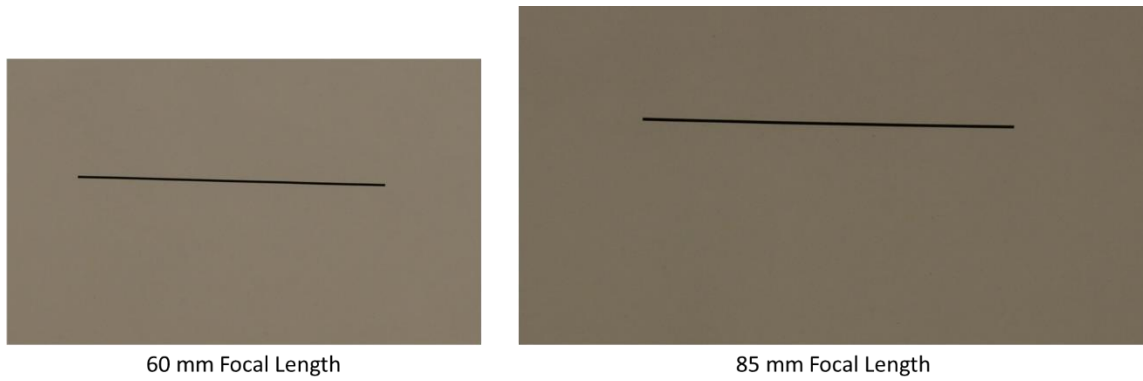


Figure 43: 4 in by 0.02 in Crack Imaged at 4 feet with a 60 mm and 85 mm Focal Length

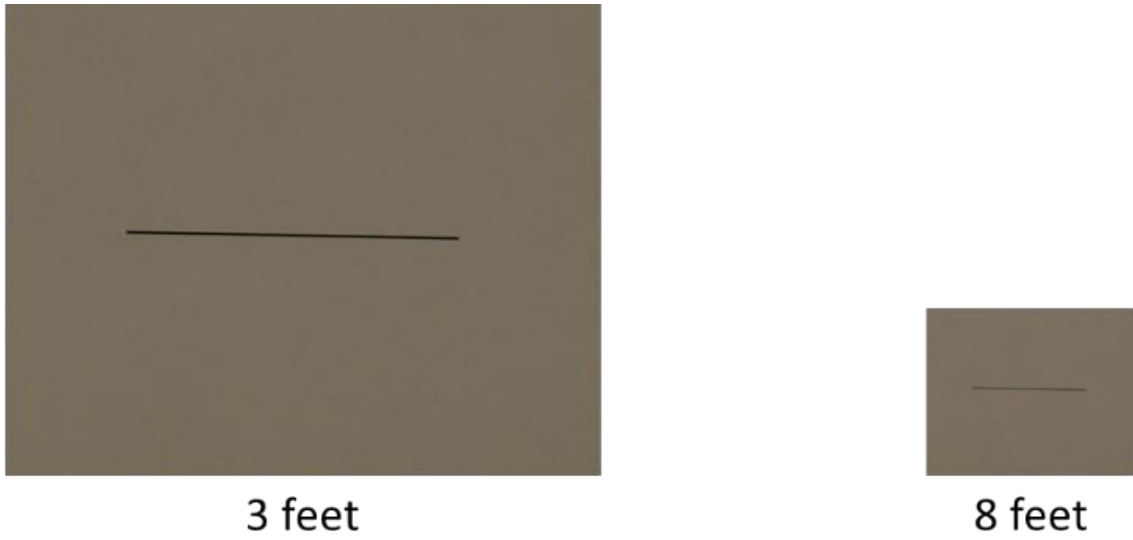


Figure 44: 4 in by 0.02 in Crack Imaged with a 24 mm at 3 feet and 8 feet

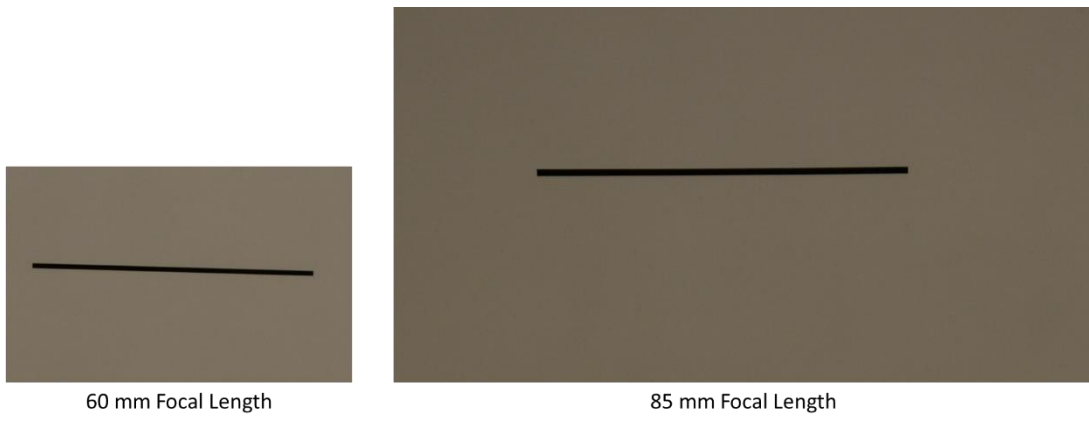


Figure 45: 4 in by 0.06 in Crack Imaged at 4 feet with a 60 mm and 85 mm Focal Length

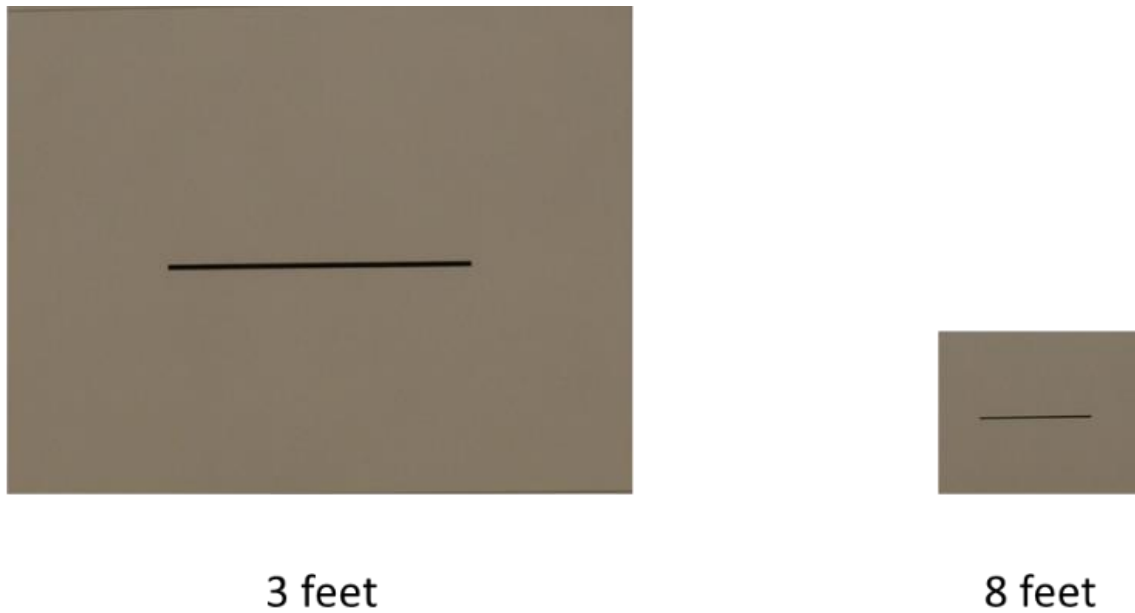


Figure 46: 4 in by 0.02 in Crack Imaged with a 24 mm at 3 feet and 8 feet

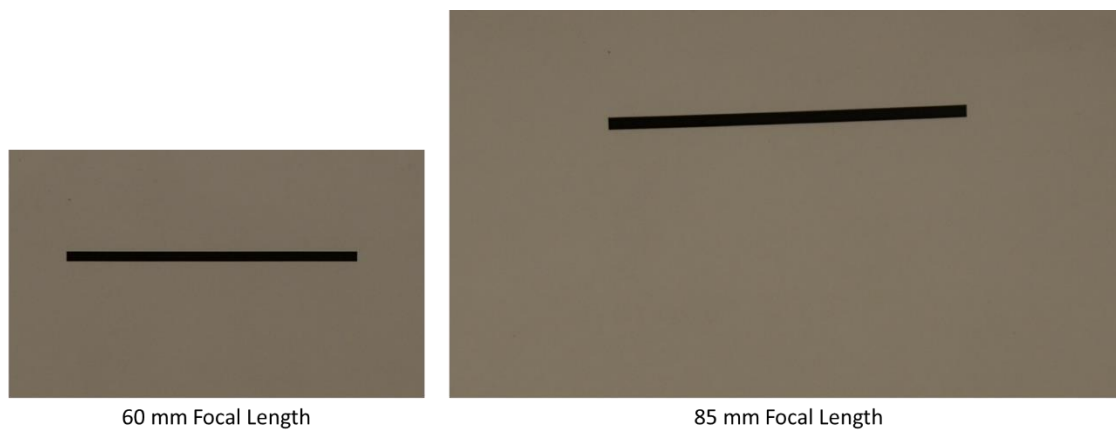


Figure 47: 4 in by 0.125 in Crack Imaged at 4 feet with a 60 mm and 85 mm Focal Length

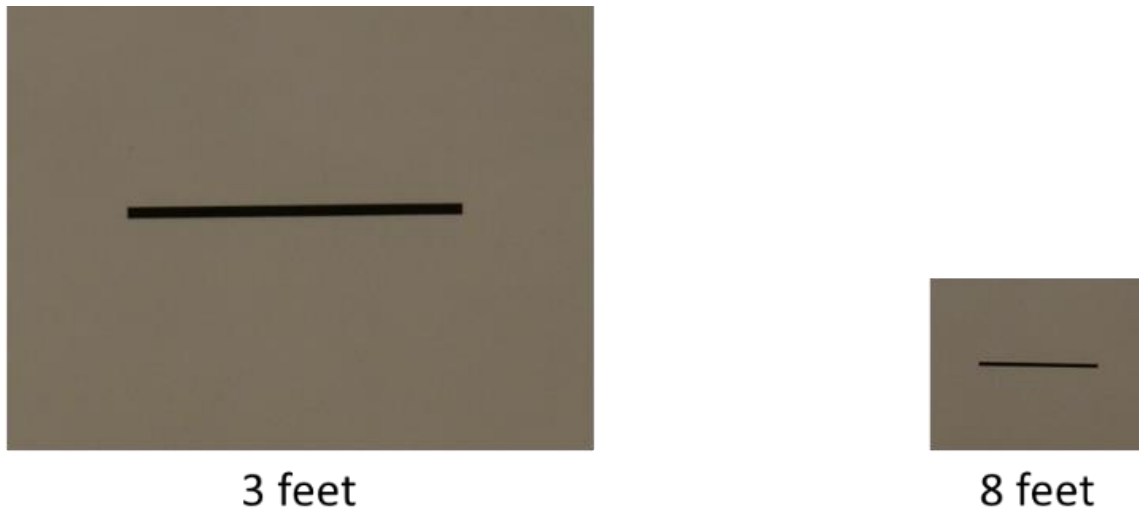


Figure 48: 4 in by 0.125 in Crack Imaged with a 24 mm at 3 feet and 8 feet

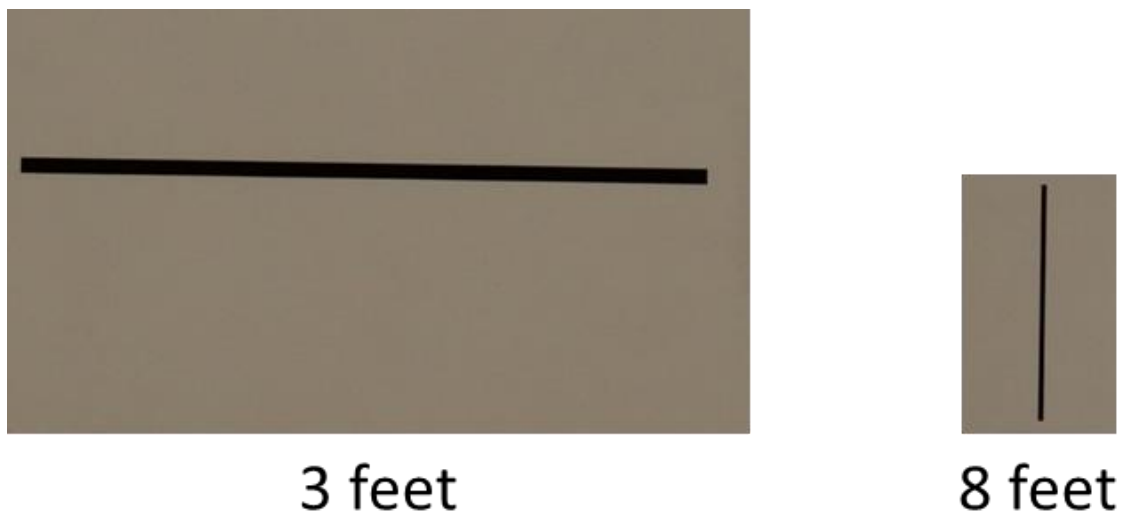


Figure 49: 6 in with a Width of 0.125 in Imaged at 3 feet and 8 feet

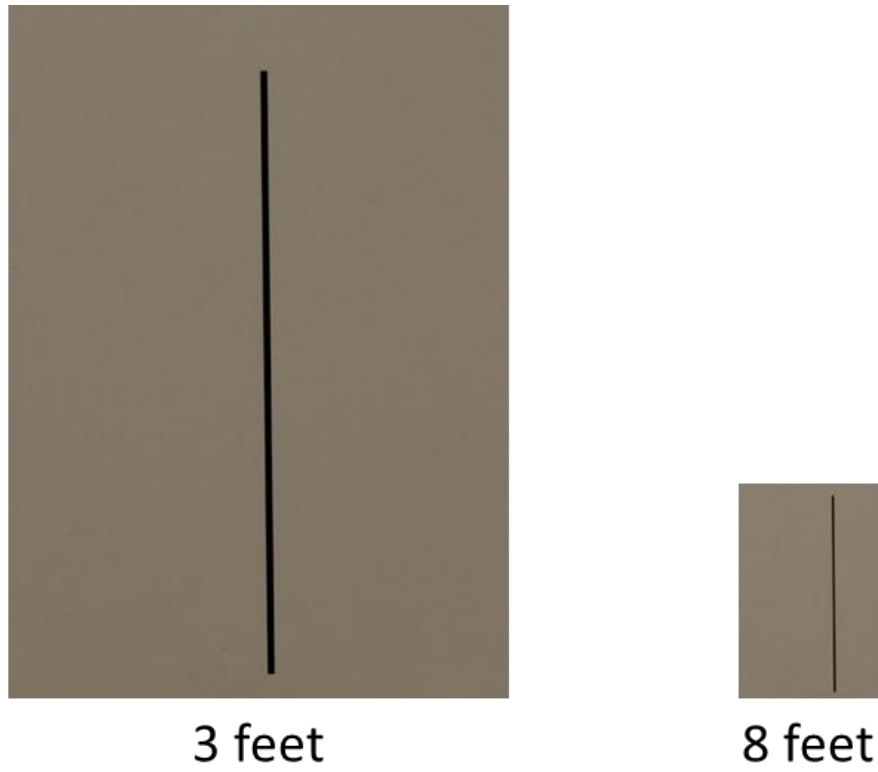


Figure 50: 6 in with a Width of 0.06 in Imaged at 3 feet and 8 feet

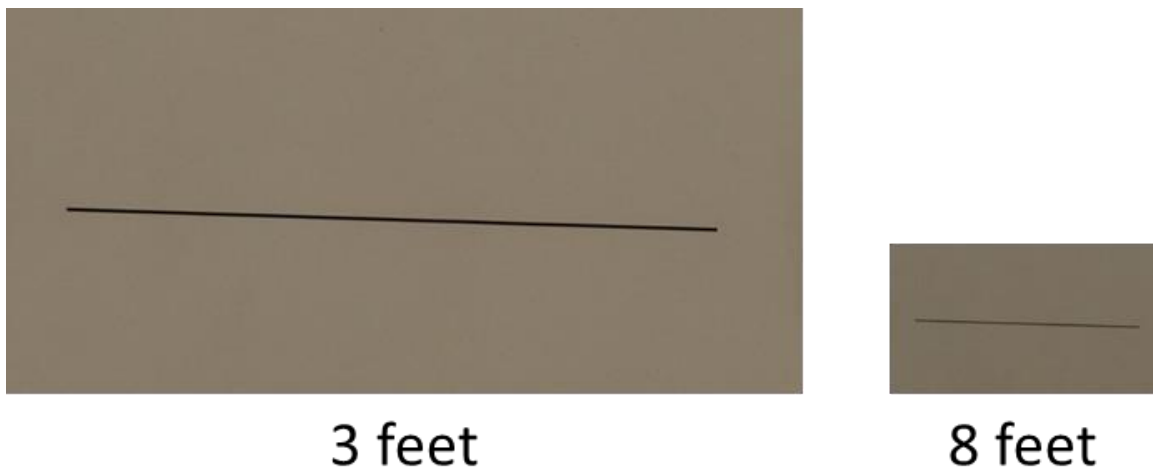
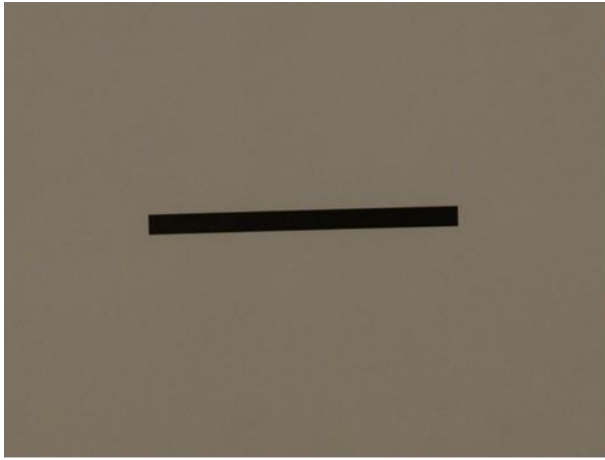


Figure 51: 6 in with a Width of 0.02 in Imaged at 3 feet and 8 feet

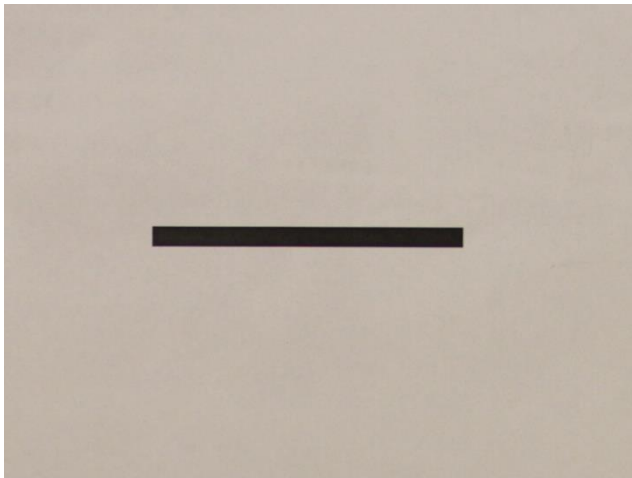


3 feet

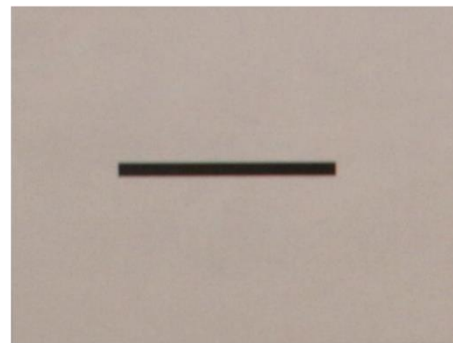


8 feet

Figure 52: Imaged with 24.3 Megapixels at 3 feet and 8 feet

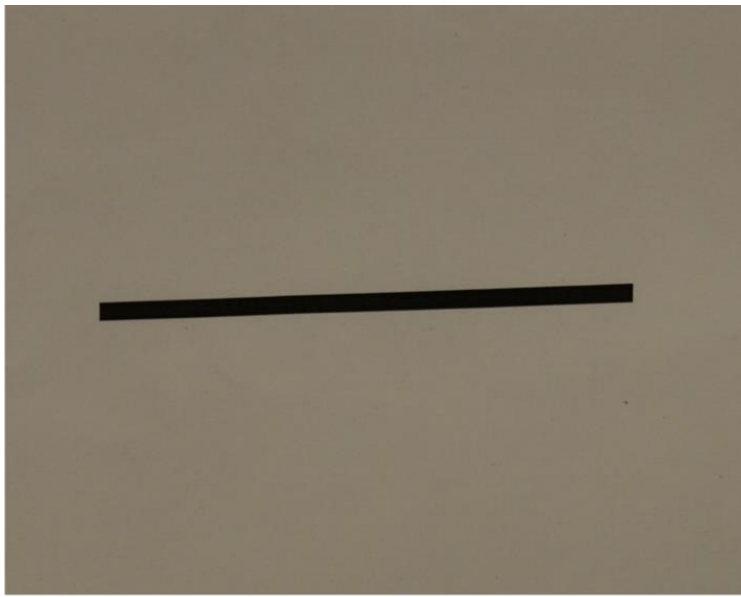


3 feet

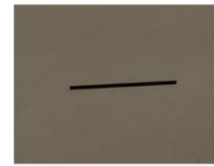


8 feet

Figure 53: Imaged with 18 Megapixels at 3 feet and 8 feet



1.5 feet

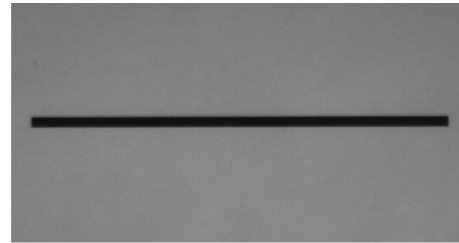


8.5 feet

Figure 54: DSLR Images at 1.5 feet and 8.5 feet



1.5 feet



8.5 feet

Figure 55: CCD Images at 1.5 feet and 8.5 feet



3 feet

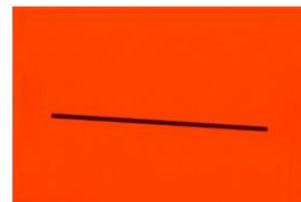


8 feet

Figure 56: Optical Images at 3 feet and 8 feet



3 feet



8 feet

Figure 57: NIR Images at 3 feet and 8 feet



Optical 1



Optical 2



Optical 3



Optical 4



Optical 5

Figure 58: In-Service Cracks Optically Imaged



NIR 1



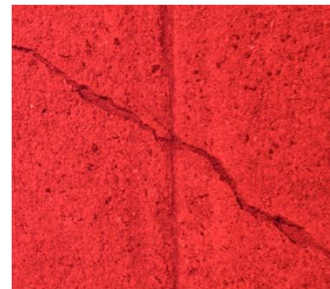
NIR 2



NIR 3



NIR 4



NIR 5

Figure 59: In-Service Cracks NIR Imaged

Table 22: In-Service Field Measurements

Image Name	Type of Camera	Length Measured (in)	Width Measured (in)
NIR_1	NIR	13	0.50
NIR_2	NIR	6	0.50
NIR_3	NIR	13	0.50
NIR_4	NIR	14	0.50
NIR_5	NIR	7	0.50
Op_1	Optical	8	0.50
Op_2	Optical	8	0.80
Op_3	Optical	3	0.20
Op_4	Optical	6	0.30
Op_5	Optical	8	0.30

## APPENDIX B: SIMULATED CRACKS

Table 23: Rotation Errors for 28 by 448 Pixel Crack

Angle:	Width	Length	W-Error	L-Error
0	28	448	0	0
0.02	29	448	3.57	0.00
0.04	29	448	3.57	0.00
0.05	29	448	3.57	0.00
0.1	29	448	3.57	0.00
0.2	30	448	7.14	0.00
0.3	31	448	10.71	0.00
0.4	31	448	10.71	0.00
0.5	32	449	14.29	0.22
0.6	33	448	17.86	0.00
0.7	34	448	21.43	0.00
0.8	33	448	17.86	0.00
0.9	35	448	25.00	0.00
1	36	449	28.57	0.22

Table 24: Rotation Errors for a 11 by 169 Pixel Crack

Angle	Width	Length	W-Error	L-Error
0	11	169	0	0
0.02	11	169	0	0
0.04	11	169	0	0
0.05	11	169	0	0
0.1	11	169	0	0
0.2	12	169	9.09	0
0.3	12	169	9.09	0
0.4	12	169	9.09	0
0.5	12	169	9.09	0
0.6	13	169	18.18	0
0.7	13	169	18.18	0
0.8	13	169	18.18	0
0.9	14	169	27.27	0
1	14	169	27.27	0

Table 25: Rotation Errors for a 5 by 169 Pixel Crack

Angle	Width	Length	W-Error	L-Error
0	5	169	0	0
0.02	6	169	20	0
0.04	6	169	20	0
0.05	6	169	20	0
0.1	6	169	20	0
0.2	6	169	20	0
0.3	6	169	20	0
0.4	7	169	40	0
0.5	7	169	40	0
0.6	7	169	40	0
0.7	7	169	40	0
0.8	8	169	60	0
0.9	8	169	60	0
1	8	169	60	0

Table 26: Pixel Width Errors for the Nikon D610 and a 60 mm Focal Length

<b>Pixel Errors</b>						
<b>Distance</b>	<b>3 ft.</b>	<b>4 ft.</b>	<b>5 ft.</b>	<b>6 ft.</b>	<b>7 ft.</b>	<b>8 ft.</b>
	<b>0.125 in.</b>					
<b>No. of Pixels</b>	35.01	26.26	21.01	17.51	15.01	13.13
<b>Rounded Pixels</b>	35	26	21	18	15	13
<b>% Error</b>	0.04	0.99	0.04	2.82	.04	0.99
	<b>0.06 in.</b>					
<b>No. of Pixels</b>	16.81	12.61	10.08	8.40	7.20	6.30
<b>Rounded Pixels</b>	17	13	10	8	7	6
<b>% Error</b>	1.15	3.13	0.83	4.80	2.82	4.80
	<b>0.02 in.</b>					
<b>No. of Pixels</b>	5.60	4.20	3.36	2.80	2.40	2.10
<b>Rounded Pixels</b>	6	4	3	3	2	2
<b>% Error</b>	7.10	4.80	10.75	7.10	16.70	4.80

Table 27: Pixel Width Errors for the Nikon D610 and an 85 mm. Focal Length

<b>Pixel Errors</b>						
<b>Distance</b>	<b>3 ft.</b>	<b>4 ft.</b>	<b>5 ft.</b>	<b>6 ft.</b>	<b>7 ft.</b>	<b>8 ft.</b>
	<b>0.125 in.</b>					
<b>No. of Pixels</b>	49.60	37.20	29.76	24.80	21.26	18.60
<b>Rounded Pixels</b>	50	37	30	25	21	19
<b>% Error</b>	0.80	0.54	0.80	0.80	1.22	2.14
	<b>0.06 in.</b>					
<b>No. of Pixels</b>	23.81	17.86	14.29	11.90	10.20	8.93
<b>Rounded Pixels</b>	24	18	14	12	10	9
<b>% Error</b>	0.80	0.80	2.00	0.80	2.00	0.80
	<b>0.02 in.</b>					
<b>No. of Pixels</b>	7.94	5.95	4.76	3.97	3.40	2.98
<b>Rounded Pixels</b>	8	6	5	4	3	3
<b>% Error</b>	0.80	0.80	5.00	0.80	11.80	0.80

Table 28: Pixel Width Errors for the Canon 7D and a 24 mm. Focal Length

<b>Pixel Errors</b>						
<b>Distance</b>	<b>3 ft.</b>	<b>4 ft.</b>	<b>5 ft.</b>	<b>6 ft.</b>	<b>7 ft.</b>	<b>8 ft.</b>
	<b>0.25 in.</b>					
<b>No. of Pixels</b>	38.85	29.14	23.31	18.43	16.65	14.57
<b>Rounded Pixels</b>	39	29	23	19	17	15
<b>% Error</b>	0.37	0.47	1.33	2.19	2.10	2.96

Table 29: Pixel Width Errors for the CCD and DSLR camera with a 35 mm. Focal Length

<b>Pixel Errors</b>			
<b>Distance</b>	<b>1.5 ft.</b>	<b>5 ft.</b>	<b>8.5 ft.</b>
	<b>CCD</b>		
<b>No. of Pixels</b>	70.45	21.14	12.43
<b>Rounded Pixels</b>	70	21	12
<b>% Error</b>	0.64	0.64	3.48
	<b>DSLR</b>		
<b>No. of Pixels</b>	40.85	12.25	7.21
<b>Rounded Pixels</b>	41	12	7
<b>% Error</b>	0.37	2.08	2.90

Table 30: Pixel Width Errors for the Nikon D3200 and a 24 mm. Focal Length

<b>Pixel Errors</b>						
<b>Distance</b>	<b>3 ft.</b>	<b>4 ft.</b>	<b>5 ft.</b>	<b>6 ft.</b>	<b>7 ft.</b>	<b>8 ft.</b>
	<b>0.125 in.</b>					
<b>No. of Pixels</b>	21.70	16.28	13.02	10.85	9.30	8.14
<b>Rounded Pixels</b>	22	16	13	11	9	8
<b>% Error</b>	1.38	1.70	0.16	1.38	3.23	1.70

## APPENDIX C: IDEAL LABORATORY CRACK

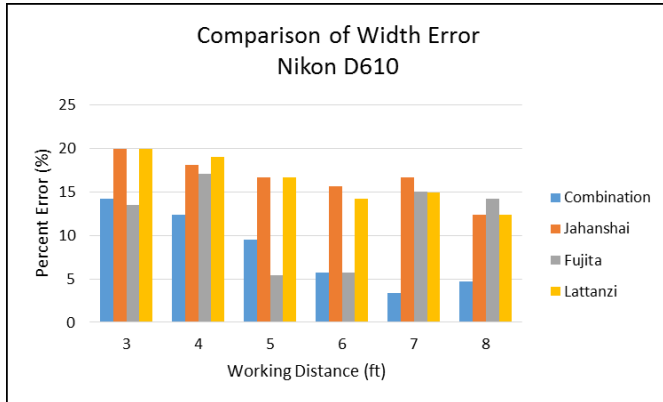


Figure 60: Image Processing Errors for a 0.25 in Crack Using a 24 mm Focal Length

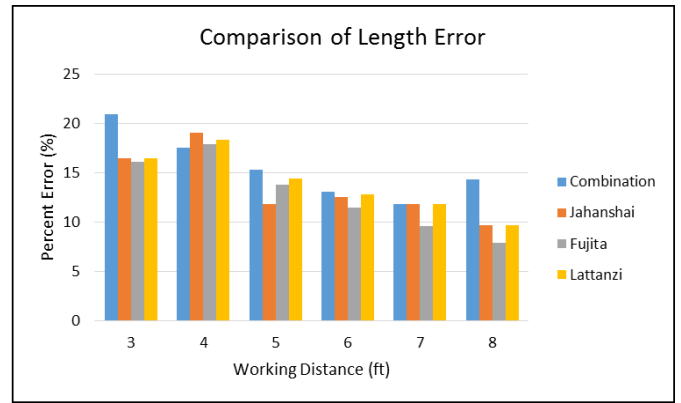


Figure 61: Image Processing Errors for a 0.125 in Crack Using a 24 mm Focal Length



Figure 62: Image Processing Errors for a 0.125 in Crack Using a 60 mm Focal Length



Figure 63: Image Processing Errors for a 0.125 in Crack Using an 85 mm Focal Length

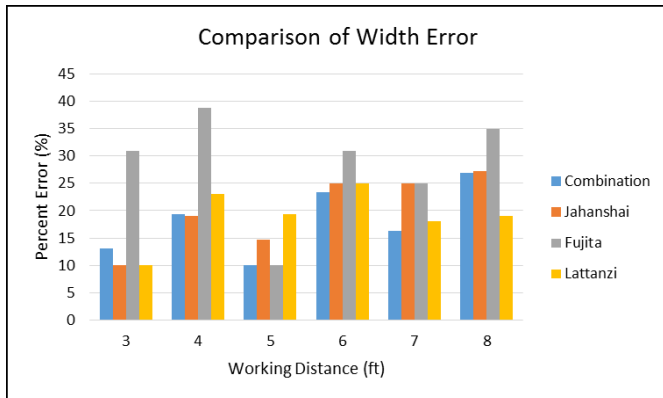


Figure 64: Image Processing Errors for a 0.06 in Crack Using a 24 mm Focal Length

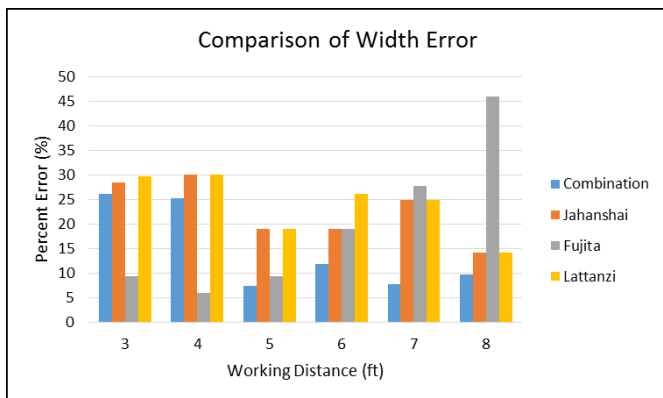


Figure 65: Image Processing Errors for a 0.06 in Crack Using a 60 mm Focal Length



Figure 66: Image Processing Errors for a 0.06 in Crack Using an 85 mm Focal Length



Figure 67: Image Processing Errors for a 0.02 in Crack Using a 24 mm Focal Length



Figure 68: Image Processing Errors for a 0.02 in Crack Using a 60 mm Focal Length

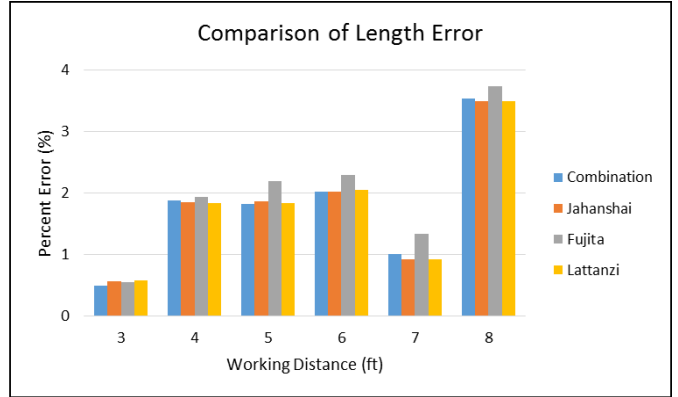


Figure 69: Image Processing Errors for a 0.02 in Crack Using an 85 mm Focal Length



Figure 70: Image Processing Errors for a 6 in by 0.125 in Crack Using a 24 mm Focal Length

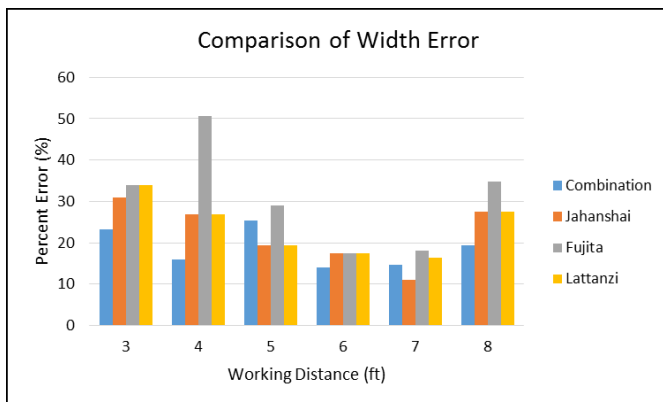


Figure 71: Image Processing Errors for a 6 in by 0.06 in Crack Using a 24 mm Focal Length



Figure 72: Image Processing Errors for a 6 in by 0.02 in Crack Using a 24 mm Focal Length



Figure 73: Image Processing Errors for a 4 in by 0.25 in Crack Using a 24 mm Focal Length and the Canon 7D



Figure 74: Image Processing Errors for a 4 in by 0.125 in Crack Using a 35 mm Focal Length and the CCD Camera

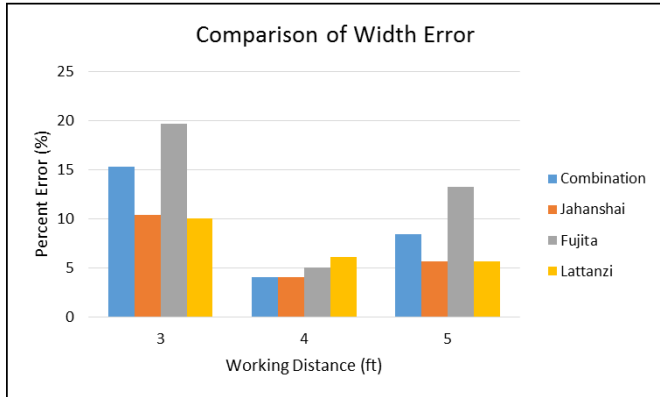


Figure 75: Image Processing Errors for a 4 in by 0.125 in Crack Using a 35 mm Focal Length and the DSLR Camera

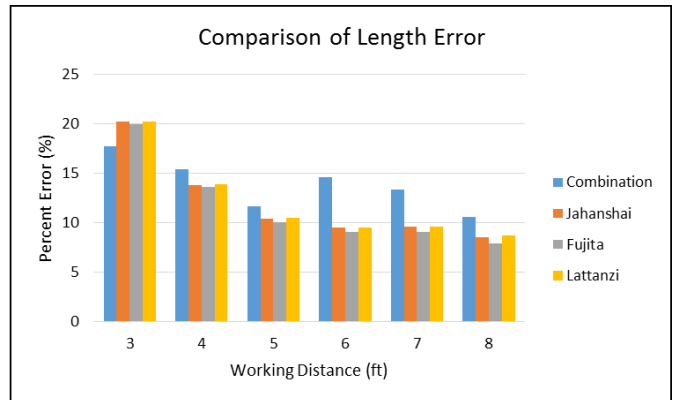
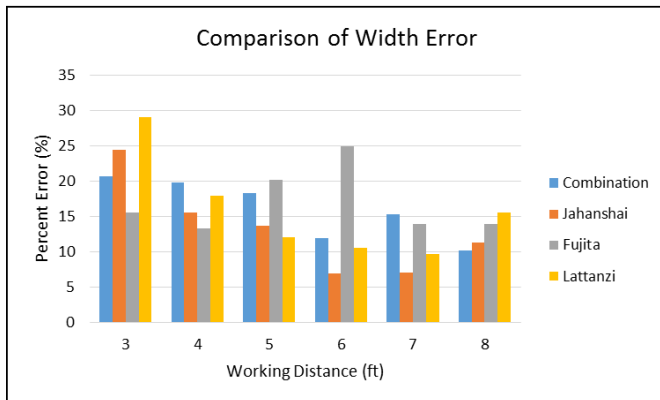


Figure 76: Image Processing Errors for a 6 in by 0.125 in Crack Using a 24 mm Focal Length and the NIR Camera

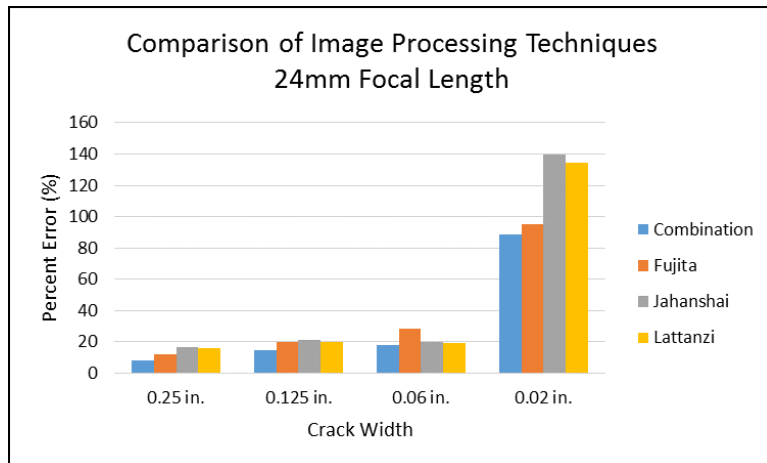


Figure 77: Comparison of 24 mm Focal Length

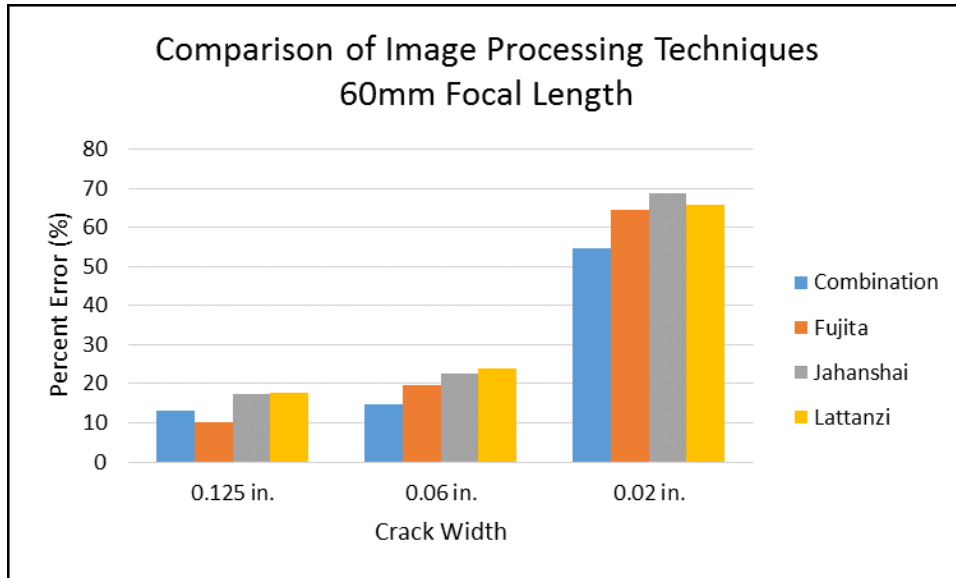


Figure 78: Comparison of 60 mm Focal Length

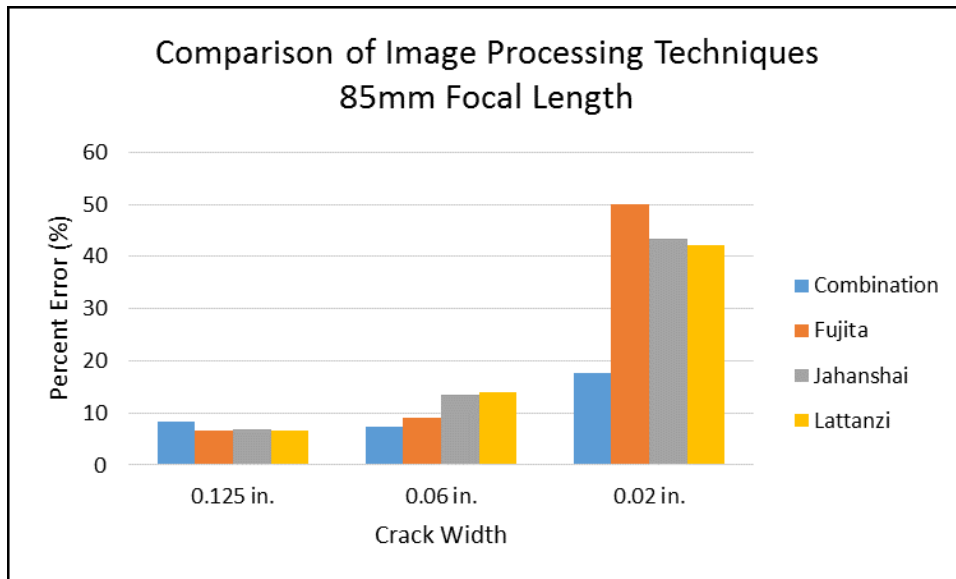


Figure 79: Comparison of 85 mm Focal Length

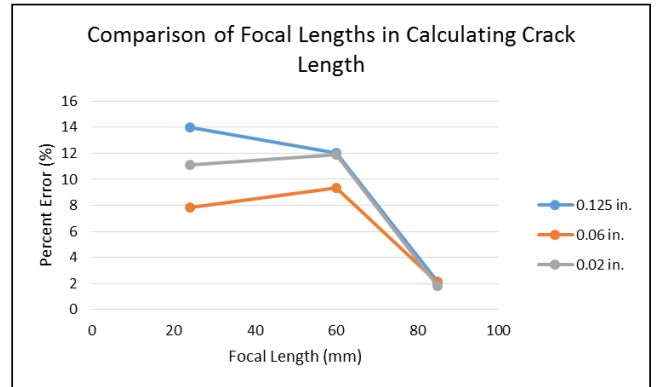
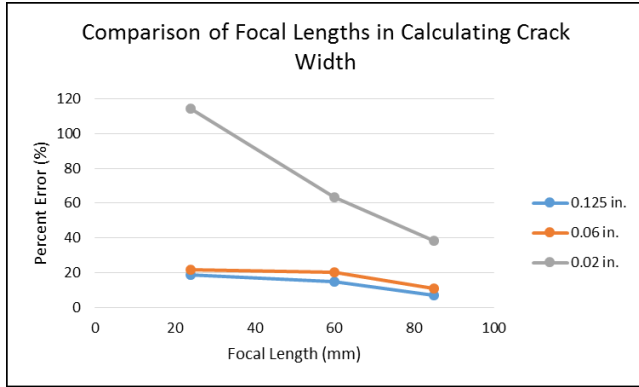


Figure 80: Comparison of Focal Lengths

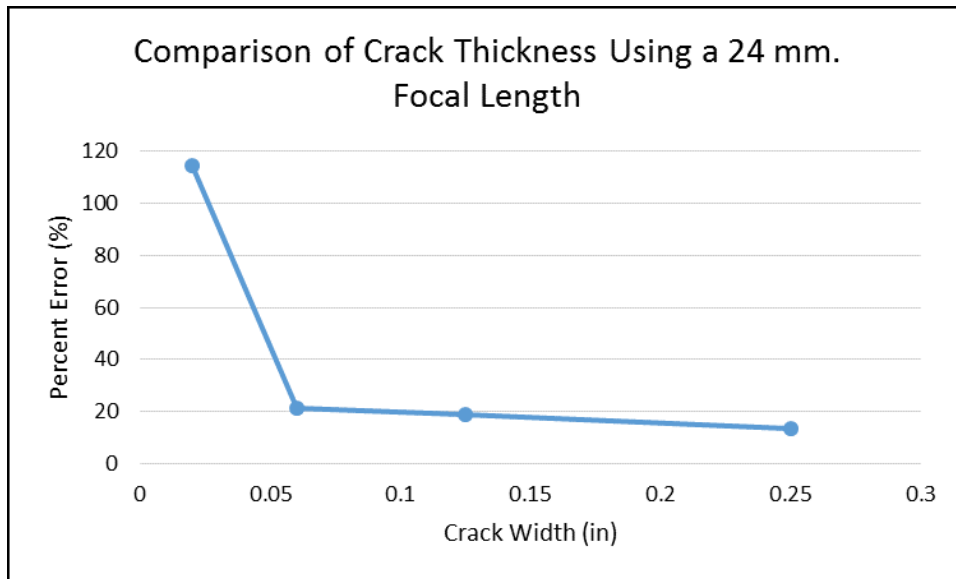


Figure 81: Comparison of Crack Thickness

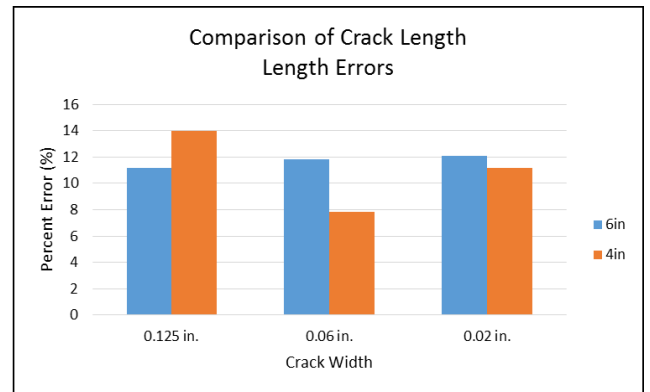
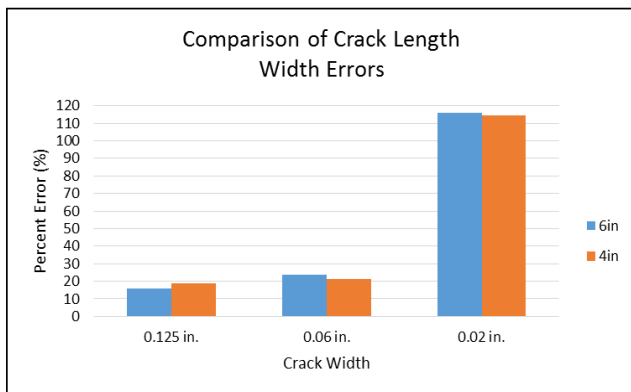


Figure 82: Comparison of Crack Length

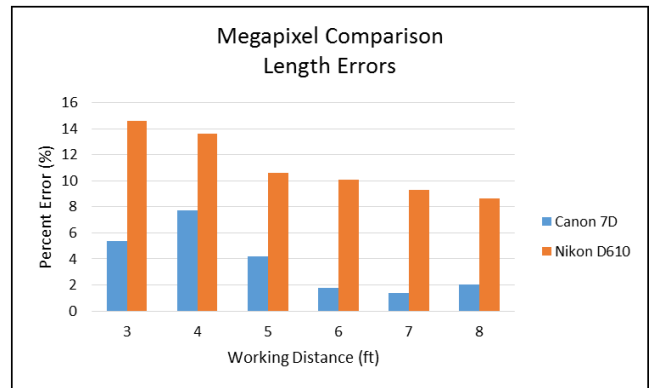
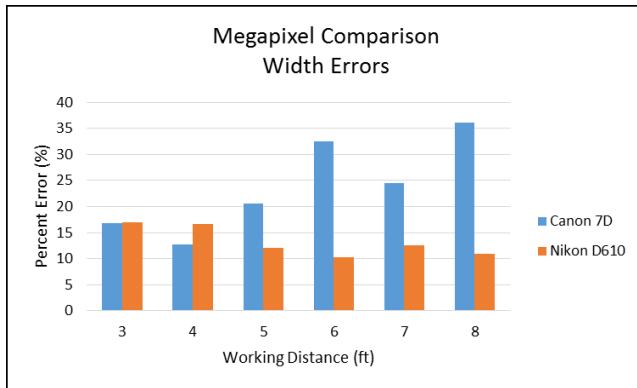


Figure 83: Comparison of Megapixels

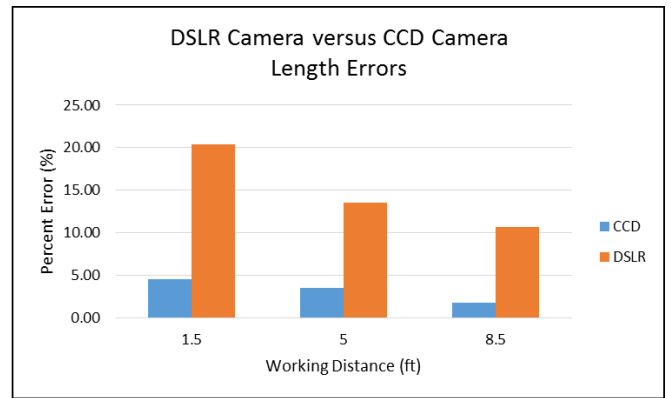
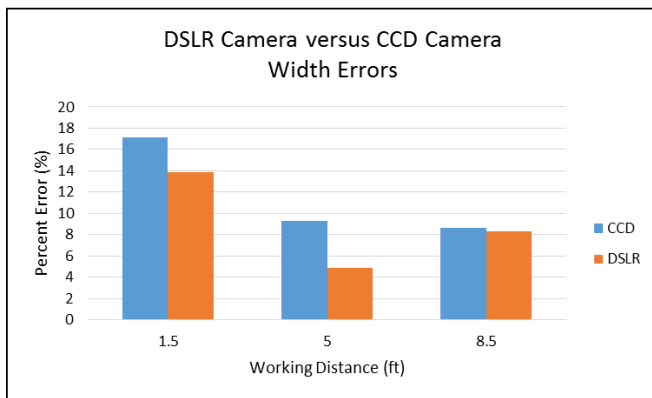


Figure 84: Comparison of CCD vs DSLR

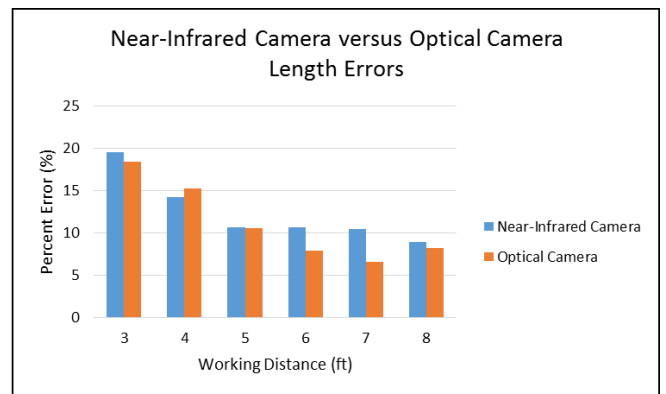
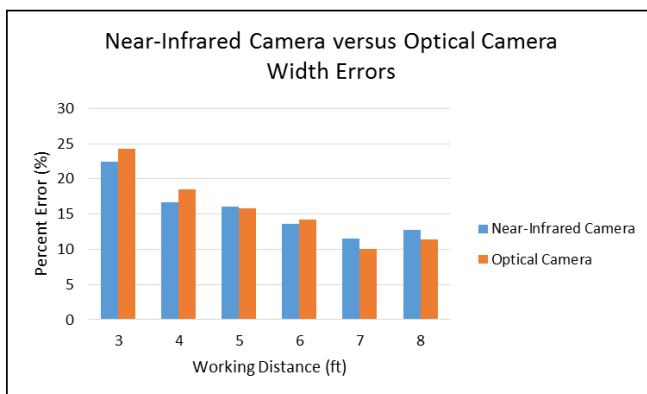


Figure 85: Comparison of NIR versus Optical

Table 31: P-Values for Normality - Nikon D610 Imaging

Data Set	P-value
Width Error: 6 in by 0.125 in	0.277
Width Error: 6 in by 0.06 in	0.315
Width Error: 6 in by 0.02 in	0.54
Width Error: 4 in by 0.0125 in	0.403
Width Error: 4 in by 0.06 in	0.64
Width Error: 4 in by 0.02 in	0.23
Length Error: 6 in by 0.125 in	0.263
Length Error: 6 in by 0.06 in	0.387
Length Error: 6 in by 0.02 in	0.235
Length Error: 4 in by 0.0125 in	0.394
Length Error: 4 in by 0.06 in	0.158
Length Error: 4 in by 0.02 in	0.744

Table 32: P-values for Normality - Acquisition Systems

Acquisition System	Dimension	P-value
18 MP	Width	0.731
24.3 MP	Width	0.551
18 MP	Length	0.427
24.3 MP	Length	0.295
CCD	Width	0.433
DSLR	Width	0.318
CCD	Length	0.551
DSLR	Length	0.425
NIR	Width	0.756
Optical	Width	0.378
NIR	Length	0.27
Optical	Length	0.064

Table 33: P-values for T-test - Length Comparison

Data Set	Dimension	P-value
0.125	Width	0.308
0.125	Length	0.262
0.06	Width	0.632
0.06	Length	0.13
0.02	Width	0.963
0.02	Length	0.789

Table 34: P-values for T-test - Acquisition Systems

Data Set	Dimension	P-Value
Sensor Size	Width	0.015
Sensor Size	Length	0
CCD vs. DSLR	Width	0.937
CCD vs. DSLR	Length	0.623
NIR vs Optical	Width	0.579
NIR vs Optical	Length	0.064

Table 35: Average Aperture Errors for a 0.02 in. Crack

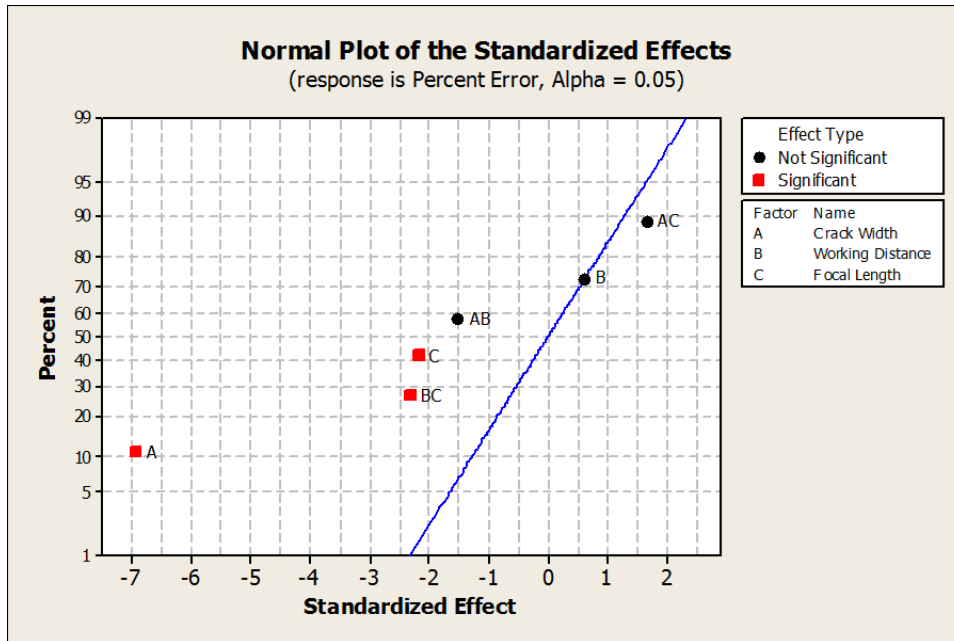
<b>0.02 in. Crack</b>						
3 ft.						
Aperture Value	4.5	5	5.6	6.3	9	10
Average Percent Environmental Error	62.17	56.6	67.75	39.86	67.75	56.6
4 ft.						
Aperture Value	4.5	5	5.6	6.3	9	10
Average Percent Environmental Error	59.5	44.625	59.5	44.625	59.5	74.375
5 ft.						
Aperture Value	4.5	5	5.6	6.3	9	10
Average Percent Environmental Error	60.315	97.505	23.125	41.72	134.69	78.91
6 ft.						
Aperture Value	4.5	5	5.6	6.3	9	10
Average Percent Environmental Error	112.375	157	112.375	78.9063	123.531	112.375
7 ft.						
Aperture Value	4.5	5	5.6	6.3	9	10
Average Percent Environmental Error	104.123	156.185	156.185	130.153	104.12	182.2175
8 ft.						
Aperture Value	4.5	5	5.6	6.3	9	10
Average Percent Environmental Error	119	178.5	178.5	178.5	163.625	238

Table 36: Average Aperture Errors for a 0.06 in. Crack

<b>0.06 in. Crack</b>							
3 ft.							
Aperture Value	5	5.6	6.3	8	9	13	18
Average Percent Environmental Error	26.86	14.87	3.72	7.44	22.31	26.03	22.31
4 ft.							
Aperture Value	5	5.6	6.3	8	9	13	18
Average Percent Environmental Error	21.07	33.05	23.13	23.13	23.55	35.53	18.59
5 ft.							
Aperture Value	5	5.6	6.3	8	9	13	18
Average Percent Environmental Error	23.55	23.55	11.57	17.35	11.98	5.78	17.35
6 ft.							
Aperture Value	5	5.6	6.3	8	9	13	18
Average Percent Environmental Error	7.22	5.16	30.56	23.13	6.19	8.25	6.19
7 ft.							
Aperture Value	5	5.6	6.3	8	9	X	X
Average Percent Environmental Error	11.99	19.63	17.36	5.79	20.66	X	X
8 ft.							
Aperture Value	5	5.6	6.3	8	20	X	X
Average Percent Environmental Error	15.29	3.58	4.96	14.88	0.84	X	X

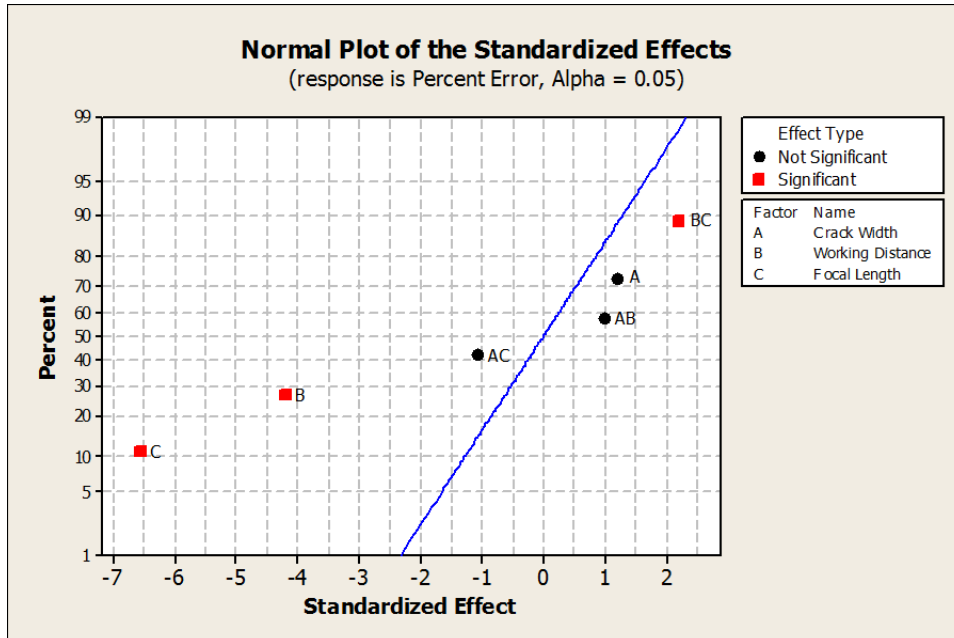
Table 37: Average Aperture Errors for a 0.125 in. Crack

<b>0.125 in. Crack</b>							
3 ft.							
Aperture Value	5	5.6	8	9	13	14	20
Average Percent Environmental Error	19.57	24.02	19.58	17.79	19.58	24.92	14.22
4 ft.							
Aperture Value	4	5	5.6	8	13	14	20
Average Percent Environmental Error	19.04	10.72	15.47	26.18	22.61	23.80	19.04
5 ft.							
Aperture Value	5	5.6	8	13	14	20	X
Average Percent Environmental Error	10.94	12.43	14.20	12.20	17.18	9.05	X
6 ft.							
Aperture Value	5	5.6	8	13	14	20	X
Average Percent Environmental Error	12.45	17.40	14.20	17.77	17.77	13.04	X
7 ft.							
Aperture Value	5	5.6	8	13	14	20	22
Average Percent Environmental Error	6.22	8.29	29.08	20.75	20.77	10.38	16.60
8 ft.							
Aperture Value	5	5.6	8	9	13	14	20
Average Percent Environmental Error	8.3	8.28	0.93	4.72	4.72	14.24	21.36



Width

Figure 86: Interaction Plot for Width Errors (Minitab, 2007)



Length

Figure 87: Interaction Plot for Length Errors (Minitab, 2007)

## APPENDIX D: IN-SERVICE CRACKS

---

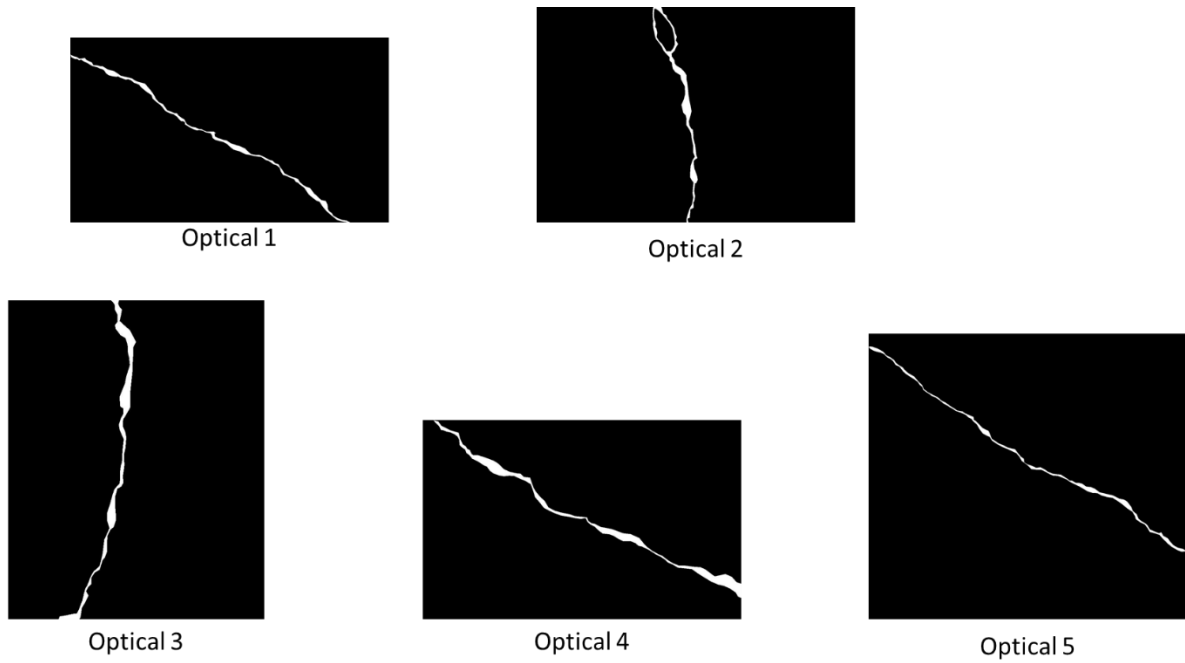


Figure 88: Manually Segmented Optical Images

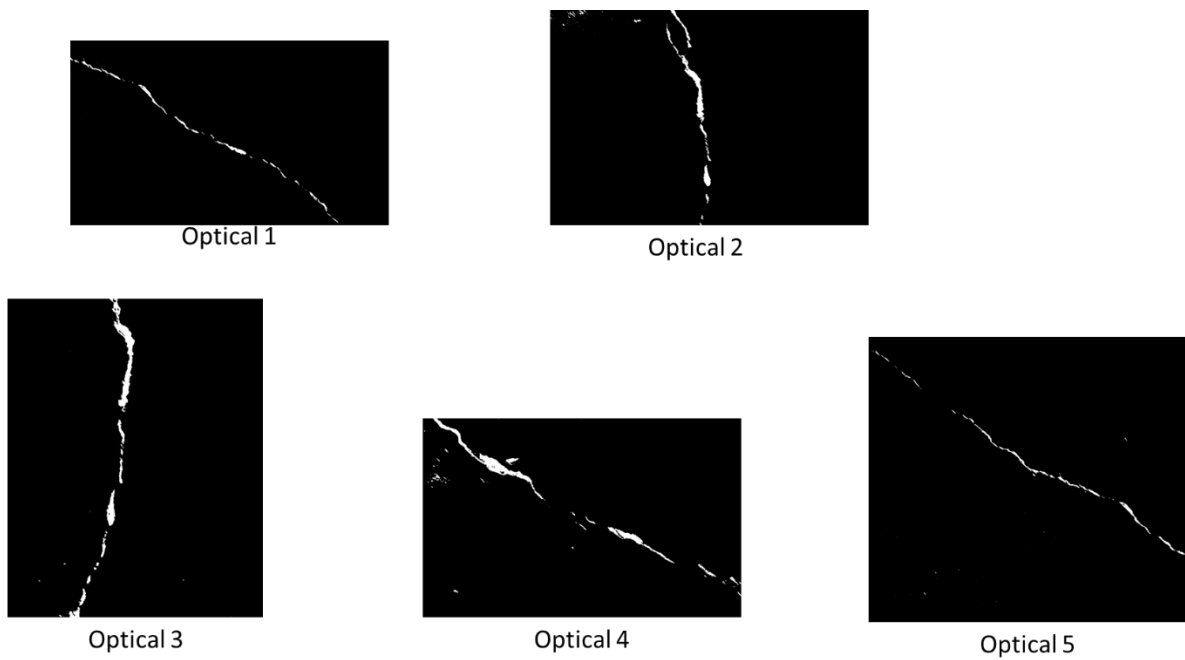


Figure 89: Optical Images Segmented by Jahanshahi Adapted Method

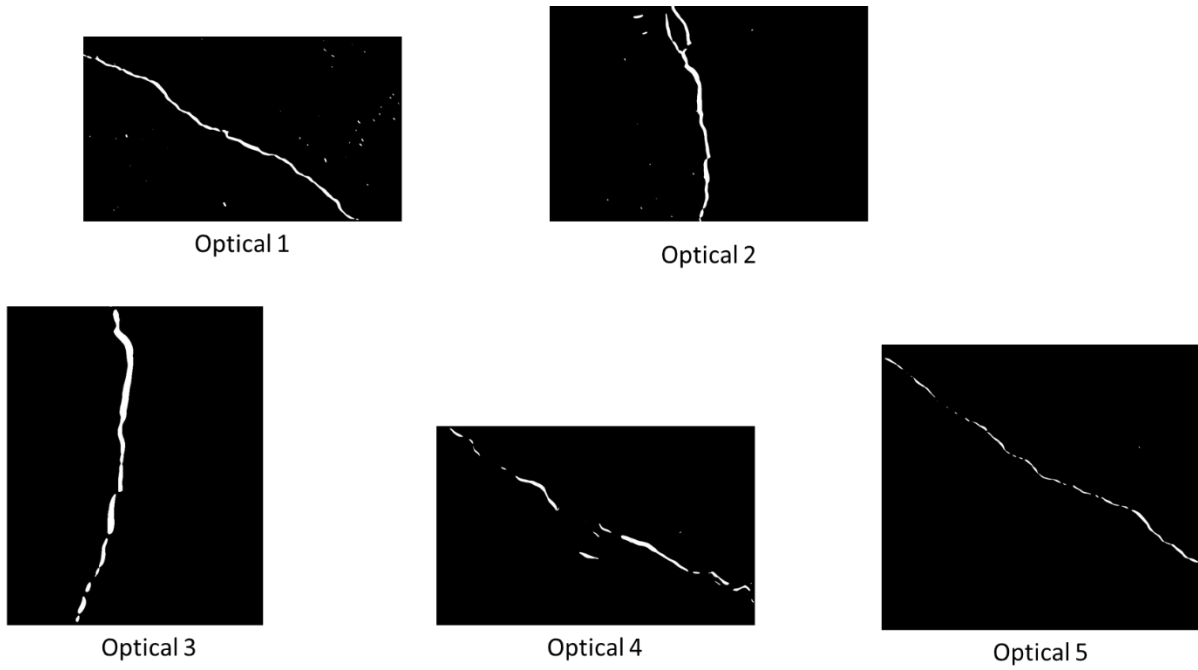


Figure 90: Optical Images Segmented by Fujita Adapted Method

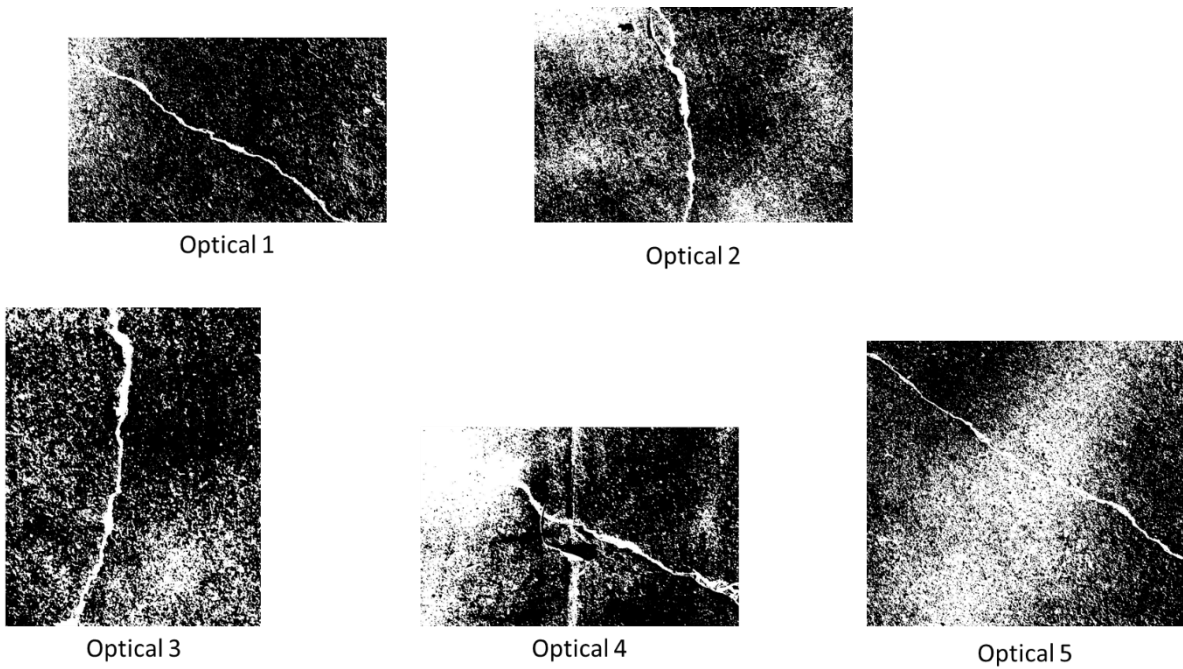


Figure 91: Optical Images Segmented by Lattanzi Adapted Method

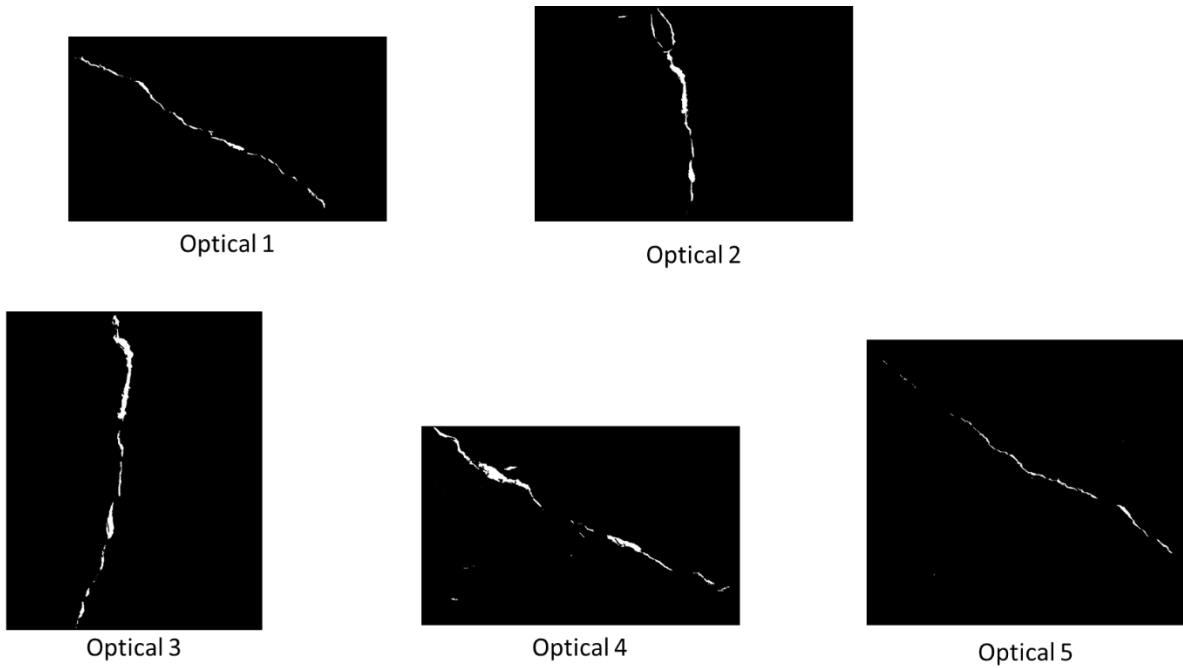


Figure 92: Optical Images Segmented by Combined Method

Table 38: Width Errors for In-Service Optical Images

Image Name	Rotation (degrees)	Manually Segmented Width (pixels)	Jahan Error (%)	Fujita Error (%)	Combined Error (%)
Op_1	-30.7894	41	31.71	21.95	17.07
Op_2	-79.886	95	50.53	6.32	30.53
Op_3	82.9048	19	10.53	84.21	36.84
Op_4	-28.6699	36	25.00	5.56	5.56
Op_5	-32.0745	33	33.33	39.39	3.03

Table 39: Length Errors for In-Service Optical Images

Image Name	Rotation (degree)	Manually Segmented Length (pixels)	Jahan Error (%)	Fujita Error (%)	Combo Error (%)
Op_1	-30.7894	926	27.54	61.02	2.05
Op_2	-79.886	931	17.08	43.07	13.96
Op_3	82.9048	381	16.80	21.00	0.79
Op_4	-28.6699	645	21.86	14.11	33.95
Op_5	-32.0745	916	88.97	0.76	51.53

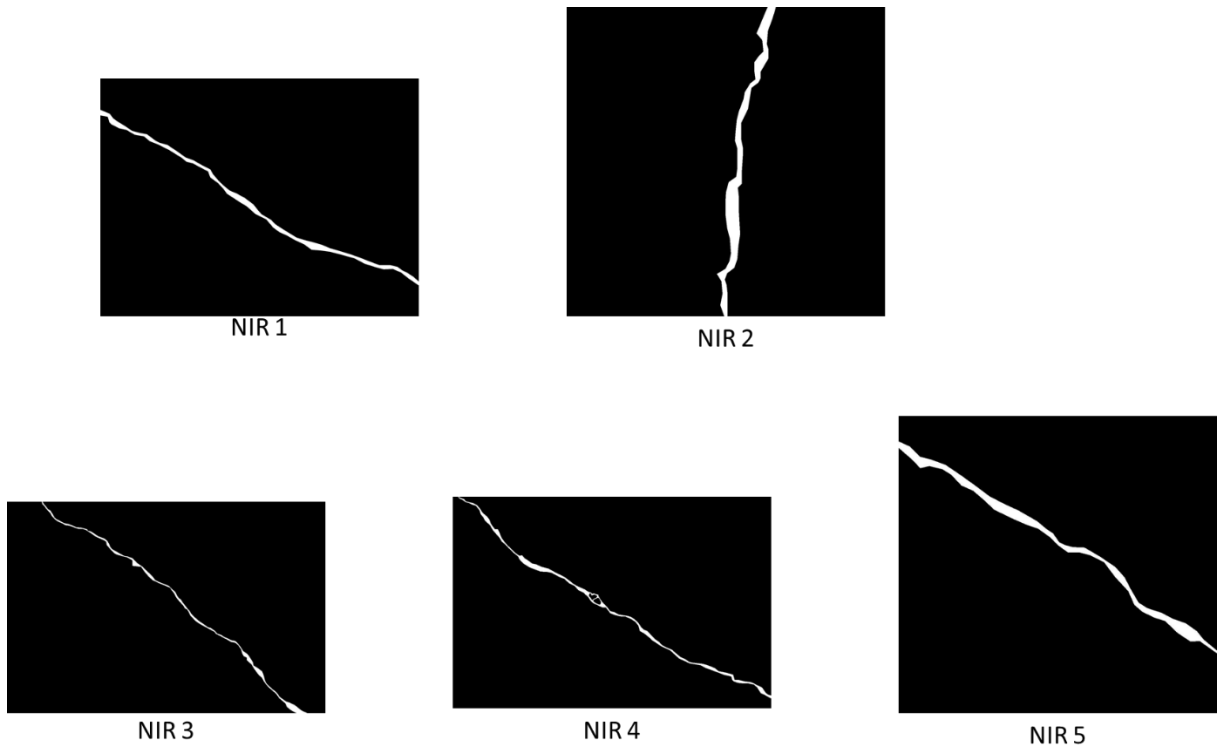


Figure 93: Manually Segmented NIR Images

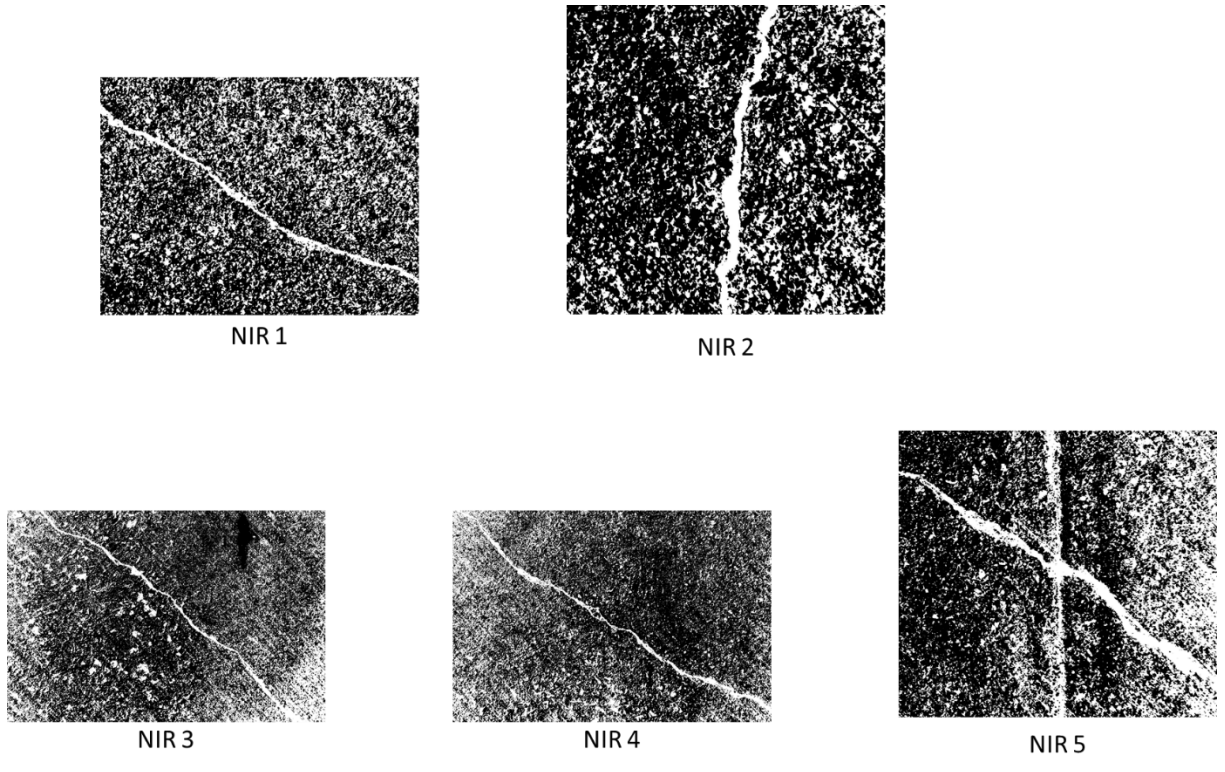


Figure 94: NIR Images Segmented by Jahanshahi Adapted Method

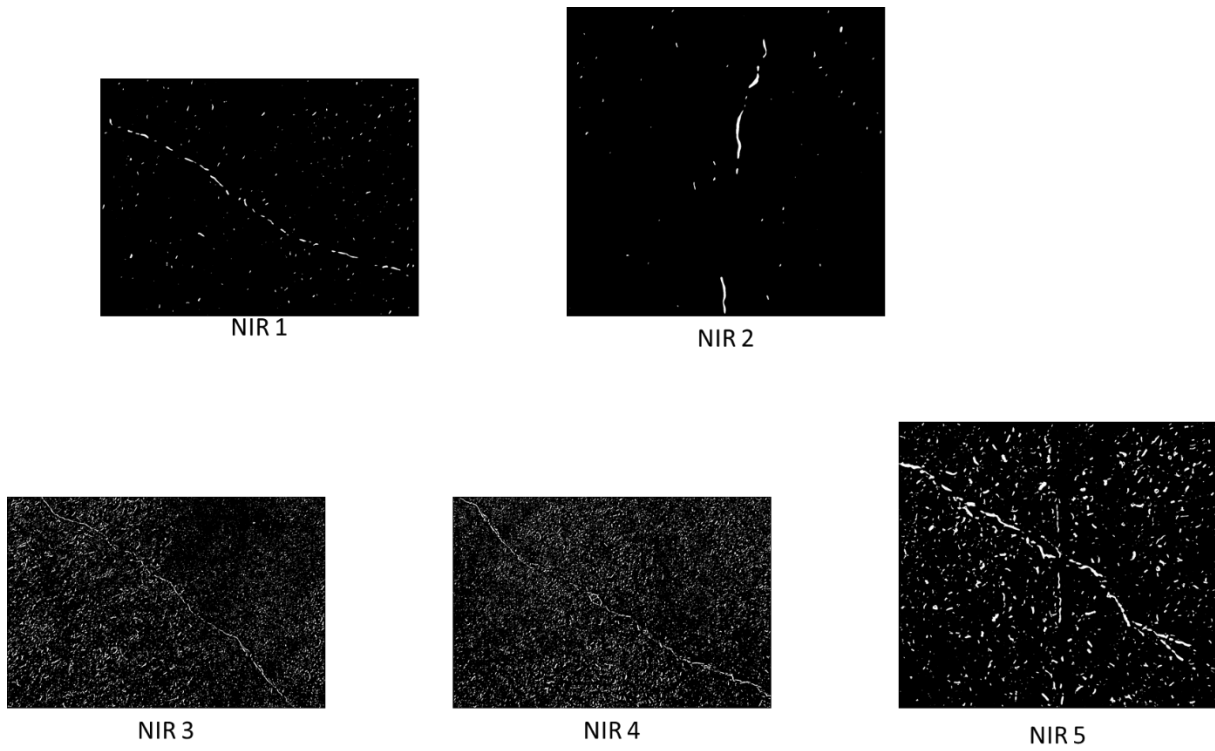


Figure 95: NIR Images Segmented by Fujita Adapted Method

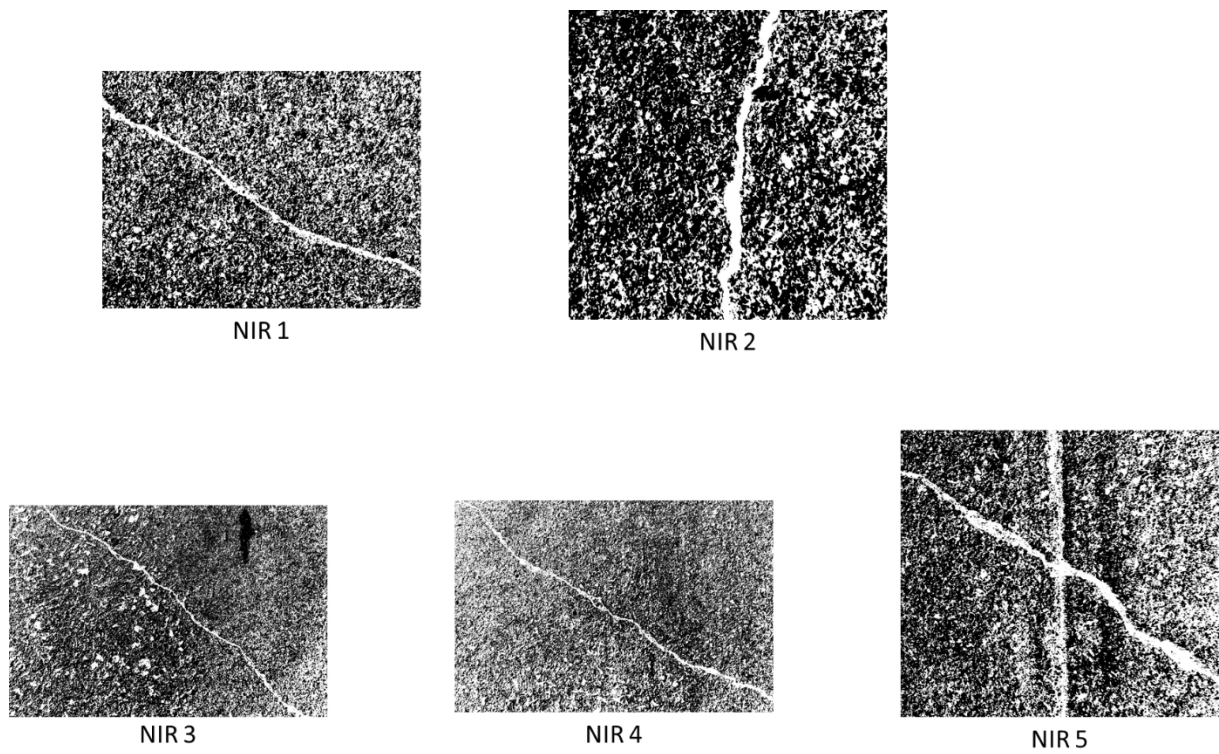
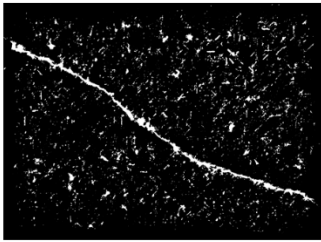
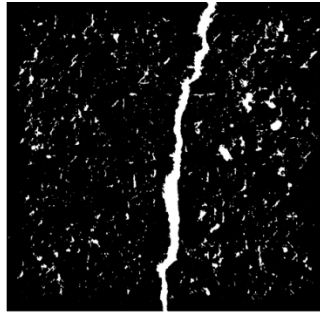


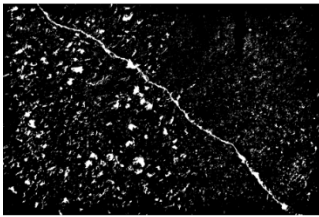
Figure 96: NIR Images Segmented by Lattanzi Adapted Method



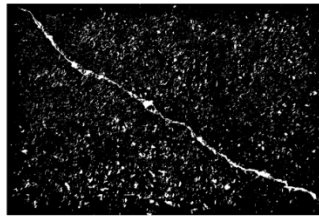
NIR 1



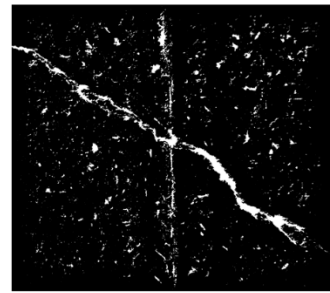
NIR 2



NIR 3



NIR 4



NIR 5

Figure 97: NIR Images Segmented by Combined Method

## APPENDIX E: MATLAB CODES

---

### Jahanshahi Adapted Method:

```
% An innovative methodology for detection and quantification
%of cracks through incorporation of depth perception by: Jahanshahi, Masri, and Padgett
clear all
close all
%%

%Properties
I = imread('NIR_5.jpg'); %Import Image

dis = 3; %Working Distance in feet

thick = 0.1; %Crack width in inches

sensor_res = 24.3;% Megapixels

sensor_size = 0.00595; %Pixel Pitch in mm

focal_length = 24; %mm

I = rgb2gray(I); %Convert to grayscale

working_distance = (dis*12)*25.4; %Convert Working Distance to mm

crack_width = thick*25.4; %Convert Crack Width to mm

crack_length = 8*25.4; %Input Crack Length in mm

% All Variables must be manually changed for each picture

%%
%Establish structuring element

LEN = (focal_length / working_distance) * (sensor_res / sensor_size) * crack_width;

Cstart = I;
%based off of equation (2) in paper

SE1 = strel('line', round(Len), 0); % 0 degrees rotation
O1 = imclose(I, SE1);
C1 = imadd(imopen(O1, SE1), Cstart);
```

```

SE2 = strel('line', round(LEN), 45); % 45 degrees rotation
O2 = imclose(Cstart, SE2);
C2 = imadd(imopen(O2, SE2), Cstart);

SE3 = strel('line', round(LEN), 90); % 90 degrees rotation
O3 = imclose(Cstart, SE3);
C3 = imadd(imopen(O3, SE3), Cstart);

SE4 = strel('line', round(LEN), 135); % 135 degrees rotation
O4 = imclose(Cstart, SE4);
C4 = imadd(imopen(O4, SE4), Cstart);

% %
%Prepare to Threshold

T = C4;
thresh = graythresh(T); % Threshold Value

bw = (T <= thresh * 255); % Global Threshold

imshow(bw) % View Image

% %
%Rotation

C = bw;

STATS11 = regionprops(C, 'Orientation');

O = extractfield(STATS11, 'Orientation');

C = imrotate(C, -O);

C = bwmorph(C, 'spur');

imshow(C)

```

### Fujita Adapted Method:

```
% A robust automatic crack detection method from noisy concrete surface by Fujita and
% Hamamoto
clear all
close all
%%

% Load in images

I = imread('NIR_5.jpg');

dis = 8; % Working Distance feet

thick = 0.125; % Crack Width in inches

iter = 10; % Number of iterations for probabilistic relaxation

tt = 30; % Percentage of local average in which the threshold is set

sensor_res = 24.2; % Megapixels

sensor_size = 0.00595; % Pixel Pitch in mm

I = rgb2gray(I); % Convert image to grayscale

focal_length = 85; % mm

working_distance = (dis*12)*25.4; % Convert working distance to mm

crack_width = thick*25.4; % Convert crack width to mm

crack_length = 4*25.4; % Convert crack length to mm

% must manually change for each picture

%%

% Median Filter
I_median = medfilt2(I, [11 11]);

% Subtract the two images
I_new = imadd(I_median,I);

%%
```

```

%Multi-scale line emphasis
I_new2=FrangiFilter2D(double(I_new));
%Not built into MATLAB, must download and write separately

%%
%Probabilistic relaxation
im0 = I_new2;

im0 = double(im0);

P_drk= log(im0 + 1)/log(max(im0(:) +1));

P_lgt = 1-P_drk;

P=cat(3,P_drk,P_lgt);

L=RelaxLabel2D(P,[],[2 1 iter 8]);
%Not built into MATLAB, must download and write separately

%P – array of probabilities

% iter – number of max iterations

%8 – indicates the neighborhood connectivity

T = (L==2); % Where the crack is located

%%

%Adaptive Threshold
T = double(T);

[x y] = size(T);

if x>y
    fsize = fix(x/30);
else
    fsize = fix(y/30);
end

bw = adaptivethresh(T, fsize, tt, 'gaussian', 'relative');
%Not built into MATLAB, must download and write separately

%T – Image to be thresholded

```

```
% fsize – filter size used to determine the local weighted average
% tt – percentage relative to local average
% Gaussian – use Gaussian smoothing to obtain local weighted mean
%Relative – means “tt” is the percentage relative to the local average gray value below which the
%threshold is set

figure; imshow(bw)

%%
%Rotation

C = bw;

STATS11 = regionprops(C, 'Orientation');
OO = extractfield(STATS11, 'Orientation');

C = imrotate(C, -OO);

C = bwmorph(C, 'spur');

imshow(C)
```

### Lattanzi Adapted Method:

```
% Robust automated concrete damage detection algorithms for field applications
%%
clear all
close all

I = imread('DSC_2126.jpg');

A = rgb2gray(I); % Convert image to grayscale

J = histeq(A); %Histogram Equalization

ab = double(J);

nrows = size(ab,1);

ncols = size(ab,2);

[id centroid] = kmeans(ab(:),6, 'emptyaction', 'drop', 'Replicates',5);
%Manually change number of clusters and iterations

%Use cluster value between 6 and 12

%Iterate to avoid local minimas and to reach a point where the values in the clusters do not
%change

%Drop – removes any clusters that become empty

pixel_labels = reshape(id,nrows,ncols);

figure; imshow(pixel_labels,[], title('image labeled by cluster index'));

segmented = cell(1,3);

rgb_label = repmat(pixel_labels, [1 1 3]);

for k = 1:6 %Separate the clusters
    color = I;
    color(pixel_labels ~=k)=0;
    segmented{k} = color;
end

%Find mean values of clusters
a = mean(segmented{1}(:));
```

```

b= mean(segmented{2}(:));
c= mean(segmented{3}(:));
d= mean(segmented{4}(:));
e= mean(segmented{5}(:));
f= mean(segmented{6}(:));

mean_val = [a;b;c;d;e;f];

%Segment the cluster with the lowest mean
num = find(mean_val == min(mean_val(:)));

num = min(num);

figure; imshow(segmented{num});

T = rgb2gray(segmented{num});

thresh = graythresh(T);

bw = (T <= thresh * 255);

%Rotation
C = bw;

STATS11 = regionprops(C, 'Orientation');

OO = extractfield(STATS11, 'Orientation');

C = imrotate(C, -OO);

C = bwmorph(C, 'spur');

figure; imshow(C)

```

### Combined Method:

```
clear all
close all

%Properties
L = imread('NIR_1.jpg');

focal_length = 24; %in mm

dis = 3; %Working Distance in feet

thick = 0.01; %Crack width in inches

tt = 30; % Percentage of local average in which the threshold is set

sensor_res = 24.2;%Megapixels

sensor_size = 0.00595; %Pixel Pitch in mm

I = rgb2gray(L); %Convert to grayscale image

working_distance = (dis*12)*25.4; %Convert working distance to mm

crack_width = thick*25.4; %Convert crack width to mm

crack_length = 6*25.4; %Convert crack length to mm
%must manually change for each picture

%%
%Establish structuring element
LEN = (focal_length / working_distance) * (sensor_res / sensor_size)* crack_width;

Cstart = I;

SE1 = strel('line', round(LLEN), 0);
O1 = imclose(I, SE1);
C1 = imadd(imopen(O1, SE1), Cstart);

SE2 = strel('line', round(LLEN), 45);
O2 = imclose(Cstart, SE2);
C2 = imadd(imopen(O2, SE2), Cstart);

SE3 = strel('line', round(LLEN), 90);
O3 = imclose(Cstart, SE3);
C3 = imadd(imopen(O3, SE3), Cstart);
```

```

SE4 = strel('line', round(LEN), 135);
O4 = imclose(Cstart, SE4);
C4 = imadd(imopen(O4, SE4), Cstart);

%%

% Adaptive Threshold
% "adaptivethresh" is not built into MATLAB, must download and write separately

% T – Image to be thresholded

% fsize – filter size used to determine the local weighted average

% tt – percentage relative to local average

% Gaussian – use Gaussian smoothing to obtain local weighted mean

% Relative – means "tt" is the percentage relative to the local average gray value below which the
% threshold is set

T = C3;

T = double(T);

[x y] = size(T);

if x>y
    fsize = fix(x/30);
else
    fsize = fix(y/30);
end

bw1 = adaptivethresh(C1, fsize, tt, 'gaussian', 'relative');
bw1 = bwmorph(bw1, 'spur');

bw2 = adaptivethresh(C2, fsize, tt, 'gaussian', 'relative');
bw2 = bwmorph(bw2, 'spur');

bw3 = adaptivethresh(C3, fsize, tt, 'gaussian', 'relative');
bw3 = bwmorph(bw3, 'spur');

bw4 = adaptivethresh(C4, fsize, tt, 'gaussian', 'relative');
bw4 = bwmorph(bw4, 'spur');

%%
A = imadd(bw1, bw2);

```

```
B = imadd(A, double(bw3));  
  
C = imadd(B, double(bw4));  
  
%Additional Morphological Operations to bridge non-continuous pixels  
C = bwmorph(C,'bridge');  
  
C = imfill(C, 'holes');  
  
imshow(C)  
  
%Rotation  
STATS11 = regionprops(C, 'Orientation');  
  
OO = extractfield(STATS11, 'Orientation');  
  
C = imrotate(C, -OO);  
  
C = bwmorph(C, 'spur');  
  
figure; imshow(C)
```

### Euclidean Distance Transform:

```
C_skel = bwmorph(C, 'skel', Inf); %Create image skeleton

C_skel = imcomplement(C_skel); %Compute the complement of the image

dist_trans = bwdist(C_skel); %Compute the Euclidean distance transform of the image

%%

%Compute Width
[xd, yd] = size(dist_trans);

for i = 1:xd

    for j = 1:yd

        if dist_trans(i,j) > 0

            p(i,:) = dist_trans(i,j);

        end

    end

end

pp = bwlabel(p);

[ap,bp] = histc(pp,unique(pp));

%%

%Compute Length
for i = 1:xd

    for j = 1:yd

        if dist_trans(i,j) > 0

            l(j) = dist_trans(i,j);

        end

    end

end

end
```

```
ll = bwlabel(I);  
[al,bl] = histc(ll,unique(ll));  
  
%%  
%Combine answer into one matrix  
answer = [mean(ap); sum(al)]  
  
%For in-service results use the mean of “ap” to find the mean width  
  
%For in-service results use the sum of “al” to find the total length  
  
%For ideal cases mean(ap) = ap  
  
%For ideal cases sum(al) = al
```